DLR-IB-FA-SD-2018-199

Uncertainty in the Layer Angle Detection of Carbon Fiber Preforms and Handling of Fabrics

Masterarbeit

Autor Lars Maxfield

Deutsches Zentrum
DLR für Luft- und Raumfahrt

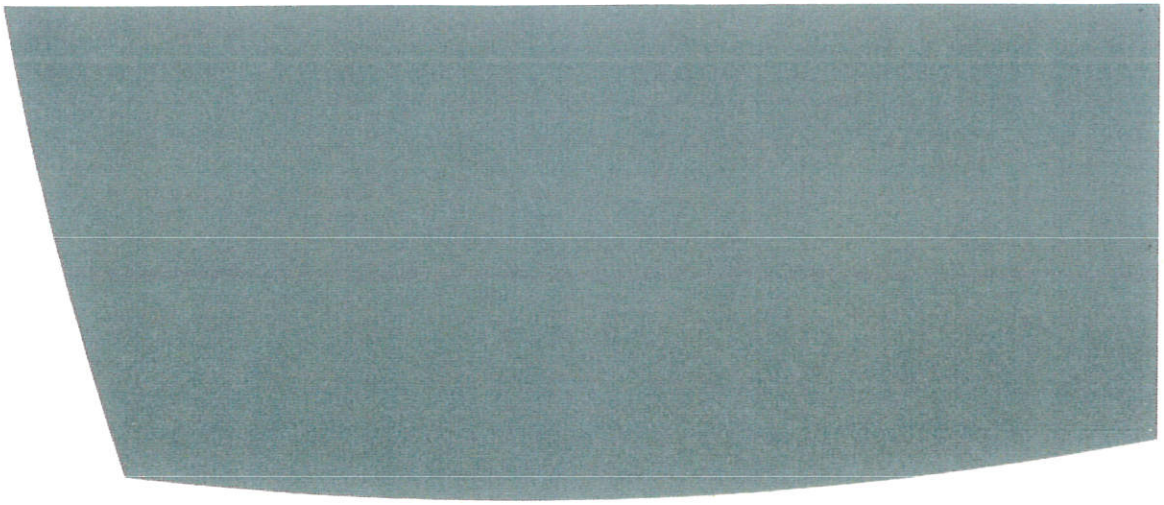

Institut für Faserverbundleichtbau und Adaptronik

DLR-IB-FA- SD-2018-199

Uncertainty in the Layer Angle Detection of Carbon Fiber Preforms and Handling of Fabrics

Zugänglichkeit:

Stufe 1 Allgemein zugänglich: Der Interne Bericht wird elektronisch ohne Einschränkungen in ELIB abgelegt. Falls vorhanden, ist je ein gedrucktes Exemplar an die zuständige Standortbibliothek und an das zentrale Archiv abzugeben.

Stade, *den*

Der Bericht umfasst: 85 Seiten

Abteilungsleiter: Prof. Dr.-ing. Jan Stüve

Autoren: Lars Maxfield

Autor 2 / Betreuer: Christian Bülow

Deutsches Zentrum für Luft- und Raumfahrt

Uncertainty in the Layer Angle Detection of Carbon Fiber Preforms and Handling of Fabrics:

The Application of Eddy Current and Laser Measurement Techniques in an Automated Resin Transfer Molding Production Line

A Master's Thesis
Submitted to the Department of Mechanical Engineering
and Business Administration
of Luebeck University of Applied Sciences
in Partial Fulfillment of the Requirements
for the Degree of
Master of Science in Mechanical Engineering

Lars Maxfield
July 2018

Abstract

This master's thesis investigates the uncertainty along the experimental carbon fiber reinforced polymer manufacturing line at the German Aerospace Center (DLR) known as EVO, a facility seeking to achieve full production automation based on the resin transfer molding (RTM) process. Specifically, two areas of the EVO facility are investigated in this thesis: 1) the handling of dry carbon fiber fabrics with a vacuum-based gantry, and 2) the layer angle detection of carbon fiber preforms with eddy current testing (ECT) and two-dimensional fast Fourier transformations (2D-FFTS).

For fabric handling, a method to determine the position of a quadrilateral fabric cutout using laser-based 3D surface scanning equipment and mathematical manipulation is proposed. The proposed fabric position measurement method has a translational uncertainty of 0.11 mm and rotational uncertainty of 0.01°. The two fabric handling steps specifically examined – the transfer from the cutter to the storage drawers and then to the preparation table – exhibited translational uncertainties no larger than 0.22 mm and rotational uncertainties no larger than 0.03°.

For the ECT/2D-FFT-based analysis of preform layer angles, a new system of numerical algorithms dubbed superX (sX) was developed and verified. Various sX parameters were also optimized using pseudo images and existing 256 mm × 256 mm ECT scans of preform specimens with various fiber materials and stackups. The ECT data and optimized sX system show a detection uncertainty of 0.20° in the fiber direction of an arbitrarily oriented layer in preforms with four distinct fiber directions – e.g., with four unidirectional layers or two biaxial layers. The results from a nine-layered preform with unidirectional fibers show the ECT/2D-FFT-based sX system can detect all layer angles with an uncertainty of no more than 0.12°. These results also support two behaviors of ECT: 1) detection uncertainty increases exponentially with layer depth, and 2) layer recognition and angle accuracy increase with sensor frequency.

Contents

Chapter 1

Introduction

The aerospace industry's increasing demand for lightweight structural components made from carbon fiber reinforced polymers (CFRPs) requires the continued research and development of high-volume manufacturing methods. One such potential CFRP manufacturing method is resin transfer molding (RTM), which involves fabric layup, preforming, and closed-mold resign/epoxy injection. The experimental near-net shape production facility referred to as EVO[1] at the German Aerospace Center (DLR[2]) in Stade, Germany, seeks to establish a fully automated production line based on RTM.

As with all production processes, deviations at each stage in EVO have a direct effect on the performance of final components; however, not all stages have been analyzed for their role in adding to the uncertainty in this production chain. The transfer, storage, and manipulation of carbon fiber *sheets* (referred to in this thesis as *fabric handling*) has yet to be documented concerning deviation. And while previous attempts to define the uncertainty of layer angle detection in consolidated sheets of fabric (i.e., *preforms*[3]) have beeen made, an improved and systematic analysis scheme must still be implemented to reach a robust and accurate uncertainty value. To ensure component quality and allow refinement of the EVO chain – and ultimately meet the rising demand for high-performance CFRP components – the uncertainty in fabric handling and preform layer angle detection must be investigated and defined.

This thesis pursues solutions for these topics at EVO in the form of a two-fold target: 1) investigate and define the uncertainty in the handling of carbon fiber fabrics and layer angle detection of preforms; and 2) improve the software methods used to determine the uncertainties in both these and other stages along the EVO production line. Chapter 2 reviews the relevant technological and scientific background of this target, which in turn allows us to understand its underlying motivation. The following chapters are distinguished by the two areas of focus in this thesis.

[1] DE: *Endkonturnahe Volumenbauteile*

[2] DE: *Deutsches Zentrum für Luft- und Raumfahrt*

[3] Preforms can be imagined as "sandwiches" of carbon fiber fabrics constituting the fiber skeleton of the final CFRP part. Chapter 2 explains this in detail.

Focus 1: Fabric handling uncertainty

The first focus of this thesis can be posed as a question:

Do the deviations in fabric movement exceed the measurement uncertainties – and if so, how large are these deviations?

A commercial laser-based 3D surface scanner is dictated as the given measurement system in this thesis. Additionally, a rectangular sheet of carbon fiber is dictated as the given specimen to be used in defining fabric handling uncertainty. Because this laser system has not yet explicitly been used to determine the movement of carbon fiber sheets, a novel method of deriving fabric position must first be developed. Hence, before measurements of specific steps in the EVO facility can be made, the uncertainty in the measurement itself must be established. Determining fabric handling uncertainty can be divided into these distinct tasks:

- Establish a robust method to determine the absolute position of a rectangular sheet of carbon fiber using 3D laser scan data.
- Plan and execute the laser-based measurement of deviations in carbon fiber fabric movement between the cutter table, storage shelves, and transfer table (i.e., the fabric handling) of the EVO production line.
- Determine if deviations in the handling stage exceed the measurement uncertainty – and if so, define the uncertainty.

Chapter 3 defines the experimental setup and methodology regarding these tasks, and Chapter 4 presents the results and analysis.

Focus 2: Preform layer angle detection uncertainty

Posing the second focus of this thesis also as a question:

What is the uncertainty in the detected angles of preform layers?

The use of eddy current testing (ECT) measurement equipment is dictated in this thesis. The primary product of ECT on preforms – *images* revealing the constituent fiber layers – have been used extensively to analyze preforms. Recent efforts at DLR on the application of 2D *fast Fourier transforms* (2D-FFT) on ECT images show that individual layer angles can determined; however, as of the release date of this thesis, no research has definitively established the uncertainty in these detected layer angles. Although a wide variety of ECT measurements have been successfully carried out in previous work at DLR, the software with which the related analyses were made was determined to be flawed. Determining preform layer angle detection uncertainty in this thesis can divided into the following tasks:

- Reformulate the software (and underlying algorithms) with which ECT data and 2D-FFTs are used to find the angles of preform layers.
- Use the reformulated software to evaluate previous ECT data and subsequently define the uncertainty in angle detection.

Chapter 5 describes the experimental setup and methodology regarding these tasks, and Chapter 6 presents the results and analysis.

Chapter 2

State of the Art

The purpose of this chapter is to review the technologies and physical principles which form the basis of the scientific work pursued in this thesis.

2.1 The rising demand for carbon fiber reinforced polymers

Innovations in aerospace manufacturing are profoundly motivated by the desire to reduce aircraft weight. Why is lighter better? That answer can be found in the fundamental description of level flight in the form of lift L and weight W [1]:

$$L = W \tag{2.1}$$

This simple balance of forces has a tremendous implication: Less weight means less required lift. Less lift means less lift-producing thrust is required, which in turn means less fuel spent. Less fuel means less money spent and – most important to today's emphasis on cleaner technologies – less emitted carbon dioxide.

Lighter is greener

Indeed, the aerospace industry's rapidly growing demand for lighter aircraft can at least be partially credited to the global push towards reduced carbon emissions. A report from the airline Southwest® shows that it costs the company US$1.2 million per year in added fuel when every passenger carries a cellphone [2]. Another US company, American Airlines®, reported its switch to an eight-kilogram-lighter drink cart saves eight million liters of fuel a year [3]. That boils down to a 1 million liter/yr/kg saving for American's fleet.

The far-reaching impact of weight reduction is not only felt in aerospace; a 2008 MIT study estimated that road vehicle weight reductions of 35% are feasible with modern materials, a reduction which translates to a reduced fuel consumption of at least 12% [4]. Applying this metric to US agency-reported vehicle and fuel statistics from 2012 [5, 6] returns an astounding fact: If one kilogram of weight would be removed from each vehicle in the US, annual emissions in the US would drop by nearly 200 million kilograms of CO_2.

The quality assurance problem

For both aerospace and other engineering industries, less is definitively better when it comes to component weight. But while the superior stiffness- and strength-to-weight properties of CFRP certainly appear capable of meeting this rising lightweight material demand, challenges in CFRP manufacturing must still be overcome to reach true mass production capabilities [7].

One of the most significant challenges in improving automated CFRP production processes is quality assurance, especially in RTM [8]. As with all manufacturing processes, quality assurance in RTM is grounded in the uncertainty of individual processes – and for good reason: A 10% fiber misalignment is capable of decreasing CFRP component strength by more than 30% [8, 9]. Simply stated, fiber orientation strongly influences CFRP component strength. And with fiber orientation being greatly affected in essential RTM processes like carbon fiber layup and fabric–preform consolidation [7, 8, 10], the pursuit of defining uncertainty in RTM processes is clearly justified.

2.2 EVo – An experimental resin transfer molding facility

The DLR's experimental CFRP production facility known as EVO is playing a key role in meeting the increasing demand for high-performance and mass-produceable composites. Defined as a high-volume near-net-shape manufacturing chain, EVO provides a testbed for technologies which seek to achieve a fully automated CFRP system based on the RTM process. One of the obstacles standing in the way of this goal is the investigation of uncertainty in certain steps of EVO, the task of which this thesis seeks to help complete. Before delving into the specific areas of this task, however, an overview of the general process is first needed.

RTM basics

The RTM process can be generalized into three steps [8, 11]:

1. **Fabric layup**: Carbon fibers are grouped into tows (untwisted bundles) which are subsequently laid up into various fabrics. While these fabric layups are typically biaxial weaves, they also include uniaxial sheets and multiaxial woven fabrics. These layups are then cut into the final cutouts.

2. **Preforming**: Fabric cutouts are draped along a 3D mold of the final component. These fabrics are then bonded into a single consolidation, or *preform*, which is effectively the reinforcement "skeleton" of the final carbon fiber component. Figure 2.1 (top) shows an example of a such a preform.

3. **Resin injection**: Figure 2.2 illustrates this final RTM step. The preform is first placed into a matching rigid mold and then closed to compaction. Binding polymer (often a thermosetting resin with

Fig. 2.1: (Top) dry preform and (bottom) final molded CFRP part [12].

low viscosity) is then injected into the mold. Curing occurs, and the final CFRP component is removed from the mold.

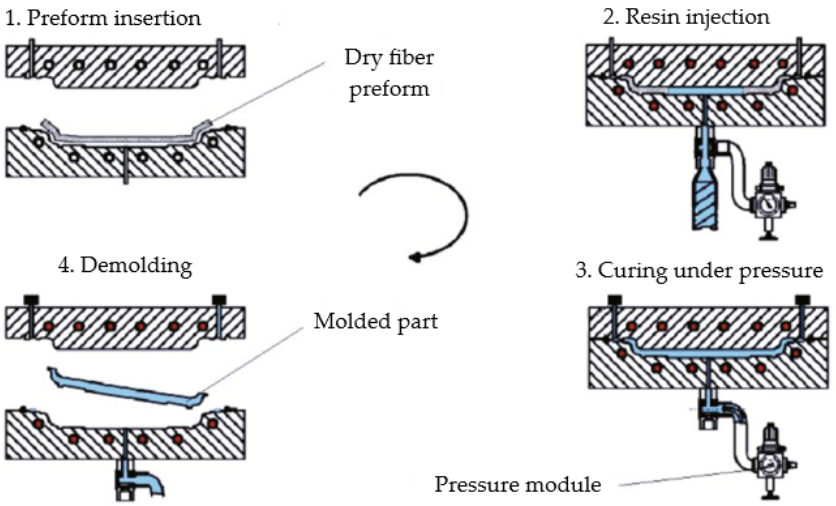

Fig. 2.2: Generalized drawing of the resin injection step of RTM [13].

EVo's implementation of RTM

To illustrate the stages of EVO, the general production steps are described in tandem with an aerospace frame which is made in EVO. Figure 2.3 shows the frame after four different stages.

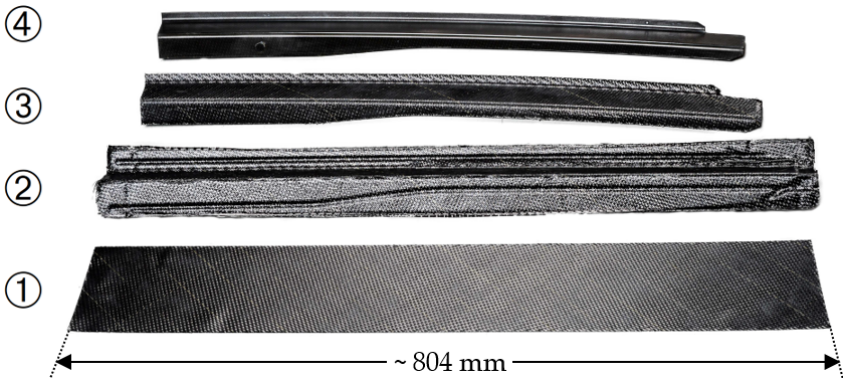

Fig. 2.3: Stages of an EVO-produced aerospace frame [14] as a: ① fabric cutout; ② draped and consolidated preform; ③ trimmed preform; ④ and final molded component. © DLR

Figure 2.5 shows EVO's fabric handling steps. A roll of prepared (i.e., pre-layed-up/woven) carbon fiber is automatically spread along the cutter table's surface, and then a preprogrammed CNC-cutter cuts a designated shape out of the raw fabric roll (see Fig. 2.4).

The result is a fabric cutout (① in Fig. 2.3). A gantry-based vacuum gripper with prealigned suction heads descends to the cutter table and picks up the fabric. The gripper then places the fabric either directly on the preparation table or in a drawer from which the cutout can be retrieved later.

Figure 2.7 provides an overhead view of the next area of EVO. Once the fabric cutout is on the preparation table, a robotic arm (not shown) picks up the fabric and proceeds to drape it across a tool. The draped

Fig. 2.4: Rolled-out carbon fiber fabric sheet being cut by the CNC-cutter.

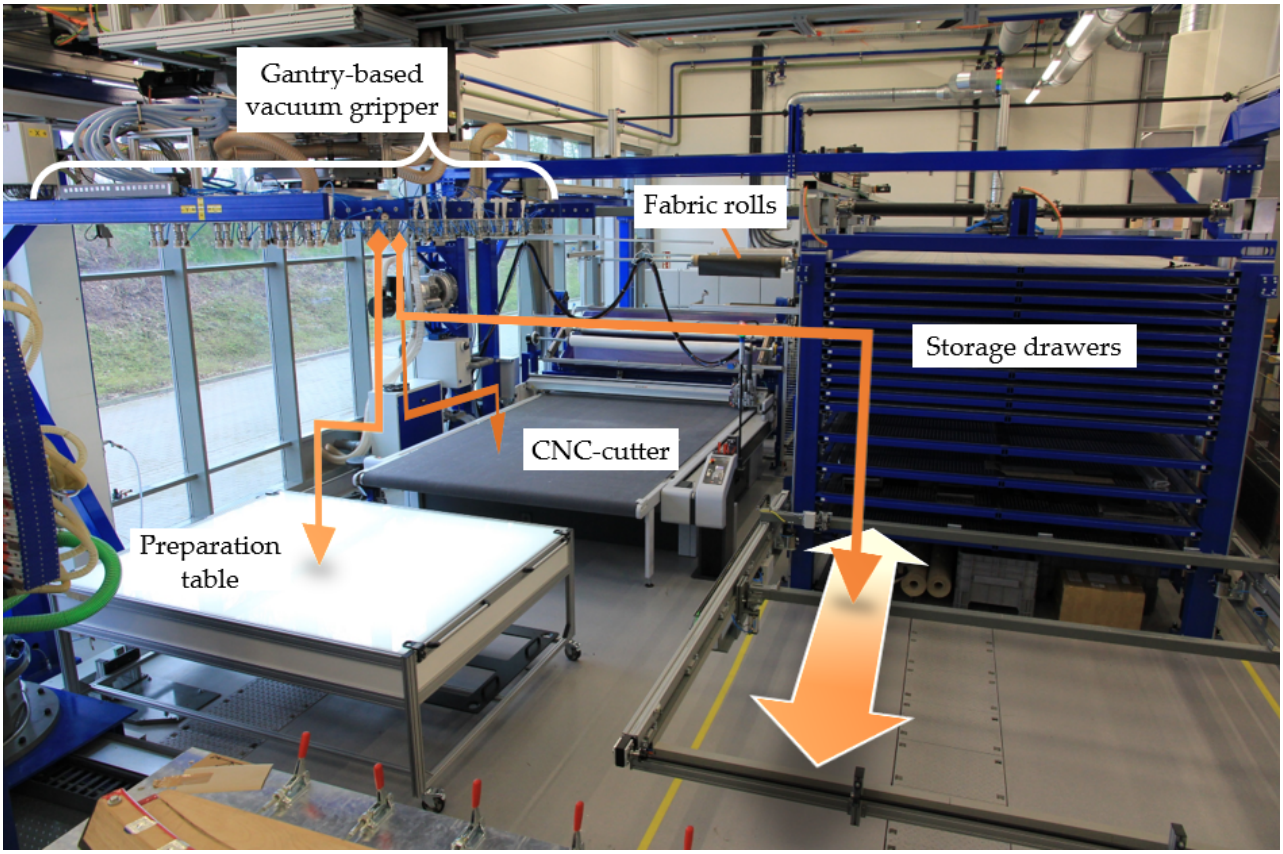

Fig. 2.5: Overhead view of the EVO chain's fabric handling stages and tools [14].

fabric is then consolidated, thus producing in an untrimmed preform (② in Fig. 2.3). Once trimmed to its final dry form (③ in Fig. 2.3), the preform is placed into the injection tool (example in Fig. 2.6). After resin injection, the component in its final form (④ in Fig. 2.3) is demolded, completing the EVO process.

The three phases of RTM – fabric production, preforming, and closed-mold resin/epoxy injection – have been the subject of numerous improved quality assurance research efforts [7, 8, 10, 15–17]. Although research has also been made along the EVO chain, two areas in particular have not been systematically analyzed in terms of uncertainty: 1) vacuum gripper handling of fabric cutouts; and 2) inline layer inspection of dry preforms with eddy current sensors.

Uncertainty in key areas of EVo

Each step of EVO plays a role in the resultant uncertainty of the final component's layer orientation. In the step where fabric cutouts are transported between the cutter, drawers, and preparation table with the vacuum gripper[1], minimization of placement error is equally critical. Misaligned fabric means misaligned fibers, and a misalignment of fibers could result in a drastically weaker final component.

If the technology for fabric handling at EVO – a gantry-based vacuum gripper – is to become a reliable tool in the mass-production of CFRPs for both aerospace and other high-performance industries,

5

Fig. 2.6: Example tool used in EVO for the resin injection stage [14]. © DLR

[1] For the remainder of this thesis, the vacuum gripper-based manipulation of fabric cutouts between the cutter, drawers, and preparation table are collectively referred to as *fabric handling*.

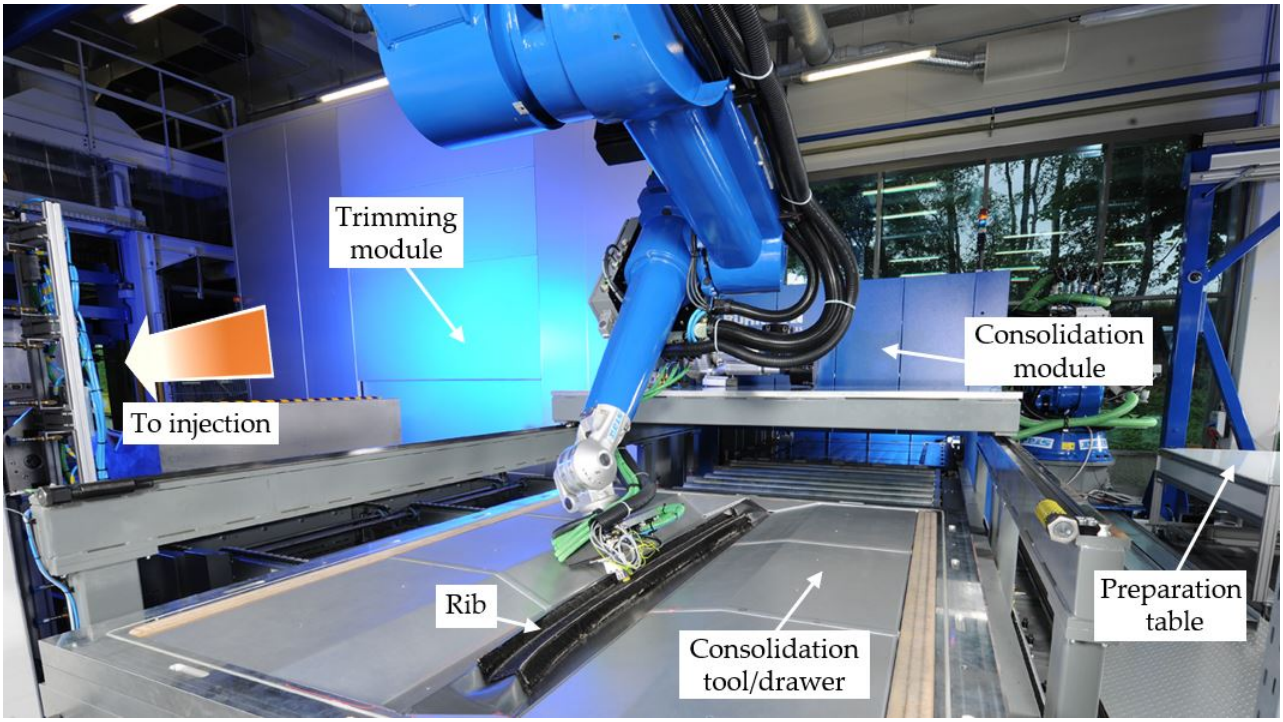

Fig. 2.7: View of post-handling EVO steps [14]. © DLR

a systematic analysis of uncertainty must be established. The first step in achieving this is to first determine if a detectable amount of deviation even occurs. To do so, an approach specifically designed with respect to EVO's fabric handling systems and available measurement equipment must be deployed. This is the motivation for the scientific work described in the first half of this thesis (Chapter 3 and Chapter 4).

For preform layer inspection (and subsequent layer angle detection) with ECT, efforts both internally and externally have already been made. The next section reviews the principles of ECT and describes the corresponding progress at EVO, thus providing the necessary scientific background and motivation for the second half of this thesis (Chapter 5 and Chapter 6).

2.3 Eddy current testing

ECT is widely considered to have the greatest potential as a non-destructive test approach for detecting defects in the production of single- and multi-layered carbon fiber preforms [7, 8, 10]. The "defect" of misaligned preform layers is derived by combining ECT and image processing tools, namely 2D-FFT, to compare detected layer angles with the prescribed angles. The final goal of 3D preform inspection in EVO is likewise being pursued by combining ECT/2D-FFT methods with a robot-arm mounted sensor like that shown in Fig. 2.7.

However, an analysis on the uncertainty of preform layer angles detected with ECT/2D-FFT has yet to be published. This thesis is intended to fill this gap in scientific knowledge. To provide a basis

for the work presented in Chapter 5 and Chapter 6, the principles of ECT, 2D-FFT, and the application of both carbon fiber fabrics are discussed in this section.

Principles of eddy current testing on carbon fibers [8, 10, 15]

The physical principle by which ECT characterizes surfaces and materials is through the analysis of variations in conductivity and permeability. The schematic in Fig. 2.8 depicts the principle by which these variations are detected with a typical ECT sensor probe.

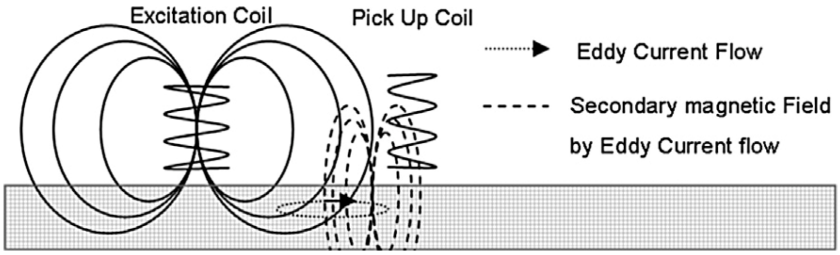

Fig. 2.8: Schematic diagram of probe and specimen configuration for ECT [10].

Alternating current in an excitation coil generates a primary magnetic field which then induces eddy currents in a nearby conductive specimen. Each eddy current subsequently generates its own secondary magnetic field. As the probe passes over the specimen, irregularities influencing the eddy current flow in the material (e.g., cracks or foreign particles) cause these secondary fields to fluctuate. A pick-up coil measures these field fluctuations (and thus the corresponding material deviations) through shifts in complex impedance values.

For ECT on carbon fiber fabrics and preforms, shifts in the measured impedance are caused by variations in fiber type, orientation, density, fiber-to-volume ratio, stacking sequence, and compaction around tows. By evaluating these measurements in the complex impedance plane and matching them to their respective geometric locations along the specimen, an ECT "image" can be generated. Figure 2.9 is an example of such an image. These images, which are effectively visualizations of the tow structure, are the foundation of ECT for carbon fiber fabrics and preforms.

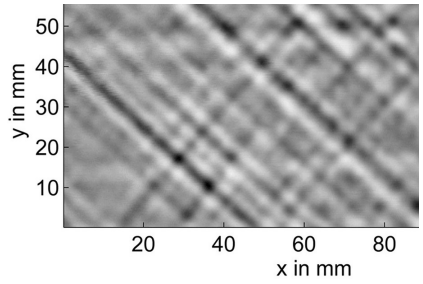

Fig. 2.9: ECT image from a four-layer quadraxial (+45/90/-45/0) carbon fiber fabric [8].

Detecting layer angles with 2D-FFT [8, 10, 15–18]

Analysis of ECT images have utilized 2D-FFT to extract details of the tow structure. In 2D-FFT, the input 2D signal is decomposed into sine functions which generate the original signal when summed with their respective frequency and amplitude [19]. This decomposition can extract periodic components of a signal; for example, the stripe pattern in Fig. 2.10 can be represented as a single sine wave with a $-45°$ angle (with the x-axis) and 0.03 mm^{-1} amplitude. The 2D-FFT in Fig. 2.10 (bottom), which is symmetrical to the origin, shows the detected frequency twice as two hotspots with the angles to the horizontal (x) axis being the pattern periodicity.

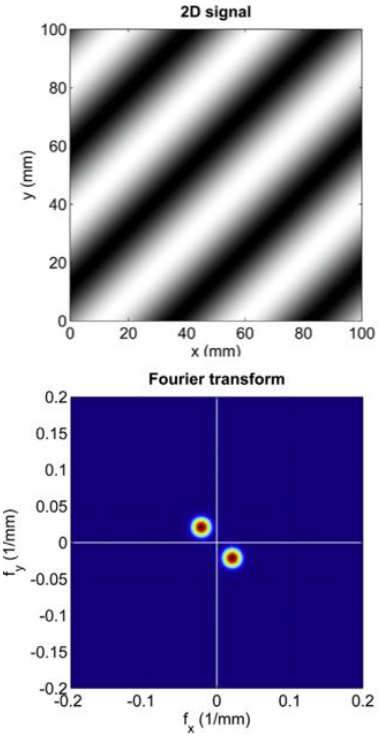

Fig. 2.10: (Top) single stripe pattern and (bottom) its 2D-FFT [8].

The underlying functionality of many subsequent experimental ECT post-processing methods depend on 2D-FFT. Directly and indirectly identifiable structural properties include fiber orientation, misalignments, waviness, and gap size distribution. Research success with 2D-FFT has even made its way to commercial ECT kits, namely SURAGUS's EddyCus® hardware/software systems.

The following work by Bardl et al. [8] represents the state of the art with respect to ECT/2D-FFT layer angle detection on dry carbon fiber. Figure 2.11 shows the ECT setup, robot-based scanning, and image construction of a hemispherically draped biaxial fabric. Figure 2.12 shows the application of 2D-FFT on a subsection of the ECT image along with an evaluation of the 2D-FFT to determine the layer angles. The detected angles presented by Bardl et al. are listed with no more than one digit after the decimal (0.1°, 0.2°, etc.). Analysis from Bardl et al. regarding uncertainty in these values is not provided.

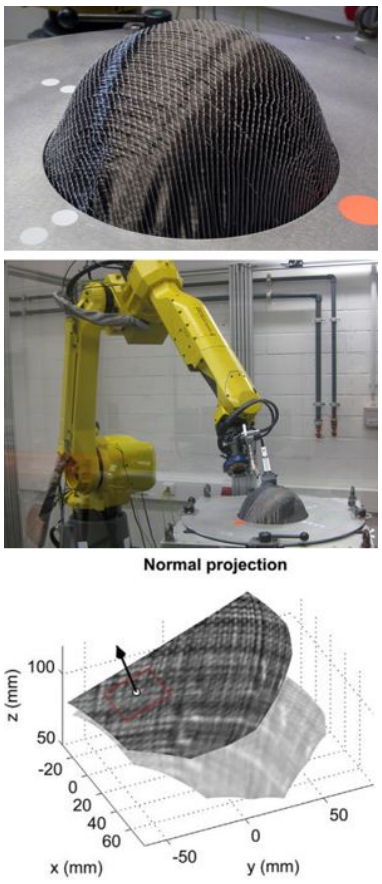

Fig. 2.11: (Top) draped biaxial fabric, (middle) robot-guided scan, and (bottom) final ECT [8].

The next step for ECT/2D-FFT in EVo

Layer angle detection in 2D preform specimens has been pursued in EVO with the same measurement approach as Bardl et al., including the use of one of the facility's robotic arms (see Fig. 2.7). ECT has also been used on frame preforms at EVO, but no layer angle analysis has been pursued. For the 2D preform layers, no reliable results (prior to the analyses made for this thesis) were ever established at EVO. The primary cause for this unreliability is the presence of mathematical flaws, namely in the existing post-processing software and the underlying algorithms.

Despite various research efforts exhibiting the layer detection of fabrics and preforms with ECT and 2D-FFT, the uncertainty of this measurement method has never explicitly been published. In addition to no defined measurement uncertainty, the algorithms which manipulate the ECT data and corresponding 2D-FFTs to extract the layer angle – like those employed by Bardl et al. – have also never been described or validated.

Methods combining ECT and 2D-FFT are documented in literature, and modern applications are quite impressive – but how can we be sure they are accurate and precise? For ECT to become a reliable quality assurance tool for tolerant-tight industries like aerospace, the uncertainty in the underlying algorithms must be investigated.

The second half of this thesis presents the first attempt to fill this gap of knowledge. Specifically, the work in Chapter 5 and Chapter 6 describes:

- the approach and validation of an algorithm to analyze 2D-FFTs;
- the analysis of various carbon fiber materials and layups; and
- the uncertainty in layer angles with respect to material and depth.

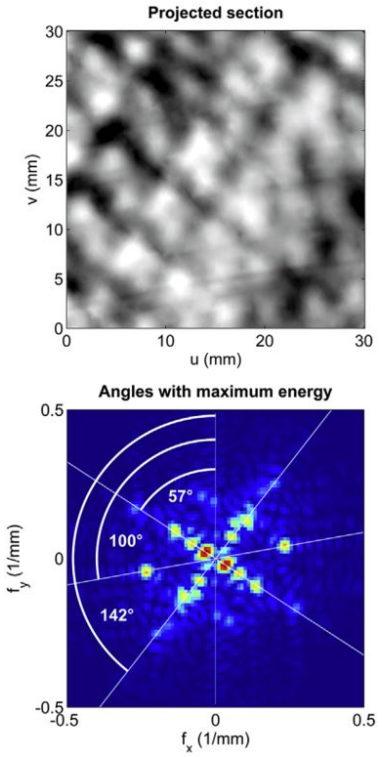

Fig. 2.12: ECT sub-image and corresponding 2D-FFT (with extracted angles) from the test in Fig. 2.11 [8].

Chapter 3

Fabric Handling: Setup and Methodology

This chapter describes the experimental setup and methodology for determining the fabric handling uncertainty of EVO, namely the error which the vacuum gripper (and related structures) introduce to the position of a given fabric cutout. The basic approach in this thesis involved measuring the position of a cutout after two gripper-based motions:

1. from the cutter table to a drawer (*cutter–drawer*); and
2. from the same drawer to the preparation table (*drawer–table*).

Figure 3.1 shows a simplified guide of these motions. These two steps mirror the general handling phase at EVO; fabric is cut from a roll on the cutter, transferred to the drawer for storage, and then brought from the drawer to the preparation table once the next step in production is ready.

The basic goal was to determine the individual uncertainty of the cutter–drawer and drawer–table handling motions; hence, the measurement trials were performed separately. In other words, for the first handling motion, the cutout was:

- "zeroed" on the cutter;
- transferred to a designated drawer;
- measured (i.e., scanned); and then
- returned to the cutter to repeat the previous steps.

The second handling motion was performed in similar fashion from the same drawer to the preparation table. Details of these steps and the corresponding setup and post-processing are described in the following sections. Chapter 4 presents and discusses the final results.

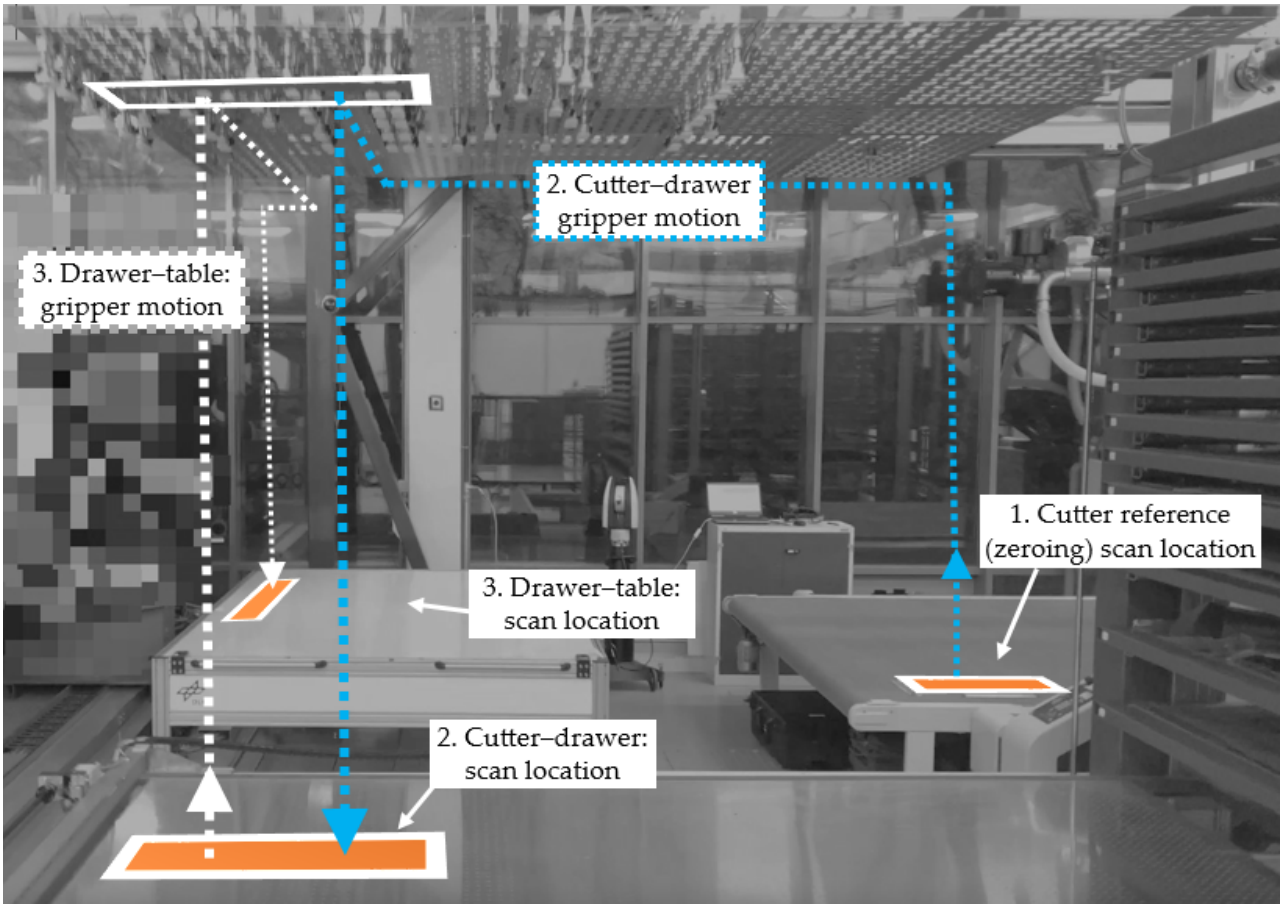

Fig. 3.1: Generalized fabric handling transfer motions and scan locations. Depicted scan area at the preparation table rotated 90° because the preprogrammed gripper motion includes a 90° rotation.

3.1 Materials and equipment

This section describes material and equipment properties used in the measurement trials for fabric handling.

Fabric cutout

Figures 3.2 and 3.3 show the fabric cutout. This is the corresponding cutout used for a type of aerospace frame produced at EVO (shown in Fig. 2.3). Table 3.1 lists the properties of this cutout.

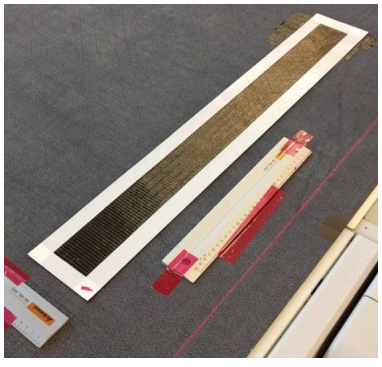

Fig. 3.2: Fabric cutout.

The specimen was cut using EVO's CNC-cutter from a sheet of unidirectional (UD; also known as *non-crimp*) biaxial carbon fiber fabric. This means the cutout consisted of two UD carbon fiber plies perpendicular to each other, one at 45° and the other at −45°, and held together with non-structural fiber binding. Although dissimilar in structure to typical woven fabrics used in aerospace-grade CFRPs, the areal weight of this non-crimp fabric is comparable to those types of weaves [20]. From a weight standpoint and based on practical experience [20], the UD biaxial material is appropriate for investigating the fabric handling steps.

The cutout as-is, i.e., directly from the fabric roll after cutting, has edges and corners which are uneven and indistinct. This indistinct edge property is caused by the exposed and loose carbon fibers. To

provide distinct, continuous edges around the cutout's outline, white opaque tape was adhered to the fabric roll prior to cutting such that both the fabric and tape were cut by the cutter. The resultant cutout had a taped outline clearly defining its edges.

Lastly, in order to track and maintain the fabric orientation during measurements, a small piece of translucent red tape was placed on one corner of the fabric.

Table 3.1: Fabric cutout properties.

Cutout property	Value
Material	Toho® Tenax Biax (single fabric sheet; two UD plies)
Areal weight	400 g/m²
Length	804 mm
Width	110 mm
Outline tape	Airtech® Airhold (fabric-reinforced; rubber-based)

Vacuum gripper

Both the cutter–drawer and drawer–table transfers used their respective preprogrammed gripper motions which already existed in EVO's automated fabric handling system. Figure 3.1 illustrates the general motions of the overhead gantry. Figure 3.3 shows how the cutout was positioned with respect to the vacuum heads on the gripper. The same head configuration was used in both motions. Just like for the physical gripper motion, the level of vacuum applied to each gripper head was set to the standard, preprogrammed value of EVO's system.

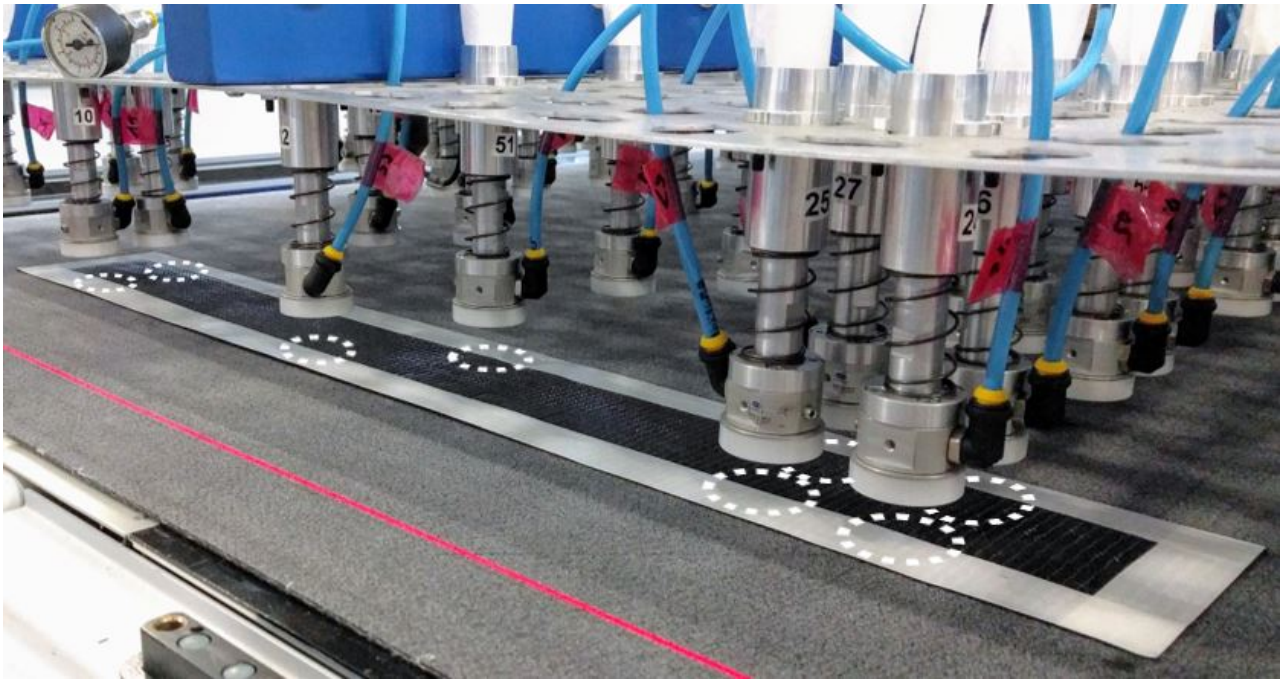

Fig. 3.3: Fabric cutout alignment to the gripper's vacuum heads.

Storage drawer

The drawer storage system in EVO consists of multiple individual drawers. The lowest-available (second-lowest)[1] drawer was chosen:

- to maximize the vertical travel of the gripper and therefore maximize the gripper movement; and
- to have the fabric cutout at an accessible height for measurement (for the cutter–drawer transfer) and zeroing (for the drawer–table transfer).

The drawer was deployed to the same position for each measurement, which was also set by EVO's preprogrammed fabric handling motions.

[1] The lowest drawer held sensitive items at the time of measurement. To prevent the risk of disturbing these items, the second-lowest drawer (which was also completely free of materials) was chosen.

Reference/zeroing base

Consistent alignment to the gripper's vacuum heads (and therefore a consistent starting reference for measurement) was guaranteed for each of the two transfer motions by way of an L-shaped "zeroing base." Figure 3.4 shows the base, which consists of two perpendicular metal rulers. Prior to each gripper transfer, the cutout was manually slid into the base, achieving both length- and widthwise (i.e., longitudinal u and lateral v) alignment.

To preserve the surface integrity of the cutter and drawer, no destructive mounting method (e.g., mechanical fasteners or glue) could be used to secure the rulers. Instead, thermoplastic tape with silicon adhesive (Nitto® PS1) was used.

The laterally aligned ruler was intentionally placed such that the reference corner (marked with an additional piece of tape) was left exposed. This exposed corner ensured that the scans made during validation of this zeroing method had unobstructed access to the reference corner's edges. The uncertainty which is introduced to the cutout's position through this zeroing method is documented in the results in Section 4.2.

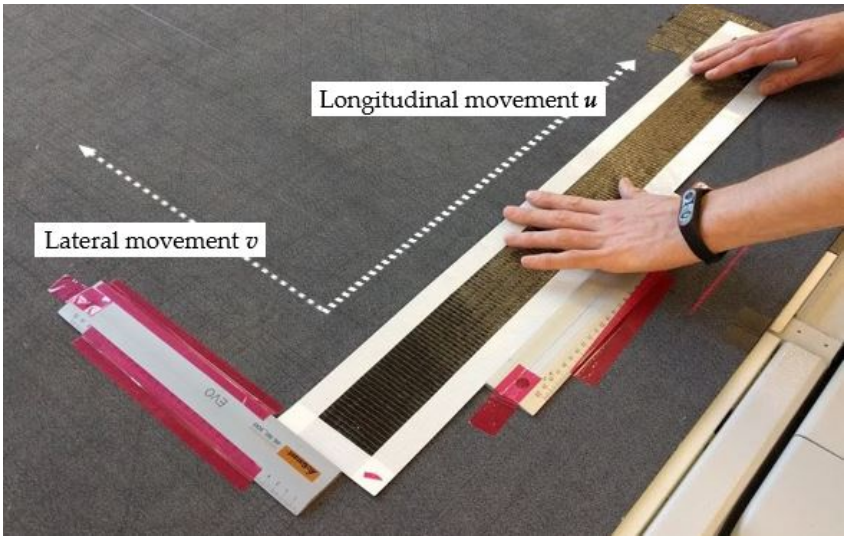

Fig. 3.4: Zeroing base into which the cutout was slid before each transfer with the gripper. Design was intended to ensure the same starting reference position, thus "zeroing" the cutout.

3D laser scanner

A Leica® laser scanner and corresponding tracker were used to capture the position of the fabric cutout during measurement. Figure 3.5 shows the paired scanning equipment, and Table 3.2 lists their respective specifications.

Fig. 3.5: Laser scanner and tracker with base.

The "product" of the laser scanner is a collection of 3D points, or *point cloud*, describing the location of the detected surface relative to the laser tracker. Figure 3.6 illustrates the 3D point cloud capture of a gloved hand. The generalized process of surface scanning with the laser system is as follows:

- A band of laser light is projected from the scanner, which then (using reflection) calculates the distance between surface and scanner at points along the laser band.
- The tracker (using an array of lasers) simultaneously determines the position and orientation of the scanner.
- The 3D location of each scanned point (relative to the tracker) are collected and represented as a point cloud.

InnovMetric's® PolyWorks | Inspector™ software was used in both the measurement (to capture the scanned points) and in the post-processing analysis steps.

The advantage of measuring the cutout with a laser scanner is that no complex mechanical measurement system needs to be constructed,

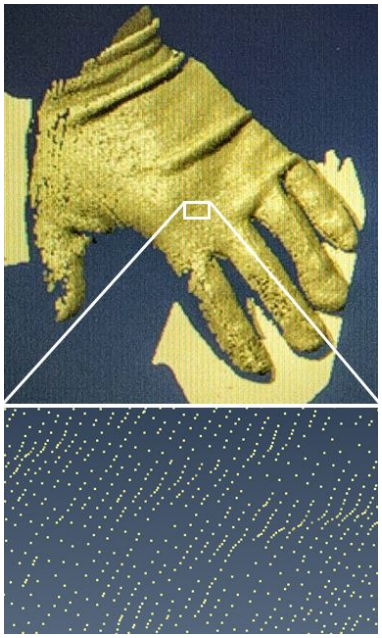

Fig. 3.6: 3D point cloud obtained by scanning a gloved hand. Variations in point color are purely aesthetic, and do not represent point density.

and the inherent no-contact measurement means the cutout does not need to be physically touched. Using a laser scanner also provides the opportunity (as presented in this thesis) to develop a novel method of determining the position of a fabric cutout from its 3D point cloud.

The tape placed around the cutout's edges was specifically chosen for its opacity and reflectivity. Preliminary scans showed that this tape's detectibility was stable in the sense that no reflective artifacts or jittery points along the taped surface appeared in the scanned 3D point clouds.

Before each measurement trial, the laser tracker base was leveled using the internal leveling meter. The laser itself was also first brought to the operating temperature as set by the automatic internal temperature gauge. Both the tracker and scanner were always powered (i.e., constantly "on"), and the tracker was left untouched in the same position for all measurements of each step.

Leica® laser measurement equipment [21, 22]	
Scanner	T-Scan 5
Tracker	Absolute AT960
Point density	0.075 mm

Table 3.2: Laser scanning system properties. The provided uncertainty is for scans made within an 8.5 m radius of the tracker. All measurements made in the scope of this thesis were within an 8.5 m range.

3.2 Experimental steps

This section describes each trial of the experimental procedure for determining the uncertainty in fabric handling using the materials and equipment as specified in the previous section.

Trial 0: Validation of edge-fit corner calculation

Before measurements can be made, the methodology for calculating the fabric position from a 3D scan must be defined. This step combines the manipulation of point cloud data and geometric analysis to bridge the gap between experimental measurements (i.e., the scans) and the final uncertainty values of which we seek.

Likewise, the uncertainty in the calculation of the fabric's position must be isolated in order to determine if the uncertainties of the zeroing method and the gripper transfers are significant. The specific methodology of this experimental step is provided in Section 3.3, and the validation of this method is presented in Section 4.1.

Trial 1: Reference position

The purpose of the first trial is to determine the translational and rotational uncertainty introduced by the zeroing base to the fabric cutout. Isolating the uncertainty in the reference position is necessary to determine if the uncertainty in the gripper transfers is significant. This trial was only made on the cutter table because it is assumed that the uncertainty in the reference position is equal for both the cutter and drawer surfaces.

The measurement procedure of this reference position trial was designed to reproduce the referencing of the cutout in the zeroing base. The specific steps are:

1. Manually place the fabric cutout in the reference position on the cutter table using the zeroing base such that edges are flush with the metal rulers.
2. Scan the edges of the cutout at each exposed corner.
3. Lift and remove the cutout from the reference position.
4. Repeat steps 1.–3. until 30 scans are collected.

Trial 2: Cutter to drawer

The purpose of the second trial is to determine the translational and rotational uncertainty introduced to the fabric cutout by the cutter–drawer transfer. The measurement procedure steps are:

1. Manually place the fabric cutout in the reference position on the cutter table using the zeroing base.
2. Transfer the cutout from cutter to drawer with the vacuum gripper.
3. Scan the cutout on the surface of the open drawer.
4. Lift and remove the cutout from the drawer.
5. Repeat steps 1.–4. until 30 scans are collected.

Trial 3: Drawer to table

The purpose of the third trial is to determine the translational and rotational uncertainty introduced to the fabric cutout by the drawer–table transfer. The measurement procedure steps are:

1. Manually place the fabric cutout in the reference position on the drawer using the zeroing base.
2. Transfer the cutout from drawer to preparation table with the vacuum gripper.
3. Scan the cutout on the surface of the table.
4. Lift and remove the cutout from the table.
5. Repeat steps 1.–4. until 30 scans are collected.

3.3 Calculating the relative position of the fabric cutout

Determining the fabric handling uncertainty requires comparing the cutout's location after multiple trials of the gripper transfer. The defined method of measurement is through the use of a laser scanner. But how do we determine the relative position of each cutout from a cloud of 3D points? To find the answer, we will employ a set of simplifications and geometric manipulations. This section presents this methodology, and Section 4.1 presents the validation.

Simplification to the horizontal plane

Because all steps of the fabric handling process begin and end on flat surfaces, the fabric's position after each transfer can be described

as movement in a 2D plane. In other words, we will assume that the fabric is a 2D shape whose deviation in placement position is within the 2D plane it defines. Figure 3.7 illustrates this approach. With regards to mass, it is assumed that the fabric's mass is spread uniformly across the 2D shape.

Simplifying the fabric cutout from 3D to 2D likewise reduces the degrees of freedom, namely from six degrees (i.e., translation in/rotation about three axes) to three degrees (i.e., translation in u and v, and rotation about w as θ). In the same vein of assumptions, we will define the uv translation and θ rotation as that of the fabric's center of mass – which, by definition, is the shape's centroid [23].

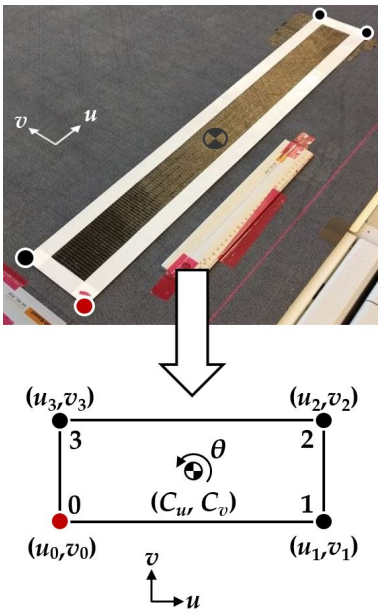

Fig. 3.7: Representation of the cutout in the uv plane.

Calculating the fabric centroid

With the fabric's relative position defined as the location of its centroid in the uv plane, the next question is posed: How can we calculate the centroid? To simplify the solution, the fabric is assumed to be a four-sided polygon (i.e., a quadrilateral) defined by its four vertices. Figure 3.7 visualizes this simplification alongside the corresponding corners of the actual fabric cutout.

The centroid of a non-intersecting polygon in the uv plane defined by n vertices $(u_0, v_0), (u_1, v_1), ..., (u_{n-1}, v_{n-1})$ is the point (C_u, C_v), where [23]

$$C_u = \frac{1}{6A} \sum_{i=0}^{n-1} (u_i + u_{i+1})(u_i v_{i+1} - u_{i+1} v_i) \tag{3.1}$$

and

$$C_v = \frac{1}{6A} \sum_{i=0}^{n-1} (v_i + v_{i+1})(u_i v_{i+1} - u_{i+1} v_i), \tag{3.2}$$

with the polygon's signed area A as

$$A = \frac{1}{2} \sum_{i=0}^{n-1} (u_i v_{i+1} - u_{i+1} v_i). \tag{3.3}$$

In eqs. (3.1)–(3.3), the vertices are assumed to be numbered in their order around the polygon. The vertex (u_n, v_n) in eqs. (3.1)–(3.3) is the same as (u_0, v_0), hence closing the vertex loop around the polygon.

By applying eqs. (3.1)–(3.3) to the uv coordinates of the fabric cutout's corners, the centroid of that cutout – and therefore the assumed position of that cutout – can be calculated. Despite the simplicity of this calculation, determining each corner's location requires an additional level of mathematical manipulation with the measured 3D surface data.

Determining the fabric corners from a cloud of points

By definition, a point has no area. Assuming each corner of the cutout is a point hence implies each corner has no area. In contrast, the scanner's band of laser light relies on reflection from a discrete area, and therefore (theoretically) can never provide the true location of the

corner. The "corner" which seems to appear in the 3D point cloud is a point which – albeit very close to the true corner location – deviates from that corner by a certain amount.

For the measurements and corresponding post-processing this thesis seeks to pursue, this false-corner effect means that a single point cannot be trusted. In other words, it means we cannot simply select what appears to be the corner points from each set of scans and define them as the cutout's corners. Instead, an indirect method of defining each corner is presented. Figure 3.8 illustrates the method.

Applying the definition that each vertex of a polygon is the intersection of its neighboring edges, the proposed method of defining each corner (i.e., each vertex) is to calculate the intersection of the neighboring edges. These edges are hence defined as lines, and are to be determined by fitting a linear line to a subset of the point cloud, namely the points which lay along the nearby edge.

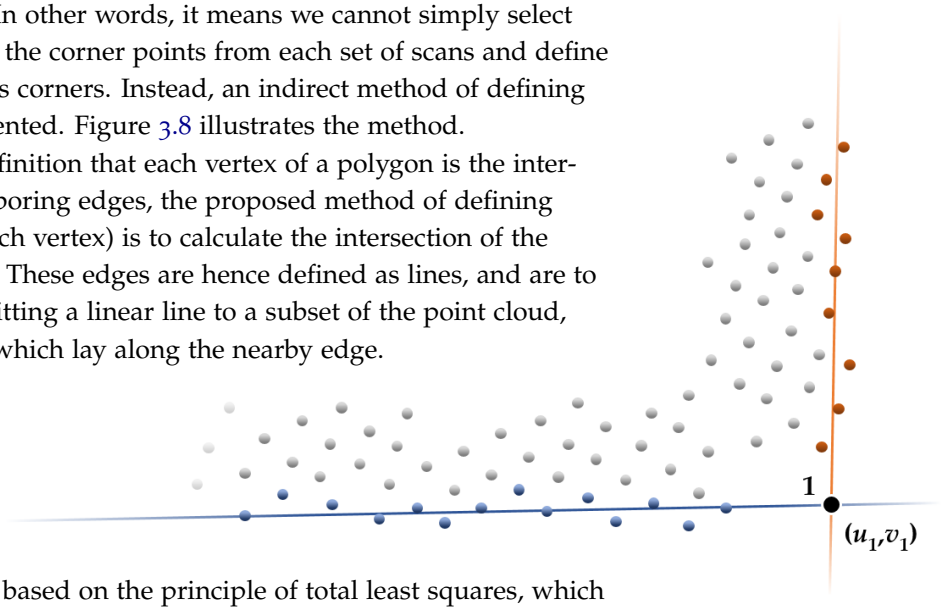

Fig. 3.8: Illustration of the edge-fit intersection method to determine the corner location.

The fitted line is based on the principle of total least squares, which is also known as the linear case of orthogonal regression [24]. This type of linear fit minimizes the perpendicular distance from each point to the fitted model [25], and is appropriate here because each variable (i.e., each spatial coordinate x, y, and z) is measured with error [24][2].

To summarize the proposed corner determination method, figures are provided of an example scan (see Fig. 3.9 and 3.10). The steps for determining a corner i's position (u_i, v_i) from the 3D scan of a given fabric cutout scan are:

1. Select a subset of the point cloud which belongs to one of the neighboring edges of corner i (Fig. 3.11)
2. Fit the points based on the principle of total least squares
3. Repeat 1. and 2. for the other neighboring edge
4. Set the intersection of the two lines as (u_i, v_i), the corner's vertex location (Fig. 3.12)

[2] See [24, 25] for the mathematical background of total least squares

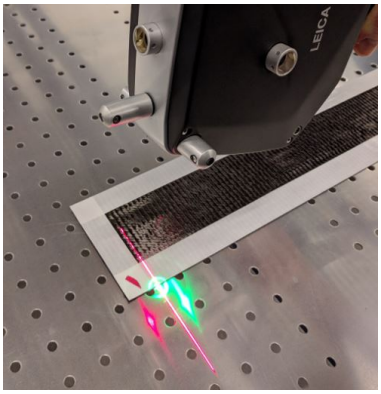

Fig. 3.9: Scanning procedure for corner determination.

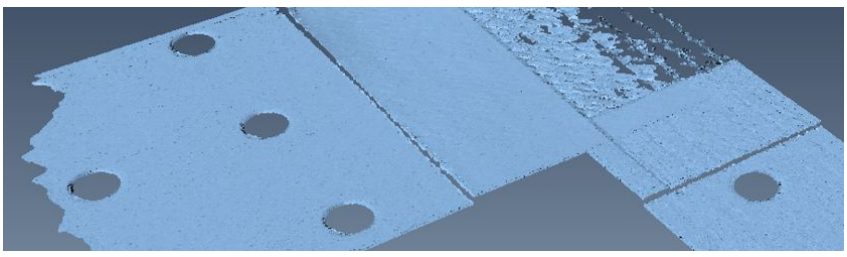

Fig. 3.10: Resultant scan from Fig. 3.9.

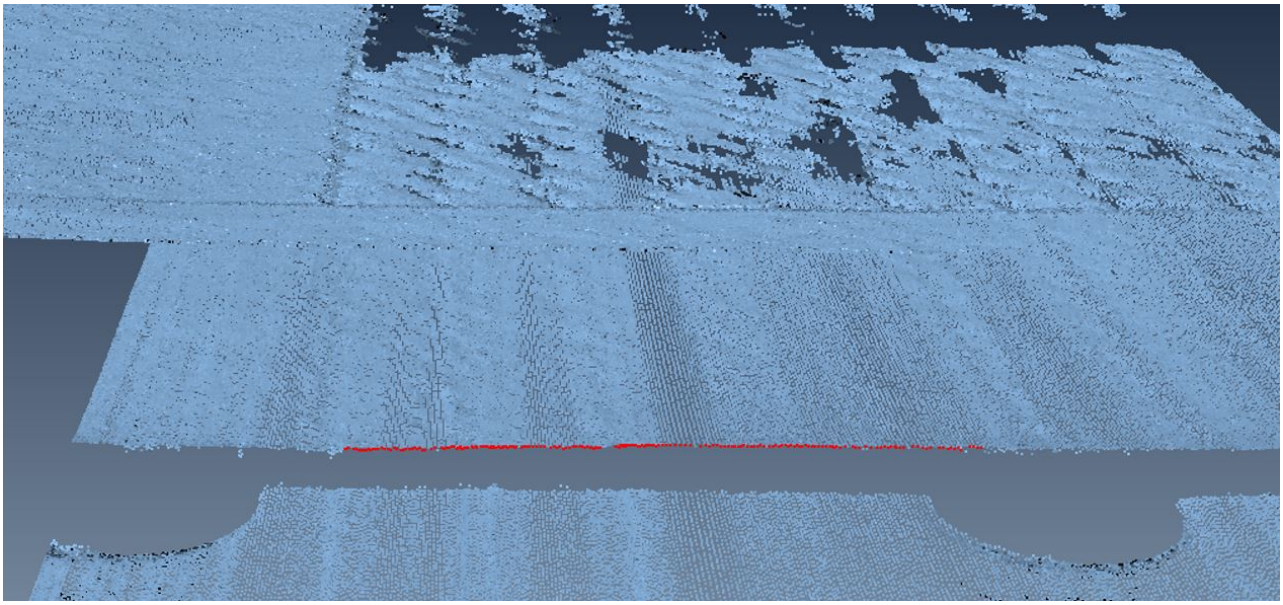

Fig. 3.11: Selected edge points for fitting from the scan in Fig. 3.10. Points are selected away from the corner to prevent deviation from bent and/or lifted corners.

The validation of this proposed edge-fit-based corner finding methodology is presented in Section 4.1.

Determining translational uncertainty

Validating the fitted-edge intersection method depends on calculating the uncertainty from a set of 2D corner points derived using the fitted-edge method. Therefore, before pursuing this validation, we must first explain how the position uncertainty from a set of 2D points can be calculated. Following this explanation, a way to define the translational and rotation uncertainty from a set of corner measurements is presented.

This thesis uses the sample standard deviation[3] σ to describe uncertainty. The coordinate-specific standard deviations σ_x and σ_y of a set of N measured 2D points $\{(x_1, y_1), (x_2, y_2), ..., (x_N, y_N)\}$ are [26]

$$\sigma_x = \sqrt{\frac{\sum_{j=1}^{N}(x_j - \bar{x})^2}{N-1}} \tag{3.4}$$

and

$$\sigma_y = \sqrt{\frac{\sum_{j=1}^{N}(y_j - \bar{y})^2}{N-1}}, \tag{3.5}$$

where $\bar{x}$ and $\bar{y}$ are the respective arthimetic means

$$\bar{x} = \frac{1}{N}\sum_{j=1}^{N} x_j \tag{3.6}$$

and

$$\bar{y} = \frac{1}{N}\sum_{j=1}^{N} y_j. \tag{3.7}$$

The individual standard deviations σ_x and σ_y describe the uncertainty in their respective directions, e.g., for longitudinal and

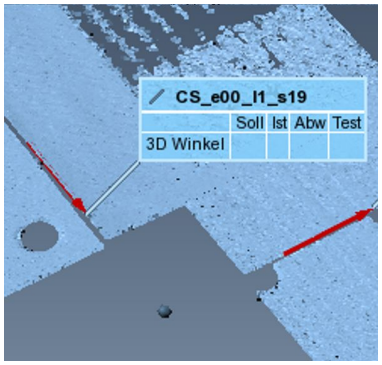

Fig. 3.12: Edge-fitted lines and intersection-based corner vertex.

[3] Though sometimes represented in literature by s, the use of σ in this thesis implies the $N-1$ sample standard deviation.

lateral movement in a given fabric cutout j's centroid $(C_{u,j}, C_{v,j})$. But what if we want an uncertainty value which is independent of a coordinate system's direction? In other words, how can we describe the uncertainty of a set of 2D points with a single value?

The answer comes from combining σ_x and σ_y into one "planar uncertainty" – σ_{xy}. The following text (with visualization in Fig. 3.13) help to understand the combination of these two into a single reportable uncertainty in fabric translation.

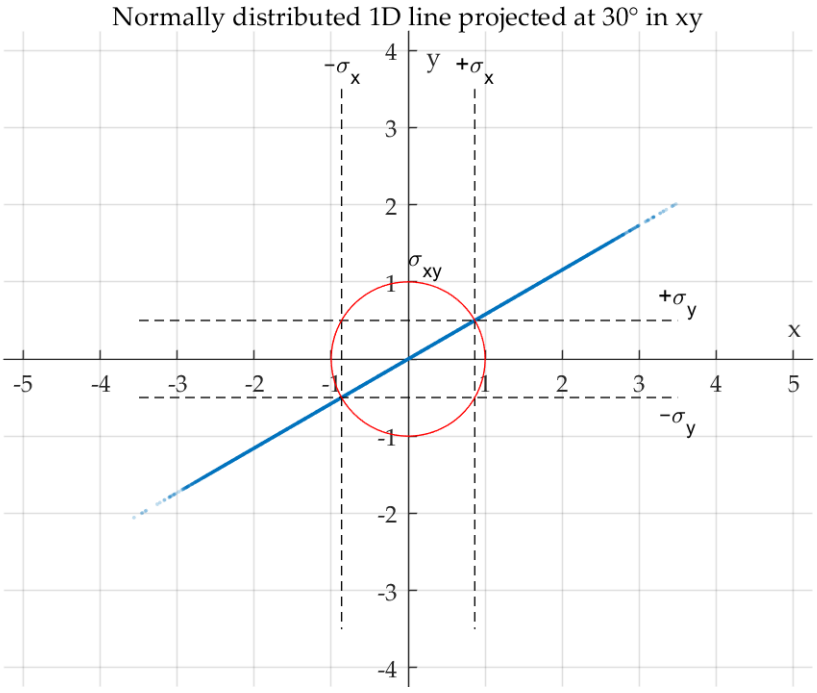

Fig. 3.13: A set of 100,000 normally distributed values along a line projected in the xy plane at 30° to the x-axis.

Take a set of points in 1D which are distributed according to the standard normal distribution. This is to say, take a set of points along a line whose mean is zero and standard deviation is 1. Project this line of points onto a 2D plane at an arbitrary angle such that the mean is at the origin. Figure 3.13 shows an example of such a line at 30° with the x-axis.

The absolute distance of the overall standard deviation σ_{xy} of this (now 2D) set of points remains 1. The xy components of σ_{xy} are σ_x and σ_y, as defined in eqs. (3.4) and (3.5). The relationship between these two coordinate-specific deviations and the overall deviation per Pythagorean theorem is therefore

$$\sigma_{xy} = \sqrt{\sigma_x^2 + \sigma_y^2}. \tag{3.8}$$

In summary, this means that while the individual coordinate standard deviations σ_x and σ_y may vary when a given set of normally distributed 2D points is rotated, the overall xy (i.e., coordinate-independent) standard devation of those points remains constant. Hence, by adjusting eqs. (3.4)–(3.7), the overall translational uncertainty for the centroid σ_{uv} (i.e., the translational uncertainty of

the fabric cutout) of a set of N centroids $\{(C_{u,1}, C_{v,1}), (C_{u,2}, C_{v,2}), \ldots, (C_{u,N}, C_{v,N})\}$ is calculated with

$$\sigma_{uv} = \sqrt{\sigma_u^2 + \sigma_v^2}, \tag{3.9}$$

where the longitudinal and lateral deviations of the centroid σ_u and σ_v, respectively, are

$$\sigma_u = \sqrt{\frac{\sum_{j=1}^{N}(C_{u,j} - \bar{C_u})^2}{N-1}}, \tag{3.10}$$

and

$$\sigma_v = \sqrt{\frac{\sum_{j=1}^{N}(C_{v,j} - \bar{C_v})^2}{N-1}}, \tag{3.11}$$

where the longitudinal and lateral arthimetic mean of the centroids $\bar{C_u}$ and $\bar{C_v}$, respectively, are

$$\bar{C_u} = \frac{1}{N}\sum_{j=1}^{N} C_{u,j} \tag{3.12}$$

and

$$\bar{C_v} = \frac{1}{N}\sum_{j=1}^{N} C_{v,j}. \tag{3.13}$$

Determining rotational uncertainty

Rotational uncertainty in the fabric handling steps is likewise determined through the deviation in rotation of the cutout. Figures 3.14 and 3.15 illustrate the following steps to determine the individual relative rotation – and the subsequent complete uncertainty of those rotations σ_θ – for a set of N scanned cutouts.

The basic premise is to first negate the relative translations by normalizing the respective centroid of each scan such that all centroids lie at the point $(0, 0)$. Then, using the "rotationally pure" scans, the angle between each corner vertex and the corresponding average vertex (with respect to the origin) is calculated. The standard deviation of these angle differences for corners 0–3 is calculated, and the average of the four corner angle deviations ($\sigma_{\theta,0}$, $\sigma_{\theta,1}$, $\sigma_{\theta,2}$, and $\sigma_{\theta,3}$) provides the rotational uncertainty of the cutout transfer – σ_θ.

The specific steps to determine the σ_θ of a set of N cutout scans is as follows:

1. Determine the centroids $(C_{u,j}, C_{v,j})$ of each cutout scan by using the corner vertices 0–3 (from the intersection method) and eqs. (3.1)–(3.3).

2. Subtract each scan's set of vertices by its respective centroid to negate the relative translation, thus generating a set of N' translationally normalized scans whose centroids all lie at $(0, 0)$ (see Fig. 3.14):

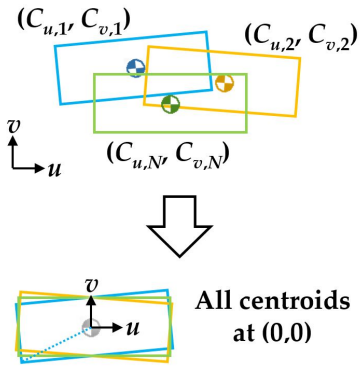

Fig. 3.14: Illustration of the centroid normalization (i.e., negation of relative translation) for the determination of cutout rotation.

$$\left\{ \ (u'_{0,j}, v'_{0,j}), (u'_{1,j}, v'_{1,j}), (u'_{2,j}, v'_{2,j}), (u'_{3,j}, v'_{3,j}) \ \right\} =$$
$$\left\{ \ (u_{0,j}, v_{0,j}), (u_{1,j}, v_{1,j}), (u_{2,j}, v_{2,j}), (u_{3,j}, v_{3,j}) \ \right\} - (\bar{C_{u,j}}, \bar{C_{v,j}})$$

(3.14)

where $(u_{0,j}, v_{0,j})$, $(u_{1,j}, v_{1,j})$, $(u_{2,j}, v_{2,j})$, $(u_{3,j}, v_{3,j})$ are the vertex coordinates of the j^{th} scanned cutout, and $(u'_{0,j}, v'_{0,j})$, $(u'_{1,j}, v'_{1,j})$, $(u'_{2,j}, v'_{2,j})$, $(u'_{3,j}, v'_{3,j})$ are the centroid-normalized vertices.

3. As illustrated in Fig. 3.15, at each corner i, calculate the angles $\{\theta'_{i,1}, \theta'_{i,2}, ..., \theta'_{i,N'}\}$ between the average of the normalized vertices $(\bar{u_i}', \bar{v_i}')$ and each individual normalized vertex $(u'_{i,j}, v'_{i,j})$ with respect to the origin, where

$$\bar{u_i}' = \frac{1}{N'} \sum_{j=1}^{N'} u'_{i,j} \tag{3.15}$$

and

$$\bar{v_i}' = \frac{1}{N'} \sum_{j=1}^{N'} v'_{i,j}. \tag{3.16}$$

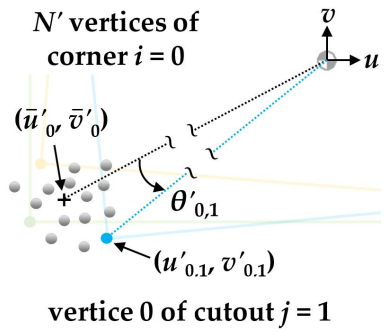

Fig. 3.15: Illustration of the relative rotation calculation for corner 0.

4. Calculate the uncertainty of each corner i's angles $\sigma_{\theta,i}$ with

$$\sigma_{\theta,i} = \sqrt{\frac{\sum_{j=1}^{N'} (\theta'_{i,j} - \bar{\theta_i}')^2}{N' - 1}} \tag{3.17}$$

and

$$\bar{\theta_i}' = \frac{1}{N'} \sum_{j=1}^{N'} \theta'_{i,j}. \tag{3.18}$$

5. Finally, find the average of the four corner uncertainties, i.e., the rotational uncertainty σ_θ of the original set of N scanned cutouts

$$\sigma_\theta = \frac{1}{4}(\sigma_{\theta,0} + \sigma_{\theta,1} + \sigma_{\theta,2} + \sigma_{\theta,3}). \tag{3.19}$$

Chapter 4

Fabric Handling: Results

This chapter presents and discusses the fabric handling results for each of the four trials:

- **Trial 0**: Validation of the edge-fit method for determining the cutout corners (which are then used to calculate the cutout's centroid and relative position), and the definition of the associated translational uncertainty σ_{uv0} and rotational uncertainty $\sigma_{\theta 0}$.
- **Trial 1**: Calculation of the error introduced to the fabric cutout when zeroed in the reference position, presented as the translational uncertainty σ_{uv1} and rotational uncertainty $\sigma_{\theta 1}$.
- **Trial 2**: Calculation of the error introduced to the fabric cutout when transferred with the gripper from the cutter to a storage drawer, presented as the translational uncertainty σ_{uv2} and rotational uncertainty $\sigma_{\theta 2}$.
- **Trial 3**: Calculation of the error introduced to the fabric cutout when transferred with the gripper from the drawer to the preparation table, presented as the translational uncertainty σ_{uv3} and rotational uncertainty $\sigma_{\theta 3}$.

4.1 Trial 0: Validation of edge-fit corner calculation

To determine the uncertainty in fabric handling, the position of a fabric cutout specimen must be analyzed across multiple instances of the same handling motion. Calculating the position – defined in this thesis as the centroid of the quadrilateral-simplified cutout – relies on the position of the cutout vertices.

In Chapter 3, we defined how to determine the relative translation and rotation of a given scanned cutout along with the corresponding 2D translational uncertainty σ_{uv} and rotational uncertainty σ_θ of a set of cutout scans; however, all of these evaluations are dependent on the calculation of the corner points (i.e., the vertices) with the edge-fit intersection method. This section presents the validation of this corner-finding methodology.

The first step of the validation involved scanning one corner of the cutout 50 times without moving the cutout. Then, the corners were

calculated for each of the 50 scans. Lastly, the translational uncertainty and a psuedo rotational uncertainty of that corner were determined by applying the equations in Section 3.3. This validation provides uncertainty values which describe the error of the corner calculation method itself, thus providing a benchmark for the fabric zeroing and handling steps.

Cutout scanning

The first step in the corner calculation validation involved scanning one corner of the (unmoved) cutout in 50 individual scans. To reduce jittery and noisy edge artifacts in the point cloud, the scanner was held slightly inboard (relative to the cutout) and pitched such that the laser band pointed slightly outboard. This encouraged a "shadow effect"[1] along the edge, thus minimizing light scatter in the transition from the fabric edge and underlying surface.

Figure 4.1 (top) shows a scan with noisy edges, a result of the scanner being held perpendicular to the surface. Figure 4.1 (bottom) shows a scan with clean edges, a result of the inboard-held, outboard-pitched laser scanning technique. This technique was implemented for all subsequent trials in the fabric handling uncertainty investigation.

[1] An exaggerated example of this shadow effect scan be seen in the scanned hand in Fig. 3.6

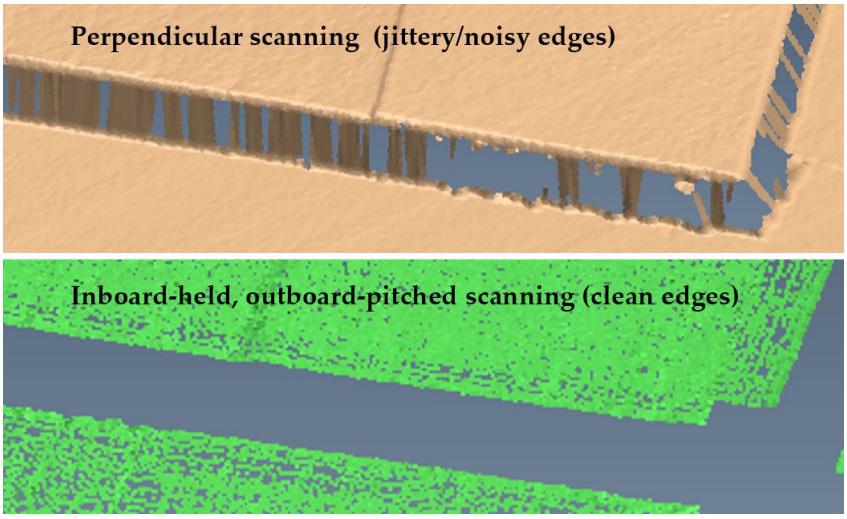

Fig. 4.1: Edge quality from (top) perpendicular scanning and (bottom) inboard-held, outboard-pitched scanning. The noisy edges seen in the top point cloud are mitigated through the shadowing effect, which is encouraged by holding the scanner at an angle.

Edge fitting and corner intersecting

The next step in validating the corner finding method involved fitting the corner edges for each of the 50 scans. The intersections of these edge pairs were then used to obtain the vertex coordinates. Figure 4.2 shows a scan along with all fitted edges and intersected points. Figure Y shows a zoomed view of the leftside edges.

The points used for the edge fit[2] were purposefully selected with an offset from the true corner. Why the offset? Like the pages of a book, the corners of the cutout are suspectible to bending and lifting. If the edges are fit to points directly next to the corner, the error from the bent/lifted corners is introduced. Hence, the points were selected with an offset to descrease this effect.

[2] A more detailed description of the edge point selection process is provided in Section 3.3.

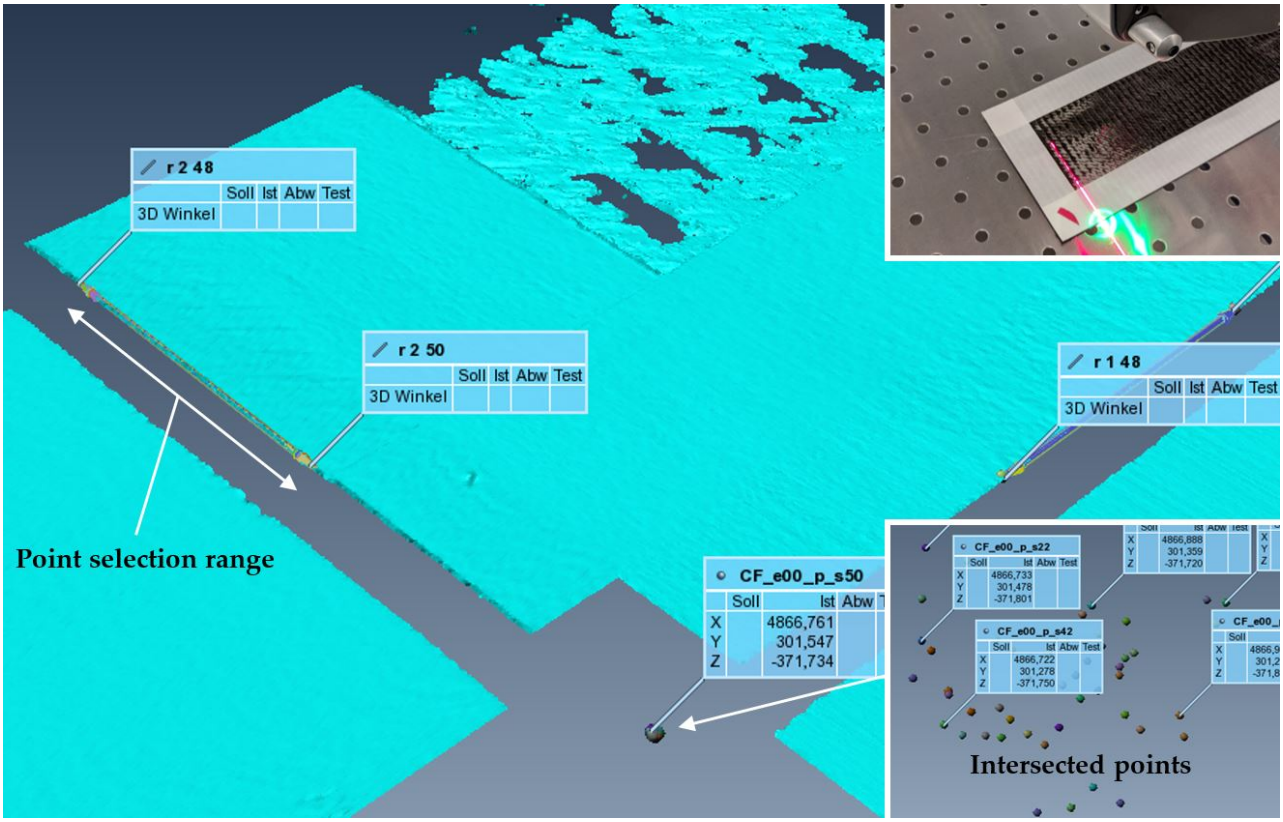

Fig. 4.2: Example scan from the corner finding validation trial.

The selected line of points for each edge started just outside the tape-overlap, and then extended away from the corner until a length equal to the tape width (1 inch; 2.54 cm) was reached. The length and position of the edge selection was maintained throughout the validation and all subsequent fabric handling trials.

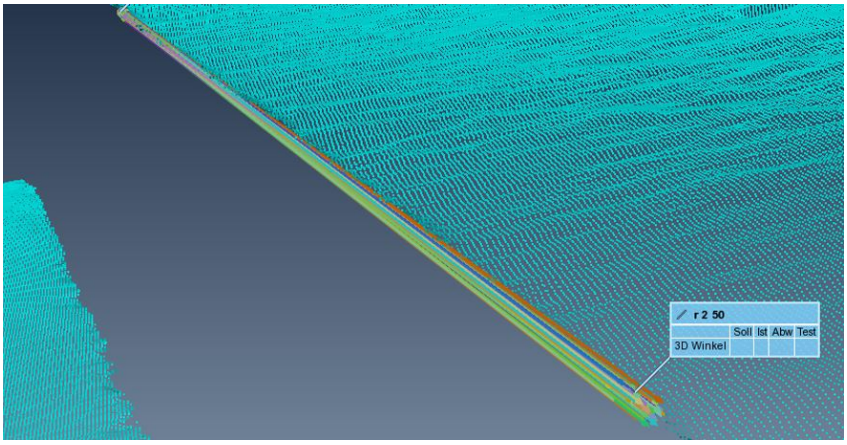

Fig. 4.3: Zoomed perspective view of the leftside edge from the scan in Fig. 4.2 showing all 50 edges.

Translational and psuedo rotational uncertainty

Figure 4.4 shows the 50 corner points in the uv plane (the surface upon which the cutout was placed), where the average of the points is centered to the origin for ease of data analysis. With the planar coordinates uv of the 50 intersection-based corner vertices known,[3] the planar translational uncertainty σ_{uv0} and rotational uncertainty $\sigma_{\theta 0}$ of the corner fit method were calculated using the equations presented in Section 3.3.

[3] The x and y components of the corner points were set to u and v, respectively.

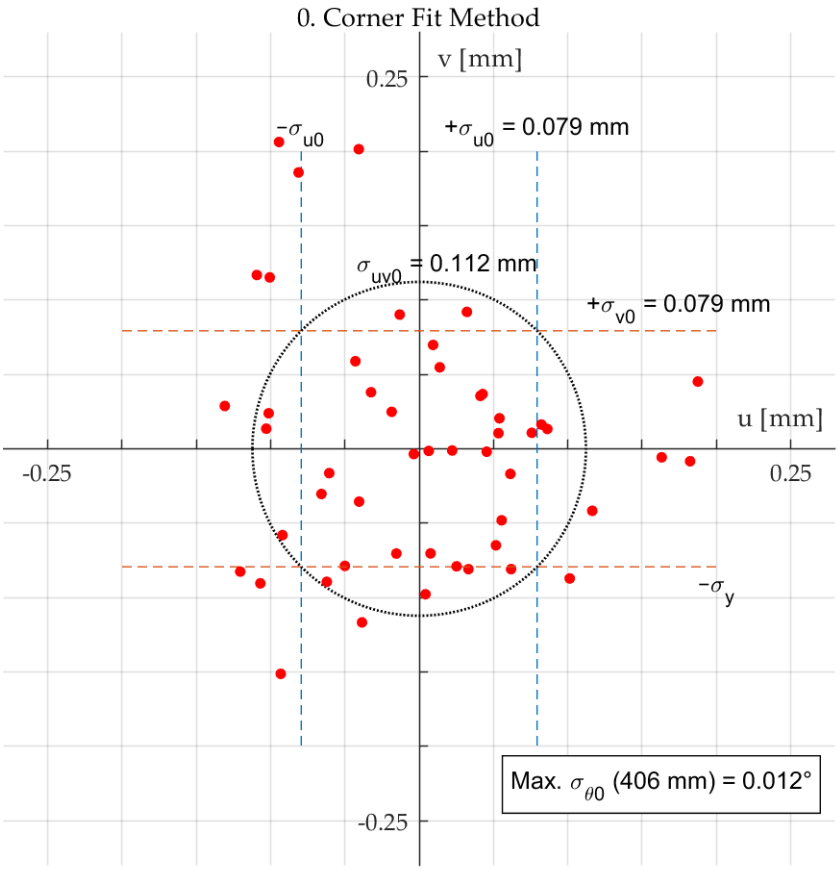

Fig. 4.4: Edge-fit corner intersection validation points in the uv plane, where the average of the points is at the origin.

The (apparent) even scattering of points in both directions signifies an even spread of corner points. The σ_{u0} and σ_{v0} values provide the planar uncertainty σ_{uv0}, which is 0.112 mm. This means that the corner fit method is able to define the location of a given cutout's corner with an uncertainty of 0.112 mm. Subsequently, this is the same uncertainty in the calculation of the centroid, and therefore is the benchmark with which the fabric handling stages can be compared.

The rotational uncertainty $\sigma_{\theta 0}$ is a pseudo uncertainty derived by placing an imaginary centroid 406 mm (half the cutout's diagonal length) from the points, calculating $\sigma_{\theta 0}$ per Section 3.3, and then rotating the centroid about the origin (and recalculating $\sigma_{\theta 0}$) until the maximum rotation uncertainty is reached. The value, 0.012°, tells us that the corner fit method introduces an uncertainty of 0.012° to the calculated relative rotation of a scanned cutout.

Summary of Trial 0

The validation of the corner fit method in Trial 0 revealed a variety of items:

- **An optimal scanning method**: To obtain point cloud scans of the cutout with reduced edge noise and point jitter, the scanner can be held inboard of the cutout and pitched outboard, encouraging a shadowing effect along the edge.
- **Inherent planar uncertainty**: The corner fit method introduces a planar uncertainty σ_{uv0} of 0.112 mm to a given corner calculated in a point cloud scan. This uncertainty provides a benchmark for the translational uncertainty in later trials for both the corners and subsequent centroids. That is to say, the planar uncertainty along a fabric handling step (analyzed with the method in this thesis) is expected to be at least 0.1122 mm. If the uncertainty is greater, it indicates that the fabric handling step may introduce an additional level of error to a given cutout's translational position.
- **Inherent rotational uncertainty**: The scattered corner points display a worst-case rotational uncertainty $\sigma_{\theta 0}$ of 0.012°. This value is also a benchmark for the analysis of later trials, but in this case an uncertainty to compare with the centroid rotation. That is to say, the rotational uncertainty along a fabric handling step is expected to be at least 0.012°. If the uncertainty is greater, it indicates that the handling step may introduce an additional level of error to a given cutout's rotational position.

4.2 Trial 1: Reference position

With the uncertainty in the corner fit method defined, we now turn our attention to the results of Trial 1: the uncertainty introduced to the fabric cutout when zeroed in the reference position before each run in Trials 2 and 3.

Coordinate system transformation

The corner points directly from the software's point cloud are coordinates described by x, y, and z, and are therefore not aligned with the cutout's longitudinal and lateral axes, u and v. For the results to be interpreted with respect to the general orientation of the cutout, these corner points must be aligned with the uv plane. The steps of this process are as follows:

- The average of the corner points at vertex 0 (the lower-left corner when seen from above) was set to the origin. This means that all points were translated such that the average coordinate of vertex 0 was at $(0, 0, 0)$.
- The direction of the vector pointing from the origin to the average of the corner points at vertex 1 (the lower-right corner) was set to

the longitudinal (side-to-side) axis. This means that the points were rotated such that the average coordinate of vertex 1 was directly along the u-axis.

- The direction of the vector perpendicular to u passing through the average of the corner points at vertex 2 (the upper-right corner) was set to the lateral (back-and-forth) axis. This means that the points were rotated such that the average coordinate of vertex 2 was directly along the v-axis.

Modified centroid calculation

In the scans for Trial 1 – where the cutout was repeatedly aligned against the two metal rulers in the reference position – the lateral edge of vertex 3 displayed large amounts of noise and jitteriness because of its proximity to one of the rulers. Because a line fit to this edge would not be stable, no corner points for vertex 3 were generated. This meant that instead of having four corners to calculate the centroid for each scan for Trial 1, only three corners (vertices 0, 1, and 2) could be used. The modified centroid calculation for each cutout scan was made by averaging two sets of coordinates:

1. the average uv coordinates of vertices 0 and 2 (i.e., the diagonal corner pair); and
2. the average u coordinate of vertices 0 and 1 (i.e., the bottom corner pair) and the average v coordinate of vertices 1 and 2 (i.e., the right-side corner pair).

This averaging across the three vertex coordinates ensured the corners had "weight" to the subsequent centroid. The rotational uncertainty (which in Section 3.3 is defined as the average of the four corner rotations) was likewise determined by averaging the relevant rotation from the three existing corners.

Translational uncertainty introduced by zeroing

Figure 4.5 shows the centroid coordinates (31 points from 31 scans on the cutter's reference position) in the uv plane, where the average of the centroids is normalized to the origin. The blue and red bars show the coordinate-specific uncertainties σ_{u1} and σ_{v1}, respectively. The outer circle has a radius equal to the planar translational uncertainty of the centroid, σ_{uv1}, which is 0.188 mm. The inner circle has a radius equal to σ_{uv0} (0.112 mm) for reference with the corner fit method.

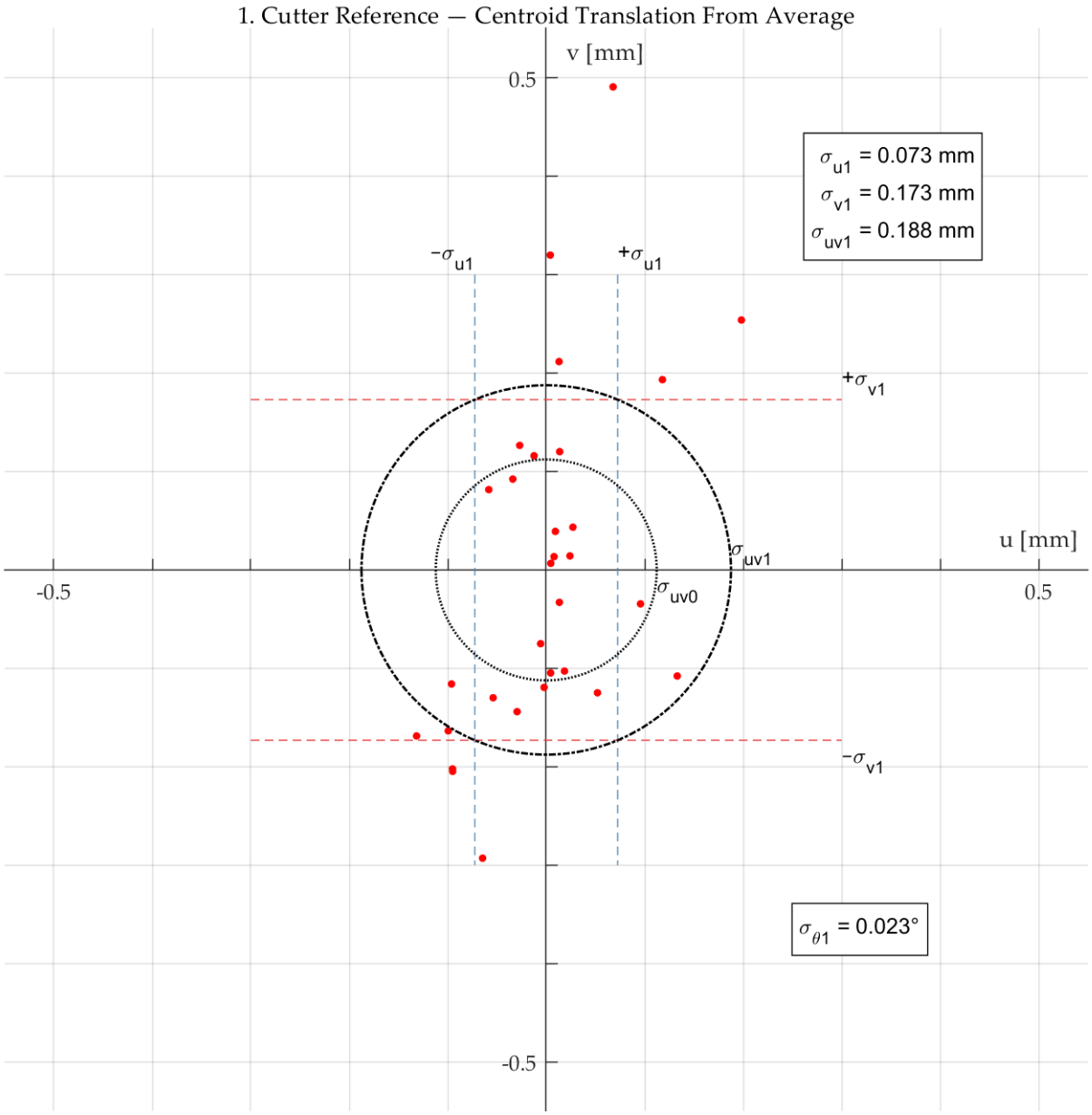

Fig. 4.5: Centroids in the uv plane from the reference position measurements, where the average of the points is at the origin. The outer circle indicates the translational uncertainty of the zeroing method, while the inner circle indicates the uncertainty from the corner fit method σ_{uv}.

Rotational uncertainty introduced by zeroing

Figure 4.6 shows the results of the rotational deviation/uncertainty analysis on the cutout reference trial. The deviations of individual corner rotations for each scan (see legend) are plotted against a thick horizontal line, which denotes the resultant rotational uncertainty $\sigma_{\theta 1}$ (0.023°) of those values. For comparison with the corner fit method analysis in Trial 0, a thin horizontal line denotes the corresponding rotational uncertainty $\sigma_{\theta 0}$ (0.012°).

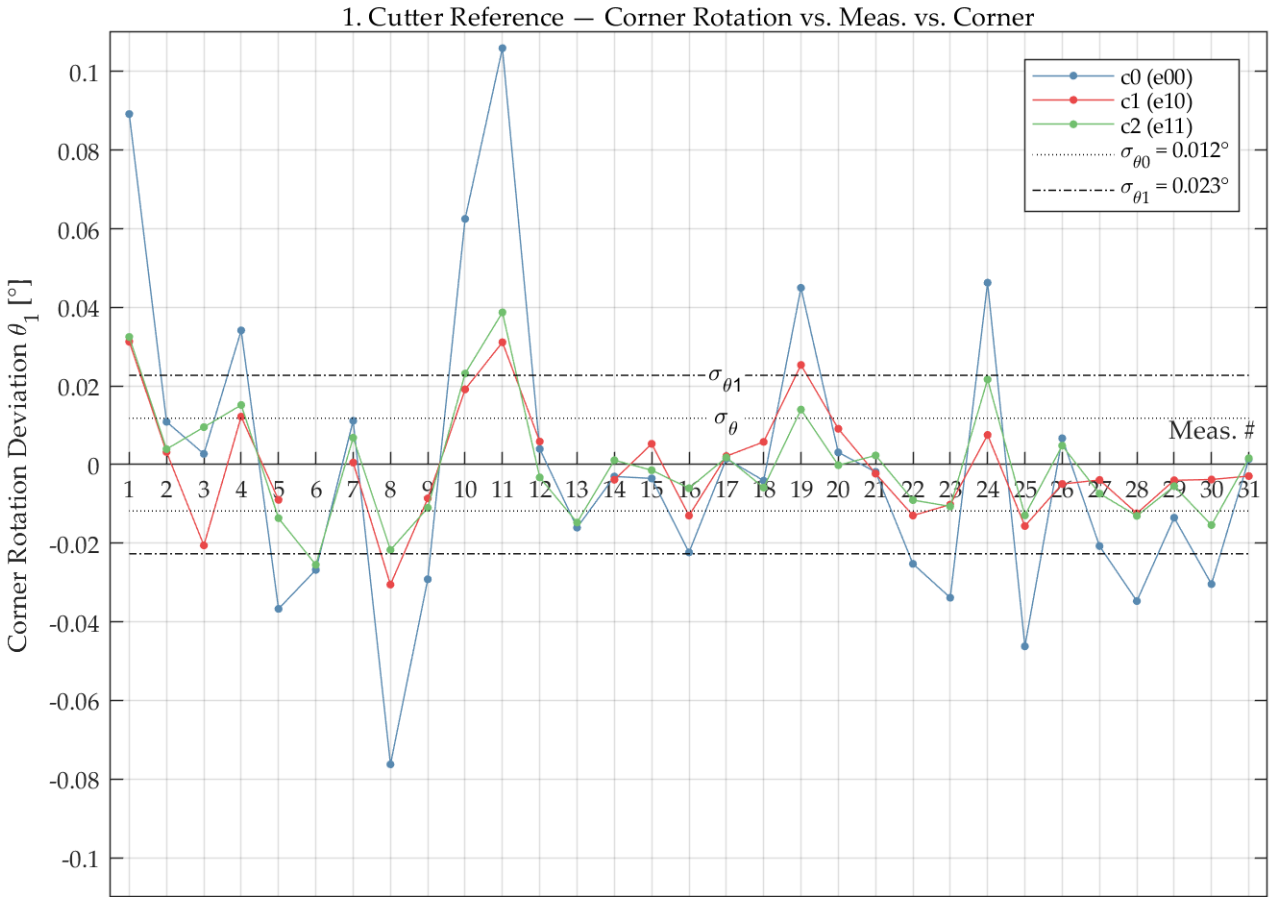

Fig. 4.6: Results of the rotational deviation/uncertainty for corners 0–2 of the 32 scans. The resultant rotational uncertainty in the cutout $\sigma_{\theta 1}$ – which is the average of the individual corner uncertainties – is shown as a thick line. The corresponding uncertainty from Trial 0 is shown as a thin line for reference.

Summary of Trial 1

The uncertainty investigation of the zeroing method in Trial 1 revealed a variety of items:

- **Difference between longitudinal and lateral uncertainty**: The difference between the cutout's longitudinal side-to-side deviation (σ_{u1} = 0.073 mm) and lateral back-and-forth deviation (σ_{v1} = 0.173 mm) is notable. This denotes a level of lateral deviation in the zeroing method. The cause of this deviation may stem from play in the metal rulers, or perhaps the friction on the cutter surface interferes with the sliding of the cutout.
- **Referencing introduces additional uncertainty**: Because σ_{uv1} and $\sigma_{\theta 1}$ are larger than their respective values from the corner fit method, the referencing method can be said to introduce an additional and detectable uncertainty in the cutout's position. In other words, when the cutout is zeroed in the reference position, there then exists an inherent translational uncertainty of 0.188 mm and rotational uncertainty 0.023° in that cutout's position.
- **Consistency in individual scan rotations**: Figure 4.6 supports the observation that the individual rotations calculated for corner vertices 0–2 appear consistent within individual scans. For a given scan, the relative rotations for each corner tend to "agree"; that is

to say, when one of the vertices'relative rotation is positive, then all other vertices belonging to that scan are also positive. If the relative rotation lies inside the uncertainty bars, this all-positive/all-negative tendency does not hold. Nevertheless, the correlative nature between individual corner rotations does offer validation to the proposed rotation calculation.

4.3 Trial 2: Cutter to drawer

Trial 2 of the uncertainty analysis in fabric handling focused on measuring the uncertainty introduced to the cutout when transferred from the cutter to the drawer using the vacuum gripper. The cutter–drawer results here inherently carry the uncertainty from both the edge-fit corner finding method and the reference position zeroing.

Translational uncertainty introduced from cutter to drawer

Figure 4.7 shows the centroid coordinates (32 points from 32 scans on the open drawer) in the uv plane, where the average of the centroids is normalized to the origin. The blue and red bars show the coordinate-specific uncertainties σ_{u2} and σ_{v2}, respectively. The outer circle has a radius equal to the planar translational uncertainty of the centroid, σ_{uv2}, which is 0.218 mm. The inner circle has a radius equal to σ_{uv0} (0.112 mm) for reference with the corner fit method.

Rotational uncertainty introduced from cutter to drawer

Figure 4.8 shows the results of the rotational deviation/uncertainty analysis on the cutter–drawer trial. The deviations of individual corner rotations for each scan (see legend) are plotted against a thick horizontal line, which denotes the resultant rotational uncertainty $\sigma_{\theta 2}$ (0.026°) of those values. For comparison with the corner fit method analysis in Trial 0, a thin horizontal line denotes the corresponding rotational uncertainty $\sigma_{\theta 0}$ (0.012°).

Summary of Trial 2

The uncertainty investigation of the cutter-drawer transfer in Trial 2 revealed a variety of items:

- **Longitudinal/lateral uncertainty slightly differ**: The difference between the cutout's longitudinal side-to-side deviation (σ_{u2} = 0.172 mm) and lateral back-and-forth deviation (σ_{v2} = 0.133 mm) is notable, albeit not as significant as Trial 1. This seems to denote a level of both longitudinal and lateral deviation during the cutter–drawer transfer. The cause of this deviation could stem from numerous sources in EVO's handling mechanisms.

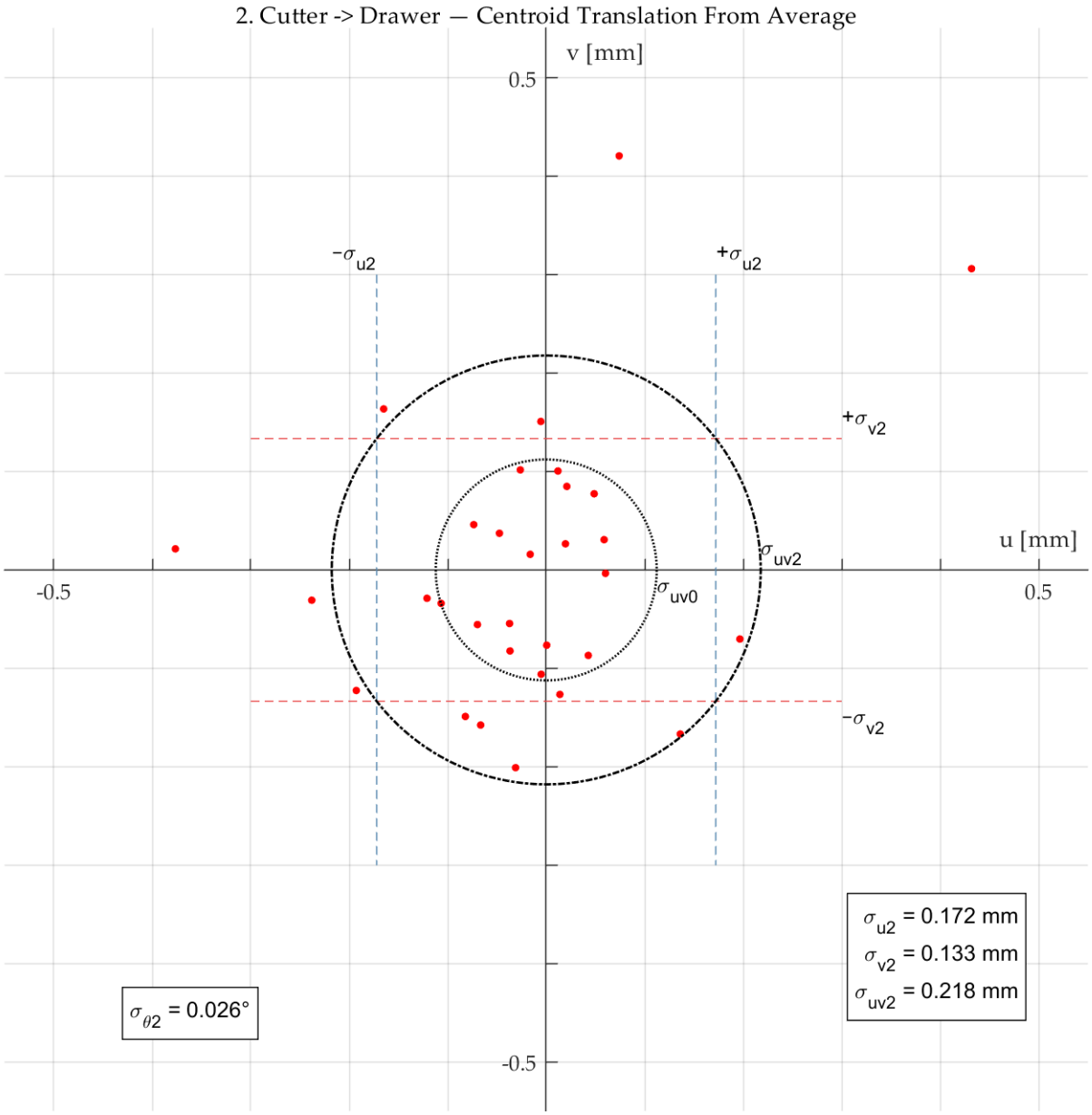

Fig. 4.7: Centroids in the uv plane from the cutter–drawer measurements, where the average of the points is at the origin. The outer circle indicates the translational uncertainty of the cutter–drawer transfer, while the inner circle indicates the uncertainty from the corner fit method σ_{uv}.

- **Gripper transfer may introduce uncertainty**: Because σ_{uv2} and $\sigma_{\theta 2}$ are larger than their respective values from the referencing method, the gripper transfer may introduce an additional and detectable uncertainty in the cutout's position when moved from the cutter to the drawer. Based purely on the larger uncertainty values, when the cutout is transferred from the cutter to the drawer, there then exists an inherent translational uncertainty of 0.218 mm and rotational uncertainty 0.026° in that cutout's position.
- **Further corner rotation consistency**: Figure 4.8 supports the observation that the individual rotations calculated for corner vertices 0–3 appear consistent within individual scans. Just as in Trial 1, the relative rotations for the corners of a given scan tend to follow each other. Again, if the relative rotation lies inside the uncertainty bars, this all-positive/all-negative tendency does not

hold. Nevertheless, the correlative nature between individual corner rotations in Trial 2 further supports the analysis approach made in this thesis.

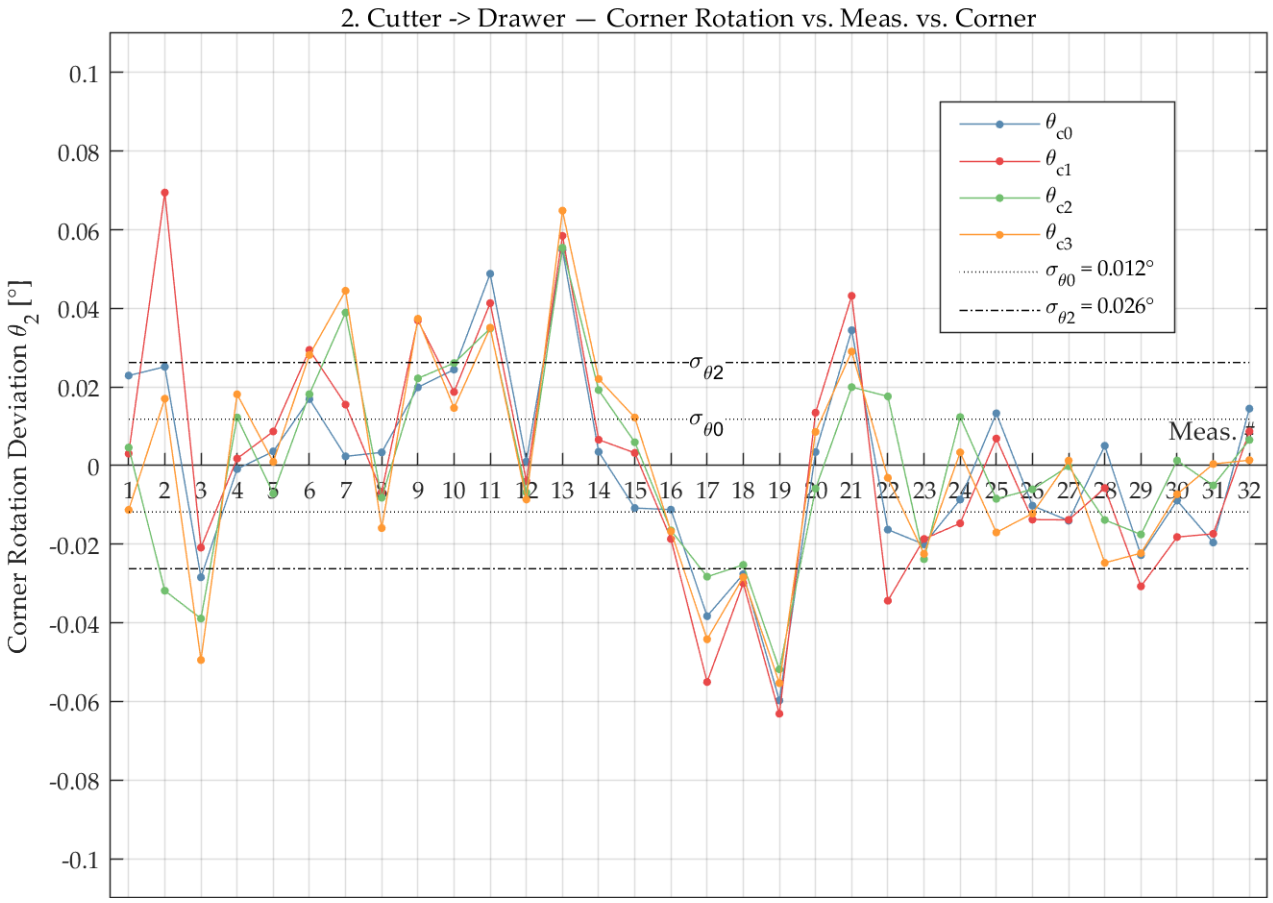

Fig. 4.8: Results of the rotational deviation/uncertainty for corners 0–3 of the 31 scans. The resultant rotational uncertainty in the cutout $\sigma_{\theta 2}$ – which is the average of the individual corner uncertainties – is shown as a thick line. The corresponding uncertainty from Trial 0 is shown as a thin line for reference.

4.4 Trial 3: Drawer to table

Trial 3 of the uncertainty analysis in fabric handling focused on measuring the uncertainty introduced to the cutout when transferred from the drawer to the preparation table using the vacuum gripper. The drawer–table results here inherently carry the uncertainty from both the edge-fit corner finding method and the reference position zeroing, but do not carry the cutter–drawer uncertainty because the analysis was made independent of this transfer.

Translational uncertainty introduced from drawer to table

Figure 4.9 shows the centroid coordinates (34 points from 34 scans on the table), where the average of the centroids is normalized to the origin. The blue and red bars show the coordinate-specific uncertainties σ_{u3} and σ_{v3}, respectively. The outer circle has a radius equal to the translational uncertainty of the centroid, σ_{uv3}, which is 0.161 mm. The inner circle has a radius equal to σ_{uv0} (0.112 mm) for reference with the corner fit method.

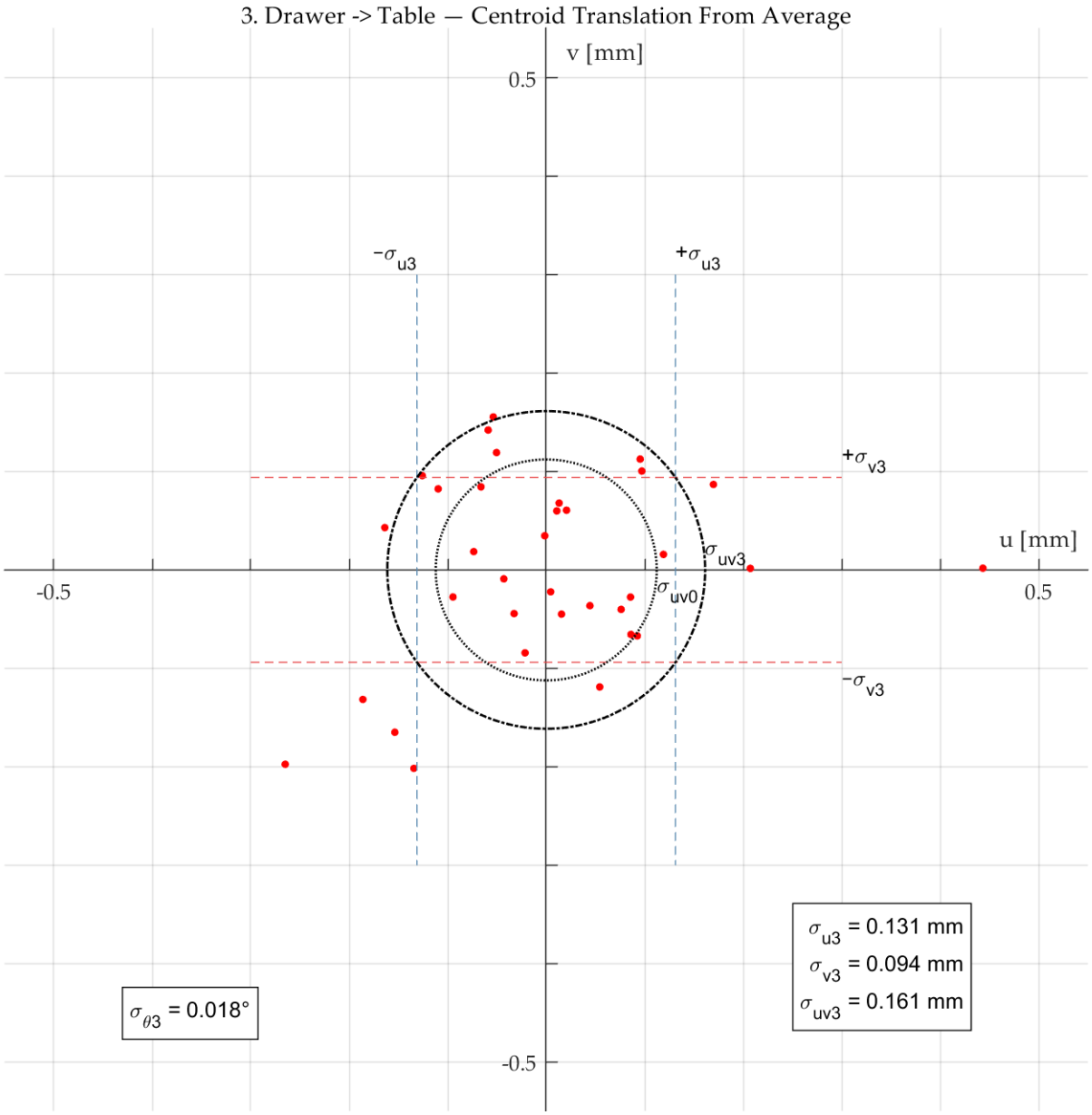

Fig. 4.9: Centroids in the uv plane from the drawer–table measurements, where the average of the points is at the origin. The outer circle indicates the translational uncertainty of the drawer–table transfer, while the inner circle indicates the uncertainty from the corner fit method σ_{uv}.

Rotational uncertainty introduced from drawer to table

Figure 4.10 shows the results of the rotational deviation/uncertainty analysis on the drawer–table trial. The deviations of individual corner rotations for each scan (see legend) are plotted against a thick horizontal line, which denotes the resulant rotational uncertainty $\sigma_{\theta 3}$ (0.018°) of those values. For comparison with the corner fit method analysis in Trial 0, a thin horizontal line denotes the corresponding rotational uncertainty $\sigma_{\theta 0}$ (0.012°).

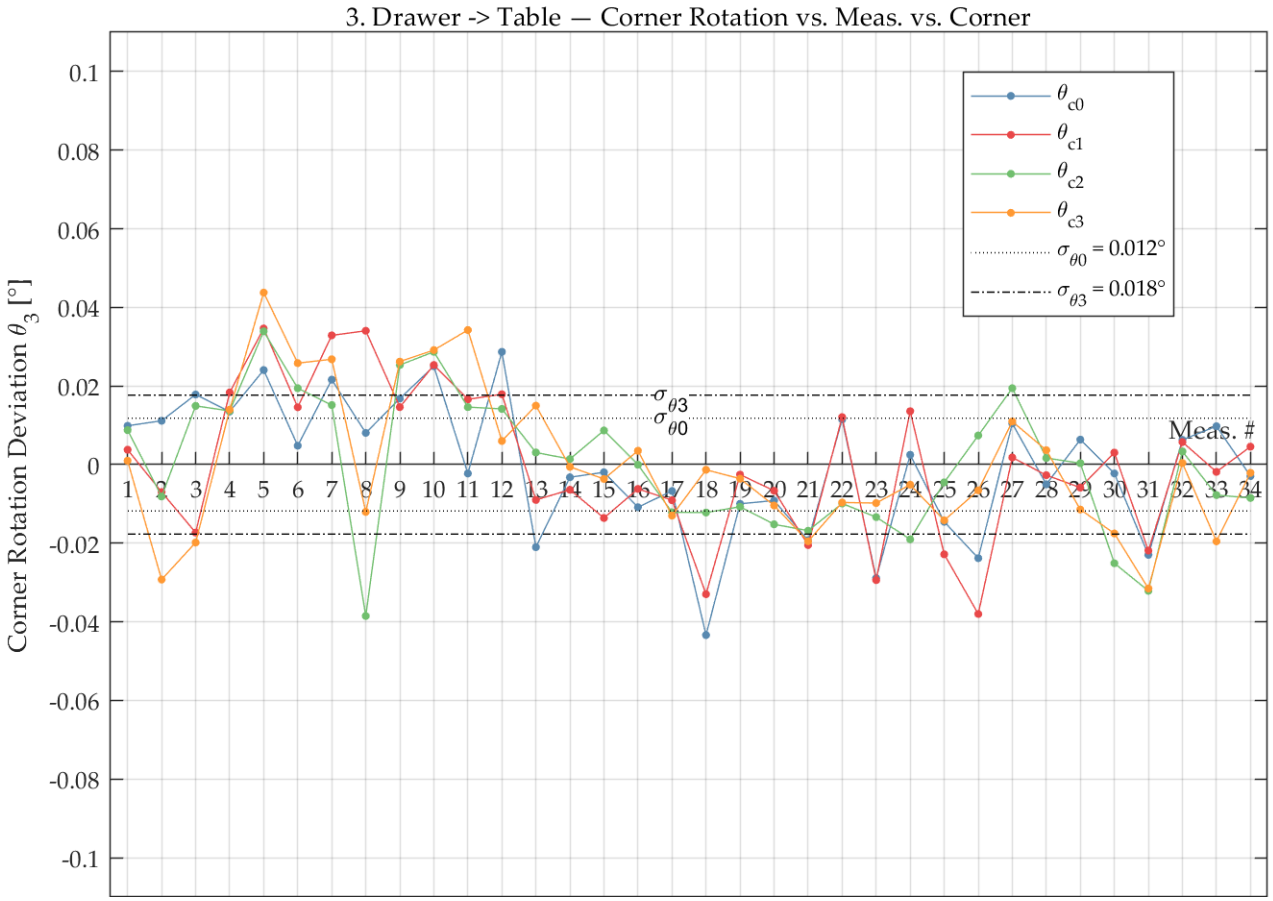

Fig. 4.10: Results of the rotational deviation/uncertainty for corners 0–3 of the 34 scans. The resultant rotational uncertainty in the cutout $\sigma_{\theta 3}$ – which is the average of the individual corner uncertainties – is shown as a thick line. The corresponding uncertainty from Trial 0 is shown as a thin line for reference.

Summary of Trial 3

The uncertainty investigation of the cutter-drawer transfer in Trial 2 revealed a variety of items:

- **Uncertainty lower than Trial 1**: The cutout's longitudinal side-to-side deviation (σ_{u3} = 0.131 mm) is notably larger than that of Trial 1's deviation (σ_{u1} = 0.073 mm); however, the lateral back-and-forth deviation (σ_{v3} = 0.094 mm) is notably lower than that of Trial 1 (σ_{v1} = 0.173 mm). The total planar translational uncertainty σ_{uv3} is also lower than that of Trial 1 (0.161 mm versus 0.188 mm, respectively).
- **Further corner rotation consistency**: Figure 4.10 supports the observation that the individual rotations calculated for corner vertices 0–3 appear consistent within individual scans. Just as in Trials 1 and 2, the relative rotations for the corners of a given scan tend to follow each other.

4.5 Summary: Fabric handling uncertainty

At the beginning of this thesis, the fabric handling uncertainty analysis was posed in the form of a question:

> *Do the deviations in fabric movement exceed the measurement uncertainties – and if so, how large are these deviations?*

Table 4.1 lists the uncertainties from each of the fabric handling trials, and from these results, we can see that the planar translational and rotational uncertainties in Trials 1, 2, and 3 are all larger than the corresponding uncertainties from the measurement uncertainties of Trial 0's edge-fit analysis.

Table 4.1: Fabric handling results from all trials.

	Translational			
	Longitud.	Lateral	Planar	Rotational
Uncertainty	σ_u (mm)	σ_v (mm)	σ_{uv} (mm)	σ_θ
Trial 0: Corner fit	0.079	0.079	0.112	0.012°
Trial 1: Ref. position	0.073	0.173	0.188	0.023°
Trial 2: Cutter–drawer	0.172	0.133	0.218	0.026°
Trial 3: Drawer–table	0.131	0.094	0.161	0.018°

So, to answer the initial question: Yes, the deviations in the trials with fabric movement appear to exceed the measurement uncertainties introduced by the laser-scan-based, edge-fit corner point calculation method. However, the results from these trials show a few peculiarities.

Firstly, the uncertainties from Trials 1–3 are all still within the same order of magnitude as those from Trial 0. In other words, the measured uncertainty of the zeroing method and gripper-based fabric transfers are not significantly larger than the uncertainty of the measurement method.

Secondly, the planar translational uncertainty and rotational uncertainty from Trial 2's cutter–drawer transfer are greater than Trial 1 – but Trial 3's drawer–table transfer uncertainties are *lower* than those from Trial 1. This reduced uncertainty implies that one or both of the following is true:

1. **Zeroing in the reference position on the drawer is more accurate**: The analysis of the zeroing method in Trial 1 was performed on the cutter, which has a carpet-like surface. While the zeroing of the cutout for Trial 2 was also made on the cutter, the cutout in Trial 3 was instead zeroed on the smooth metallic surface of the drawer. The cutout was slid against L-aligned rulers when zeroed, so it is plausible that the drawer's smooth surface encouraged better alignment.

2. **The reference position uncertainty is lower than measured**: The uncertainty analysis of the zeroing method was made with a modified centroid calculation with just three vertices, as the fourth vertex could not be derived due to disturbed 3D point

clouds. Therefore, the final centroid uncertainties (translational and rotational) for Trial 1 may actually be inflated from the true values.

In the same vein of inconsistent zeroing, the individual longitudinal and lateral translation uncertainties for Trials 2 and 3 do not reflect the lateral-heavy deviation from Trial 1. Again, this inconsistency may lie in the reference position and/or the measurement process itself.

The primary observation – that the measured values deviate in the same magnitude as the measurement uncertainty itself – suggests that the results here in this thesis were highly influenced by the measurement process, and that the above observations are (at least partially) a product of said process. In short, it means a more accurate method to analyze the position of fabric cutouts must be developed to make more rigid claims about the uncertainty in fabric handling at EVO. No compounded uncertainty is therefore provided.

Nevertheless, the relatively small uncertainty values from this analysis show that EVO's fabric handling systems are capable of transporting carbon fiber cutouts with translational tolerances well below 1 mm with a rotational tolerance also well below 1°.

Chapter 5

Layer Angle Detection: Setup and Methodology

This chapter presents the setup and methodology for the detection of layer angles in carbon fiber preforms with eddy current testing (ECT) and 2D fast Fourier transformation (2D-FFT) methods. First, the construction and ECT analysis of preforms from previous work is reviewed. Next, a new method to extract angles from the 2D-FFT's of ECT images is proposed. Lastly, a set of preliminary analyses covering specific parameters is presented. The following chapter presents the results of the application of the proposed method on the existing preform measurements.

5.1 Preform specimens and ECT procedure

The ECT data (from carbon fiber preform specimens) which is analyzed in this thesis was predominantly obtained[1] in previous work from Hienz and Buelow (2017, [27]). Because the preparation of these preforms and the subsequent ECT measurement (i.e., the preform *scanning*) is comprehensively described in the work from Heinz and Buelow, this thesis provides only a review of these experimental steps. The author directs readers to the original work for full details.

[1] Except for one additional specimen made in the scope of this thesis.

Preform specimens

The ECT data from ten preform specimens with varying materials and stackups were investigated in this thesis. Each preform measures approximately 400 mm × 400 mm, with thicknesses dependent on the layer material and stackup. Figure 5.1 shows three of these preforms. Table 5.1 lists the material type, stackup sequence, and reference number for each of the ten preforms. Figure 5.2 shows close-up photos from all five materials with their corresponding preform reference numbers.

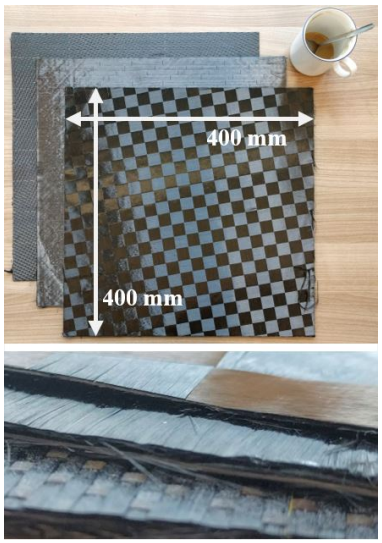

Fig. 5.1: Three of the ten investigated preforms.

Ref.	Stackup (top–bottom)	Material	Type
7.1	45/-45/0/90	Toho Tenax®	*UD
7.2	45/-45/90/0	Hexcel HexForce®	G1157 UD
7.3	0/90/45/-45	Toho Tenax®	†Biax UD
7.4	[45/-45]/[0/90]	Hexcel HexForce®	G0926 Biax
8.1	0/45/90/-45/-45/90/45/0	Toho Tenax®	UD
8.2	0/0/45/45/90/90/-45/-45	Toho Tenax®	UD
8.3	0/90/10/-80/20/-70/30/-60	Toho Tenax®	Biax UD
8.4	[0/90]/[10/-80]/[20/-70]/[30/-60]	Hexcel HexForce®	G0926 Biax
8.5	[10/-80]/[20/-70]/[30/-60]/[40/-50]	TexTreme® Thin-Ply	Biax
8.6‡	0/10/20/30/40/50/60/70/80	Toho Tenax®	UD

Table 5.1: Preform specimen properties. *Unidirectional, non-woven fibers. Without UD, woven fibers are implied. †Biaxial fabric, where two fiber directions (UD or woven) are present in a single sheet. Two orientations in immediate brackets (e.g., [0/90]) signify a woven fabric. ‡8.6 was constructed in the scope of this thesis work.

Toho UD 7.1, 8.1, 8.2, 8.6 | **Hexcel G1157 UD** 7.2 | **Toho Biax** 7.3, 8.3 | **Hexcel G0926 Biax** 7.4, 8.4 | **TexT. Thin-Ply Biax** 8.5

Fig. 5.2: Close-up photos of the preform specimen material with corresponding reference numbers. Each photo shows a 50 mm × 50 mm area, and are therefore (comparably) to-scale.

The construction of each preform followed these general steps:

1. Automatic cutting of individual layers with EVO's CNC-cutter.
2. Manual stacking of the layers.
3. Consolidation – i.e., the compaction and activation of the binder in an oven with vacuum bagging – of the stacked layers to produce a process-resemblant preform.

ECT scanning equipment

The commercially available EddyCus® Integration Kit[2] by Fraunhofer IKTS was used for the hard- and software sensor elements of the ECT. Each preform was scanned with a half-transmission[3] eddy current sensor guided by the 6-axis robotic arm in EVO (shown in Fig. 2.7). Table 5.2 lists the ECT scanning parameters. Figure 5.3 shows the sensor. The sensor was mounted to a spring-dampened linear rail to encourage consistent pressure along the preform.

[2] Further information in [10, 18, 27].

[3] Staggered, non-coincident excitation and pickup coils on the same side of the preform. See Section 2.3 for the principles of ECT.

ECT sensor parameters		Excitation frequencies	
Model	S13133; 2.4H	F1	1.895 MHz
Coil config.	Half-transmission	F2	2.753 MHz
Coil diameter	2.4 mm	F3	3.612 MHz
Coil shape	Helical	F4	*6.265 MHz

Table 5.2: ECT sensor parameters and excitation frequencies. *F4 for preform 7.3 was 1.582 MHz.

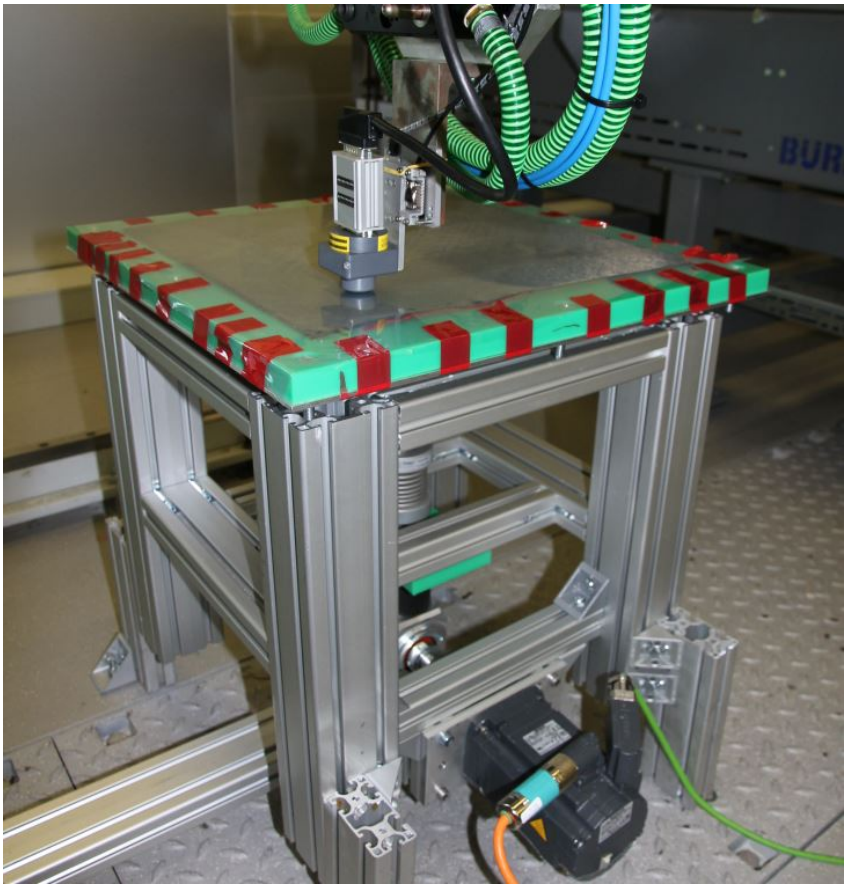

Fig. 5.3: Robot-guided eddy current sensor and turntable during scanning [27].

Each preform was placed on a programmable turntable (see Fig. 5.3) and covered by transparent vacuum film to protect both the preform and sensor surfaces. Capable of 360° rotation with an absolute position uncertainty[4] of 0.006° [28], this turntable was used to turn the preform to specific orientations for the scanning procedure.

[4] Equal to the sample standard deviation.

Scanning procedure

The standard measurement procedure for each preform involved repeating a programmed scanning path five times at the starting table orientation, rotating the table (and preform) −15°, and repeating the scanning/rotating for a total of seven table orientation groups and 35 individual ECT scans. Table 5.3 lists the standard scanning order.

Group	Table orientation	Measurement number				
1	0°	1	2	3	4	5
2	−15°	6	7	8	9	10
3	−30°	11	12	13	14	15
4	−45°	16	17	18	19	20
5	−60°	21	22	23	24	25
6	−75°	26	27	28	29	30
7	−90°	31	32	33	34	35

Table 5.3: Standard ECT scanning order.

Figure 5.4 illustrates the programmed scanning path. The sensor scanned a 256 mm × 256 mm area in a snake pattern with a 0.5 mm separation between parallel paths. This area was centered to both the preform and rotational center of the turntable. That is to say, at all turntable orientations, the centers of the preform and scanning path were approximately coincident. The sensor held a constant velocity of 200 mm s^{-1} (except to accelerate and decelerate at turns) along the scanning path.

The sensor's pickup coil continuously measured the complex impedance signal over four excitation frequencies (see Table 5.2) as it was guided along the path. The relative position of the sensor was simultaneously recorded and paired with the impedance values. This impedance–position data is what this thesis uses to produce ECT images and subsequent 2D-FFTs.

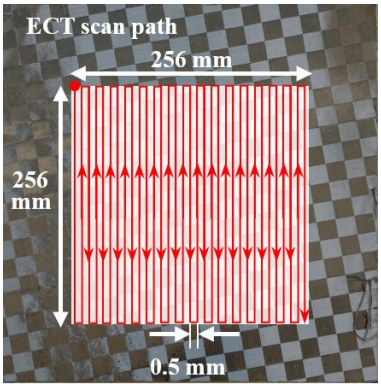

Fig. 5.4: Illustrative depiction of the ECT scanning path and area. Path separation not to scale.

Creating the ECT images

By mapping the measured impedance to its relative position along the 2D scanning path, an ECT image can be created. Specifically to this thesis, the real (Re) component of the impedance value is mapped to its position in the 256 mm × 256 mm scan area as a pixel, with its relative intensity displayed along the grayscale.[5] Figure 5.5 shows an *impedance cloud* from where the pixel intensity values are taken.

[5] In grayscale, the highest value is displayed as white, and the lowest value is displayed as black.

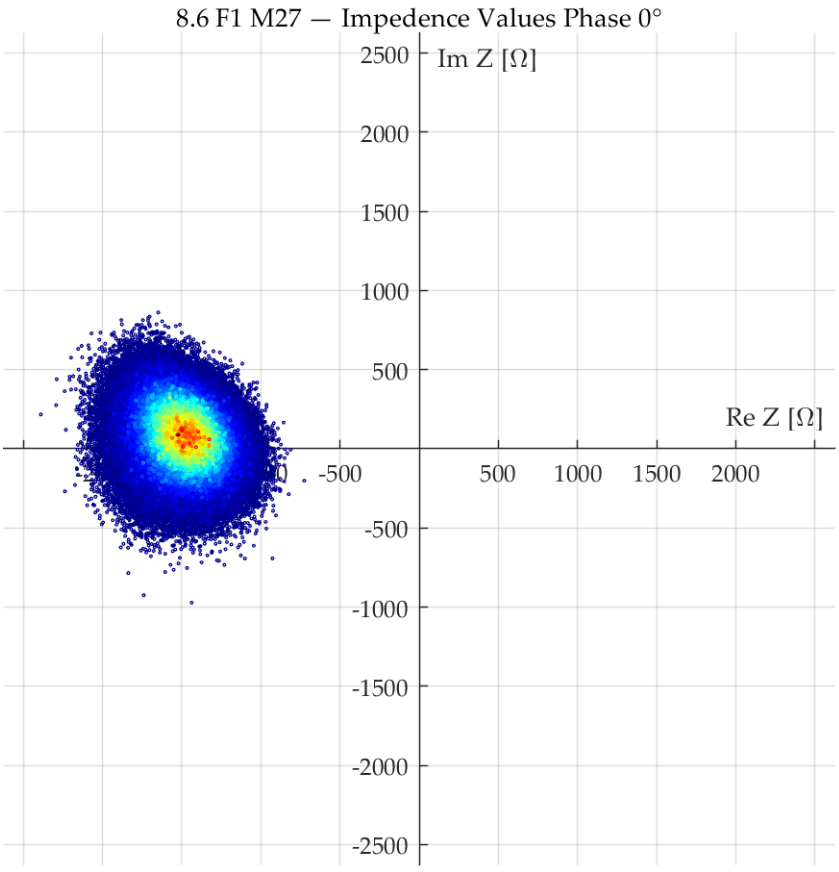

Fig. 5.5: Impedance cloud from an ECT scan. Colors represent clustering/density of individual impedance values.

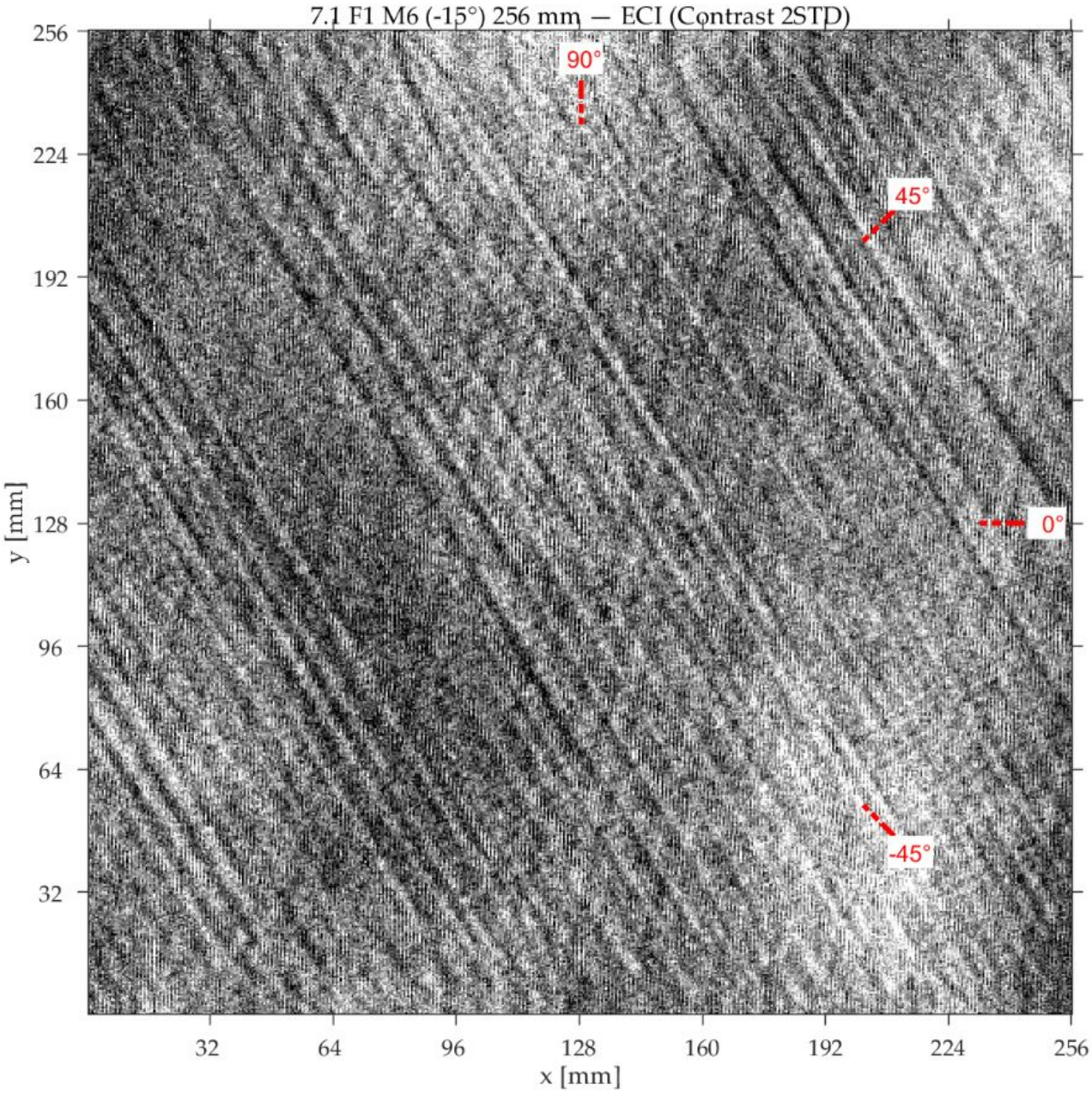

Fig. 5.6: A 512 px × 512 px, 256 mm × 256 mm eddy current image from specimen 7.1 (Toho UD; stackup [45/-45/0/90]) at measurement M6 (table orientation −15°). Lighter pixels represent higher Re values from the impedance cloud, while darker pixels represent lower Re values.

With the 256 mm × 256 mm scan area and path separation of 0.5 mm, the default ECT image resolution from the existing ECT data is 512 px × 512 px. Figure 5.6 is a full-area ECT image from preform specimen 7.1 for the first excitation frequency (F1) with light contrast applied. Figure 5.7 shows ECT image examples from the other preforms (7.2–8.6), also for F1 and applied with light contrast. The notable vertical striping in Fig. 5.6 is an artifact of the ECT scanning direction [27], and is a common occurrence in the data examined in this thesis.

For the remainder of this thesis, individual ECT scans are referred to by their specimen number (#.#), sensor frequency (F#), and measurement number (M#). For example, the sixth ECT scan of specimen 8.5 in the second sensor frequency is "8.5 F2 M6."

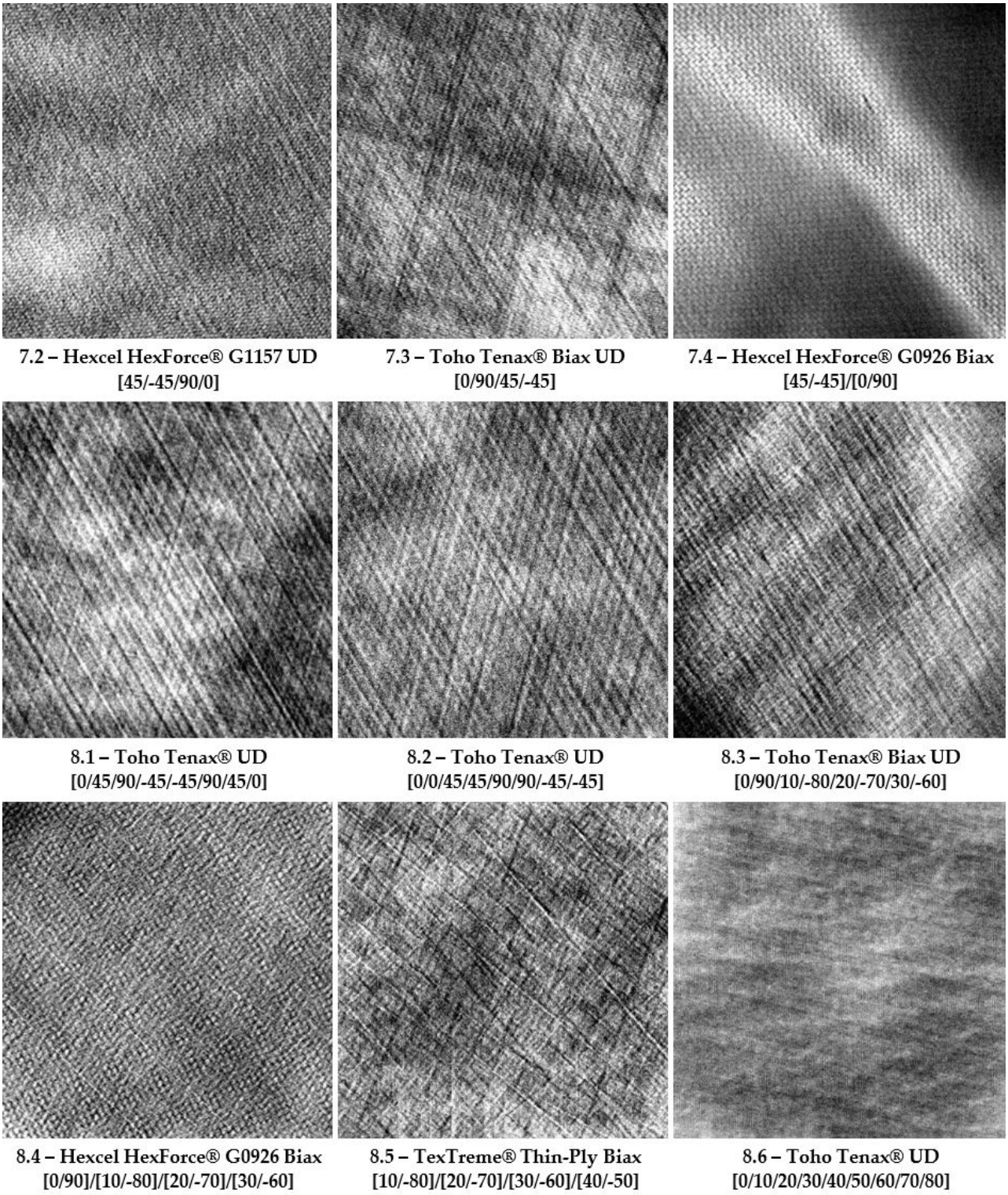

Fig. 5.7: Eddy current images from specimens 7.2–8.6 at various measurements and table orientations.

5.2 Development of a 2D-FFT angle extraction algorithm

With the ECT data and the basis for the corresponding images reviewed, a system of algorithms to detect the layer angles with 2D-FFT on ECT images can now be established. This section presents the methodology and validation behind this system. To transfer smoothly into these details, a review of 2D-FFT on ECT images is first given:

Figure 5.8 shows the 2D-FFT of the ECT image in Fig. 5.6 generated with MathWorks® MATLAB.[6] Because the input signal is a discrete 512 px × 512 px image, the output 2D-FFT is likewise a discrete 512 × 512 matrix. A grayscale image which represents the 2D-FFT matrix – typically in the logarithmic scale[7] – reveals the orientations and frequencies of the image's periodic signals; for ECT images, these periodic signals are (generally) the fiber patterns, which means the bright areas signifying these pattern orientations in the 2D-FFT are perpendicular to the actual fiber directions seen in the ECT.

[6] MATLAB was used to generate all 2D-FFTs in the scope of this thesis.

[7] The 2D-FFTs shown in this thesis and in literature are predominantly shown in logarithmic scale to compensate for the large differential in grayscale pixel intensities. The algorithms and analyses described in this thesis all use "pure" 2D-FFTs for the evaluation of data.

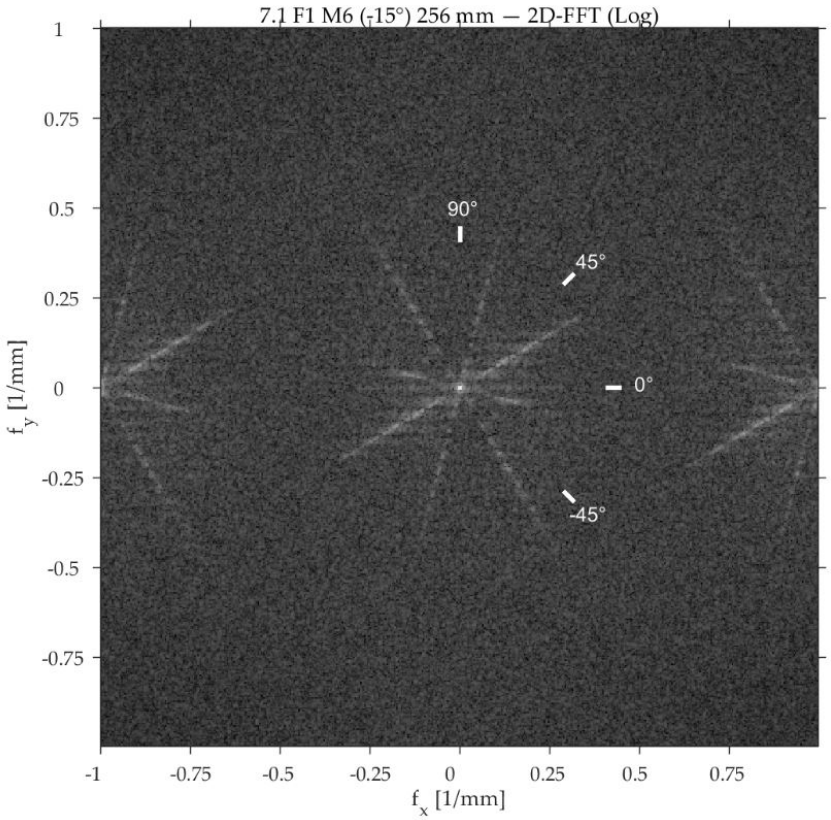

Fig. 5.8: Full 2D-FFT of the ECT image from preform 7.1 shown in Fig. 5.6. Grayscale intensity values in logarithmic scale.

Summing cuts in the 2D-FFT

The brighter areas in the 2D-FFT allow us to visually estimate the detected fiber directions – but how can we numerically analyze the 2D-FFT to extract the exact angles? For this thesis, the proposed method is to extend *cuts* from the 2D-FFT center, with evenly spaced points along each cut which sample the neighboring discrete intensities. Figure 5.9 illustrates this approach. The cuts extend evenly from $-90°$ to $90°$.[8] The sampled intensities along each cut are summed, and the sums are plotted against the corresponding angular position of the cuts.

[8] The axis-symmetry of the 2D-FFT means only half the matrix must be analyzed.

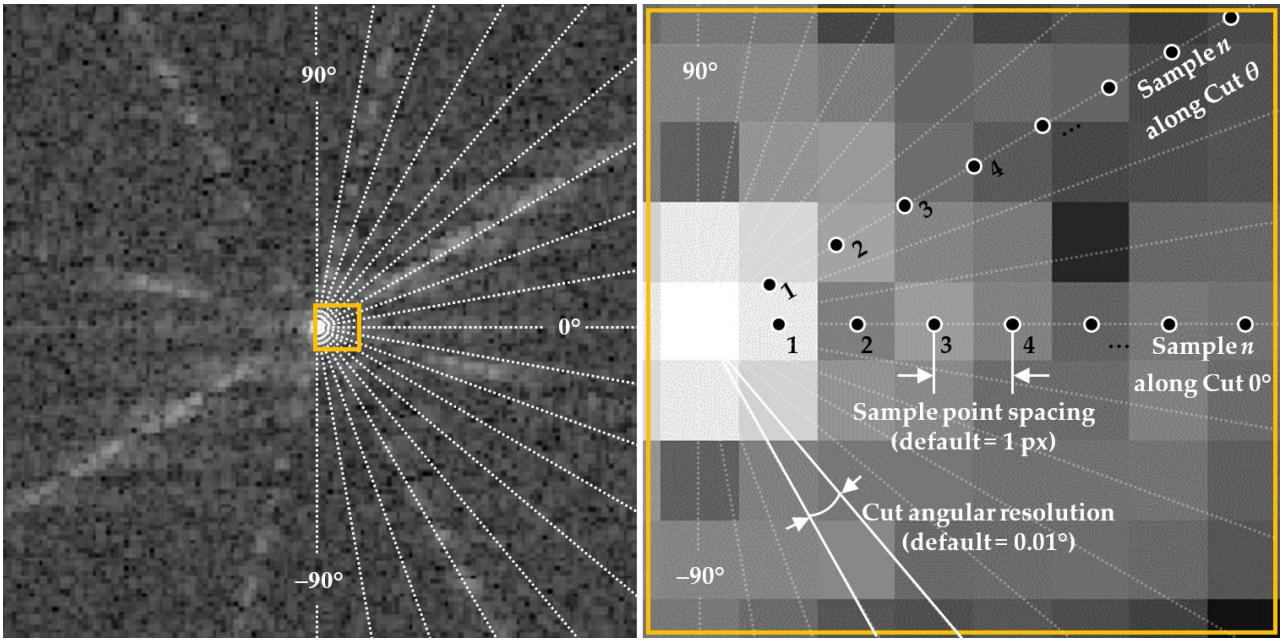

Fig. 5.9: Illustration of the SUMCUT method on the 2D-FFT from Fig. 5.8. The default cut angular resolution (0.01°) is not shown to scale. The default sample point spacing (1 px) is shown to scale.

The result – a SUMCUT plot – reveals the areas of higher 2D-FFT intensity as *peaks*. Figure 5.10 shows a spline SUMCUT plot from the 2D-FFT in Fig. 5.8. The angular resolution of the cuts is 0.01°. The sample point spacing is the default 1 px – i.e., a $1/256\ \mathrm{mm}^{-1}$ image frequency. Each cut in Fig. 5.8 is a summation of sample points between 3 px and 96 px away from the 2D-FFT center.[9] The angle corresponding to the highest point of each prominent peak is then taken as the angle of the fiber pattern, i.e., 90° to the fiber direction of the layer.

[9] The parameter optimization of the inner and outer sample point limits (IC and OC) is described in Chapter 6.

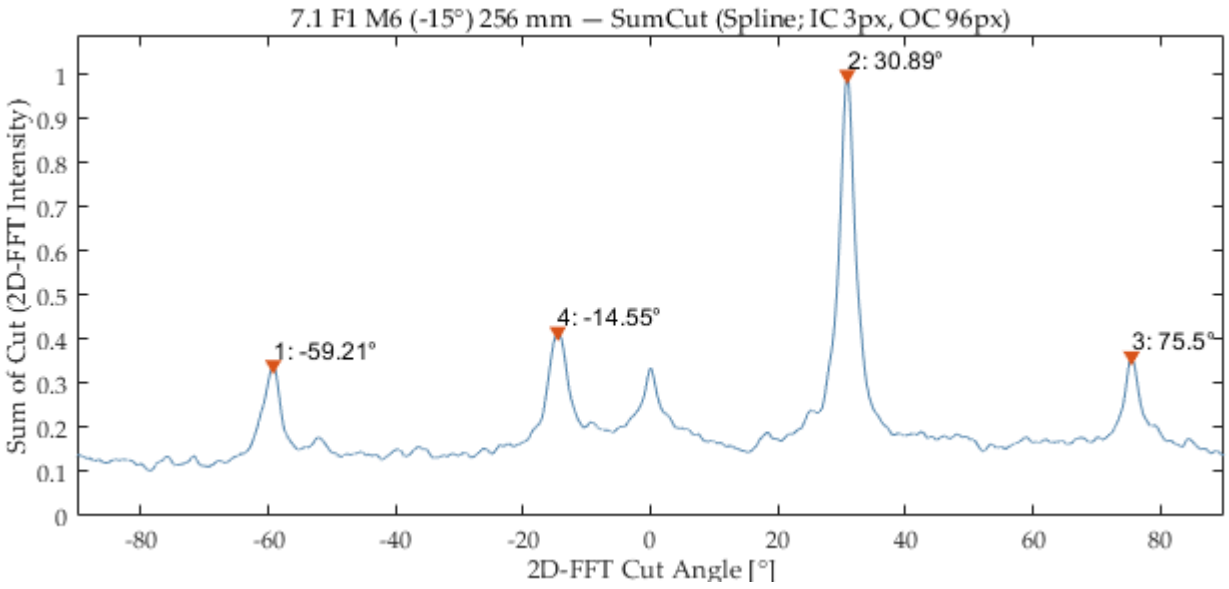

Fig. 5.10: Spline SUMCUT plot from the 2D-FFT in Fig. 5.8. Default SUMCUT settings used – i.e., angular res. = 0.01°, point spacing = 1 px. Numbers next to peaks indicate stack position of the layer.

Interpolation-based sampling of the 2D-FFT values

The fiber angle extraction method is based on the sampling of points along the discrete matrix of the 2D-FFT. Because these points are rarely coincident with the discrete coordinates of the 2D-FFT, an interpolation scheme is necessary. Two forms of 2D interpolation-based sampling are proposed: bilinear and bicubic spline.

Figure 5.11 illustrates these 2D sampling methods along with their 1D analogies. Figure 5.12 shows the interpolation of a discrete color map. The following is a review from [30, 31], and the author directs readers specifically to [30] for a comprehensive mathematical description:

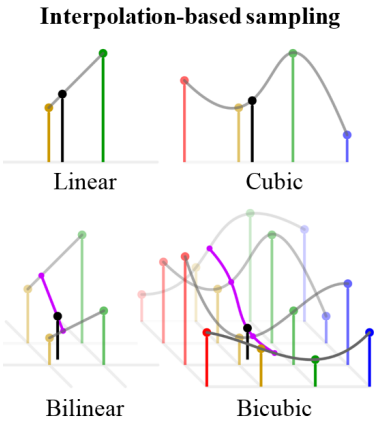

Fig. 5.11: Depiction of interpolation methods for sampling between discrete values in 1D and 2D [29].

1. **Bilinear interpolation**: Bilinear interpolation-based sampling uses a linearly weighted average from the four nearest grid values. Employing bilinear interpolation inherently means no interpolated value will exceed the range of true measured values – i.e., no overshooting occurs.

2. **Bicubic (spline) interpolation**: Bicubic interpolation uses a polynomial-based scheme which uses the surrounding 4×4 grid of discrete values. Sampling with this method can estimate local maxima and minima which are outside the discrete grid's range of values – i.e., overshooting can occur. The spline version of this method means the entire interpolated "surface" is continuously differentiable across gridlines. A notable application of cubic splines is in Euler–Bernoulli beam theory.

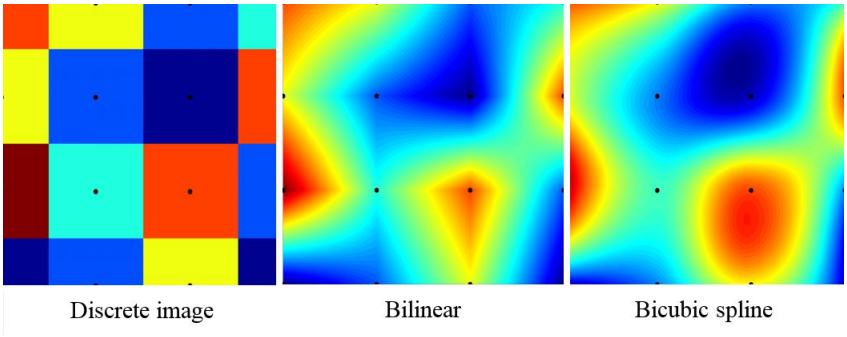

Fig. 5.12: The application of bilinear and bicubic spline interpolation on a discrete color map [30].

Validating the angle extraction algorithms with simple 2D-FFTs

The validation of the proposed 2D-FFT angle extraction method – referred to at DLR as *superX* (sX) – covers the SUMCUT principle and compares the bilinear and bicubic spline interpolation methods. To determine the accuracy of sX, the detected angles from pure sine-based 2D images, or *pseudo images*, with varying frequencies were evaluated for orientations from 0° to 90°.

Figure 5.13 shows a 22 px $\times$ 22 px pseudo image with 9 periods horizontally across the resolution. The sine signal mimics the fibers

from the ECT images, but because only one frequency ($9/22\ \mathrm{px}^{-1}$) and orientation (0°) are present, the resultant 2D-FFT shows only one distinct pair of pixel clusters. A pseudo image with infinite resolution would result in a pair of infinitely small pixels on the likewise infinite resolution 2D-FFT.

Because this ECT/2D-FFT system operates with discrete signals, the point signifying the frequency and orientation instead spans multiple pixels, most notably for points which lie at non-integer distances from the 2D-FFT center. In Fig. 5.13, the $9/22\ \mathrm{px}^{-1}$ signal is revealed by a single distinctly higher pixel value within the cluster of pixels on the 2D-FFT. The distance from the 2D-FFT center to the brightest pixel is exactly 9 px, which describes the input frequency.

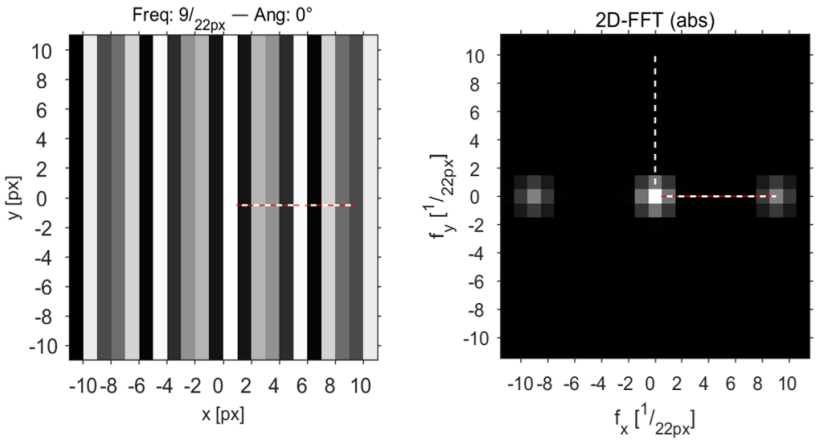

Fig. 5.13: Pseudo image ($9/22\ \mathrm{px}^{-1}$; 0°) and resultant 2D-FFT in absolute (i.e., non-logarithmic) scale.

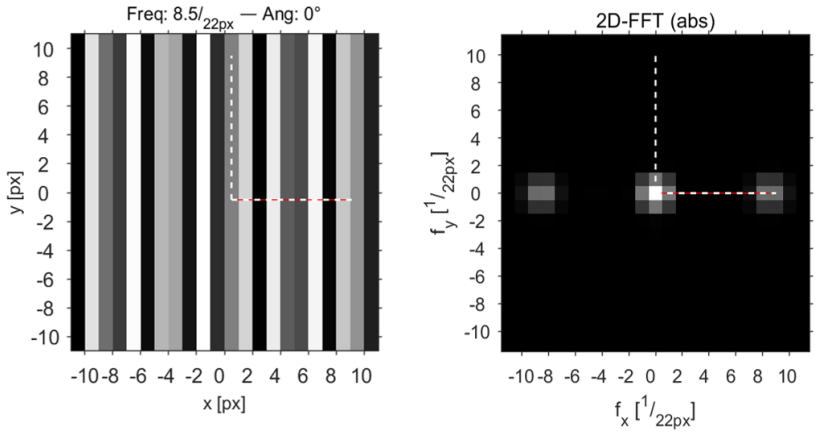

Fig. 5.14: Pseudo image ($8.5/22\ \mathrm{px}^{-1}$; 0°) and resultant 2D-FFT.

Figure 5.14 shows an $8.5/22\ \mathrm{px}^{-1}$ 0° pseudo image and corresponding 2D-FFT. When the periodic signal frequency is exactly halfway between integers and is oriented horizontally (or vertically), the resultant 2D-FFT pixel cluster describing the signal frequency is evenly distributed in intensity – i.e., there is no distinct maximum. We know that the true point rests exactly between the pixels, but the 2D-FFT only shows us a discrete sampling.

Figure 5.15 shows a 22 px × 22 px pseudo image with a $8.5/22\ \mathrm{px}^{-1}$ frequency at an 18.65° orientation. The true 2D-FFT point is 8.5 px from the center at an angle of 18.65° with the horizontal axis; in the shown discrete 2D-FFT, a cluster of unevenly distributed pixel

intensities is instead visible, and the true point is "lost" between the points. Figure 5.16 shows a 3D representation of the 2D-FFT image, where the third axis is the pixel intensity.

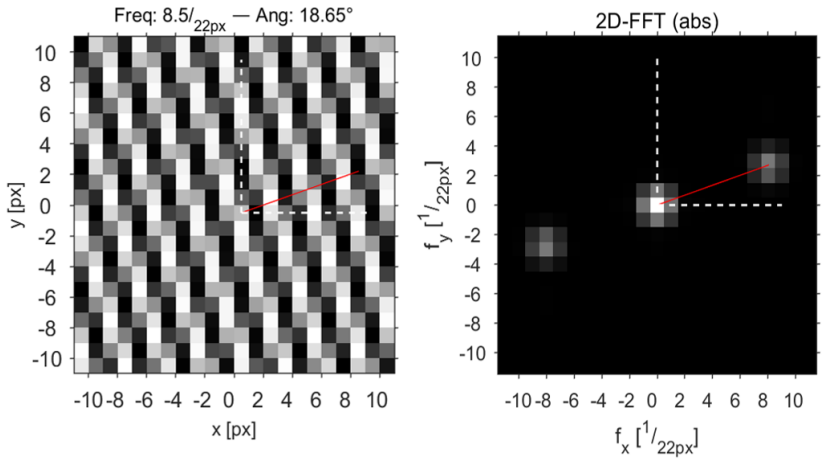

Fig. 5.15: Pseudo image (8.5/22 px^{-1}; 18.65°) and resultant 2D-FFT, a 3D representation of which is shown in 5.16.

The linear panel-like surface in Fig. 5.16 reveals the expectations for bilinear interpolation on the pixel cluster: linear increase and decrease with no over- (or under-) shoot. With spline interpolation, the overshooting surface (right peak in Fig. 5.16) reveals the true maximum location. The angle from this maximum to the center is 19.05°, translating to a detected–input difference of 19.05°–18.65°=0.40°. That is to say, the difference between the input signal orientation and the spline-maxima-based detected angle is 0.40°.

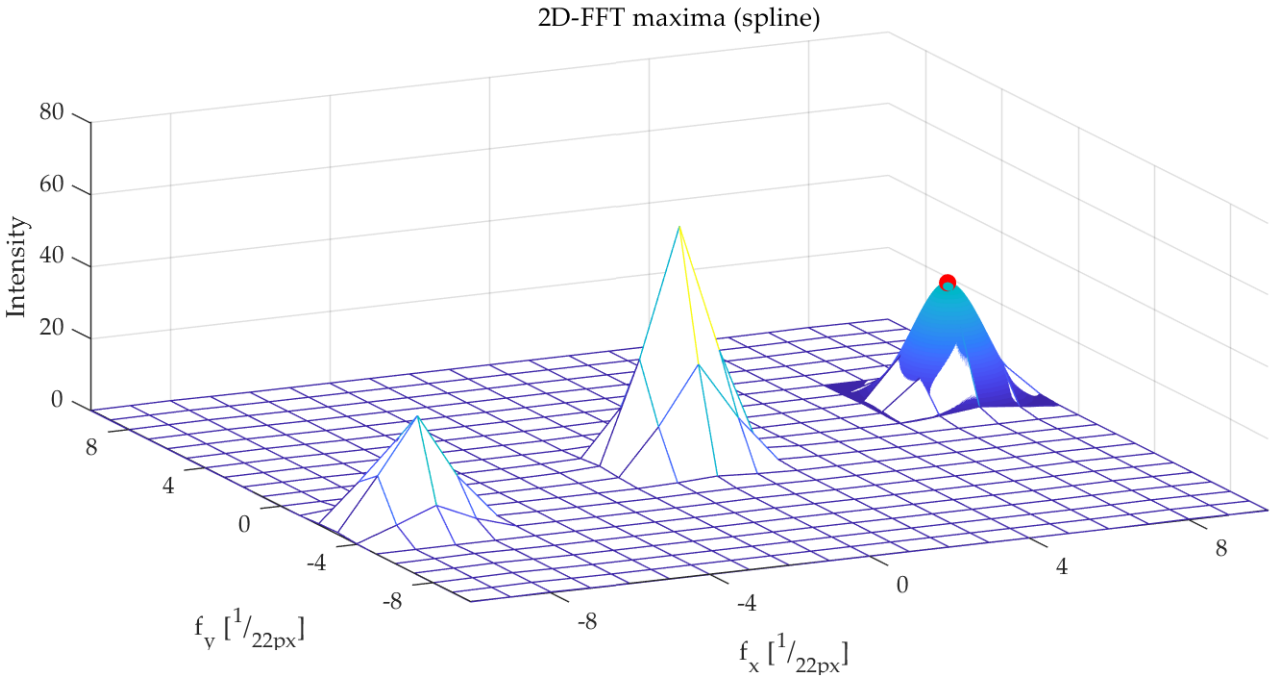

Fig. 5.16: 3D representation of 2D-FFT values with (8.5/22 px^{-1}; 18.65°).

Figure 5.17 shows the SUMCUT from Fig. 5.15 using the bilinear and spline methods. The zoomed plot in Fig. 5.18 shows the difference in peaks (and therefore detected angles) between the two SUMCUT-interpolation schemes, as well as the difference in the spline-maxima detected angle and original input angle.

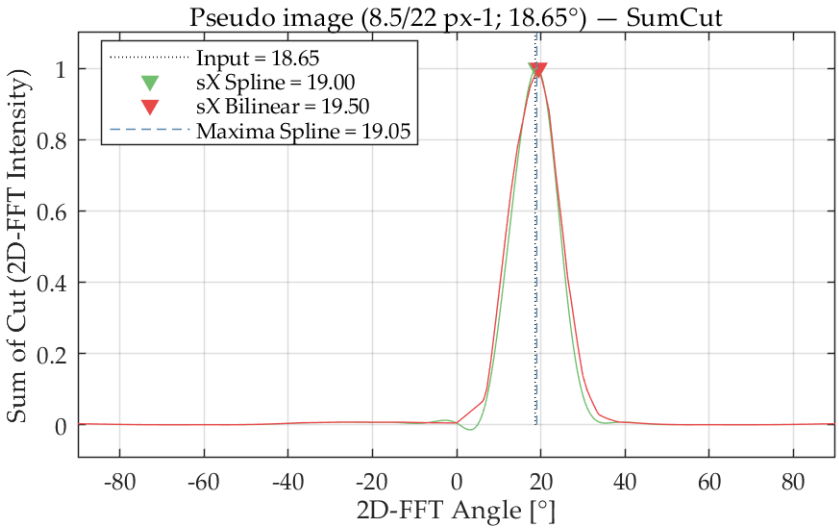

Fig. 5.17: SUMCUT from pseudo image (8.5/22 px^{-1}; 18.65°).

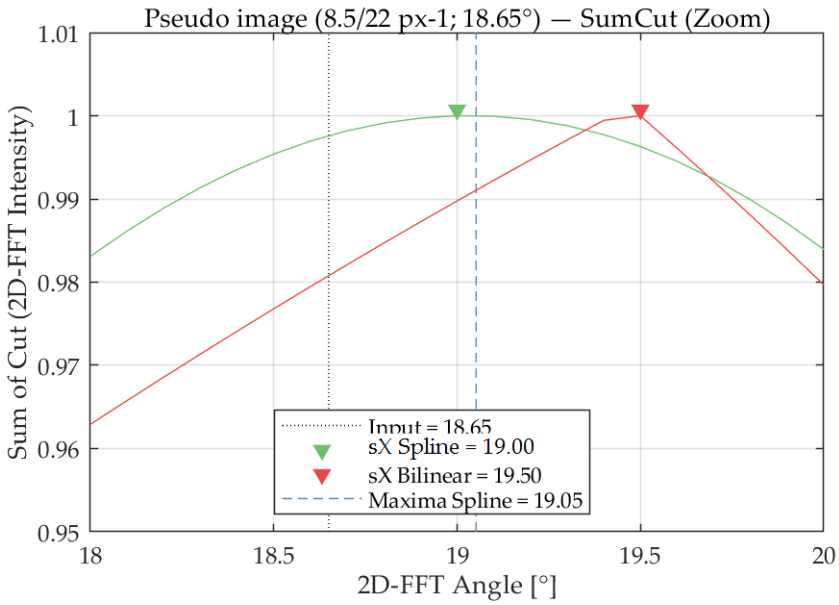

Fig. 5.18: Zoomed portion of SUMCUT in 5.17 showing peak quality between bilinear and bicubic spline sampling methods.

To review our progress in this section so far:

- A system has been proposed – sX– to numerically analyze 2D-FFTs by summing evenly spread cuts consisting of sampling points.
- These summed cuts are plotted in a SUMCUT graph, and the peaks along this plot are taken as the fiber directions.
- Two sampling methods have been proposed: bilinear and spline.
- Combining sX with pseudo images allows us to measure how

accurate the SUMCUT principle is at various 2D-FFT point angles and distances.

- An additional "spline-maxima" method to determine the supposed true 2D-FFT angle from pseudo images is proposed.
- Spline-maxima provides an independent comparison with the two interpolation schemes for SUMCUT.

If we generate a set of 8.5/22 px^{-1} pseudo images with orientations ranging from 0° to 90°, we can then see how accurate the various 2D-FFT methods are at detecting the true input angle when the 2D-FFT point rotates about the center across the pixel field. Figure 5.19 is a plot of the detected–input results for the 8.5/22 px^{-1} pseudo image with a 0°–90° sweep with 0.01° increments.

In other words, we use pseudo images to generate 2D-FFTS with a single point 8.5 px from the center at an angle of 0.00°, 0.01°, 0.02°, ..., 89.99°, 90.00°. For each 2D-FFT point angle, we apply the two SUMCUT interpolation schemes and the spline-maxima method to calculate the point angle. By subtracting the detected angles by the input, we then produce three differences – one for each 2D-FFT analysis method – for a given input. In Fig. 5.19, the input angle is the horizontal axis, and the detected–input difference is the vertical axis.

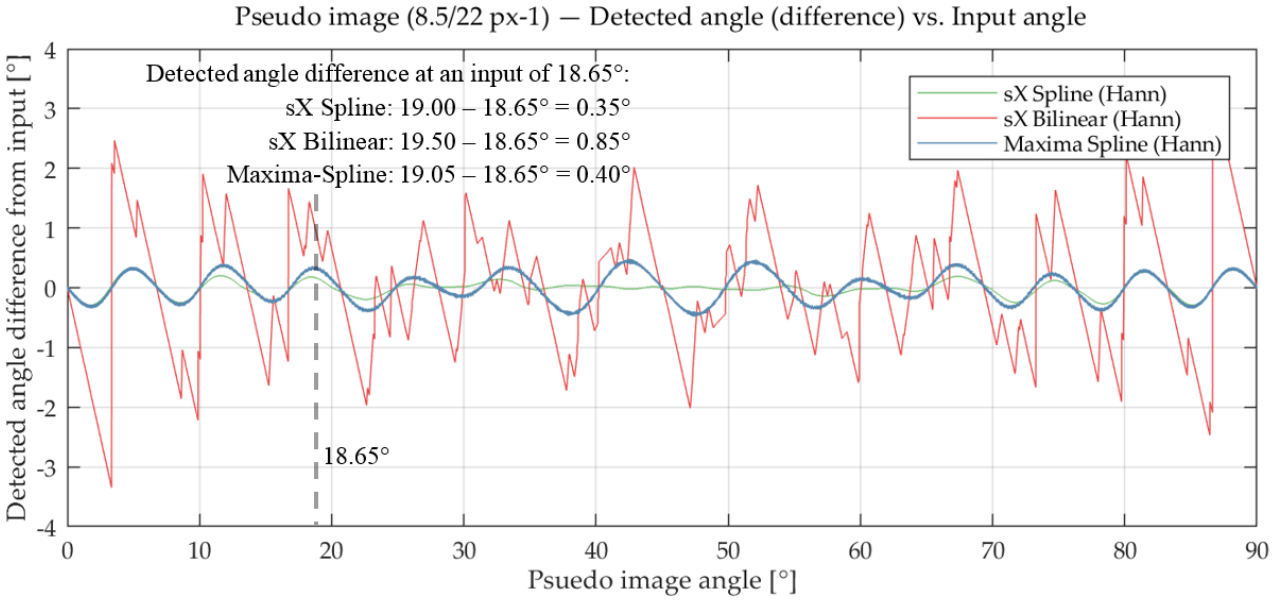

Fig. 5.19: Detected angle difference versus input angle of pseudo image with 2D-FFT point at 8.5 px.

The curves in Fig. 5.19 show significant properties: First, the difference between the bilinear method and both spline-based systems is considerable. The maximum angle difference with bilinear SUMCUT is nearly 3.5°, but the angles detected with SUMCUT spline and spline-maxima do not deviate above 0.5°. The SUMCUT spline method in particular shows minimal deviation near 45°.

In terms of stability, the spline detection results are quite smooth, while the bilinear results are jittery and erratic. The cause of this seemingly unpredictable variation comes from individual cuts passing over the plate-like interpolation field, as seen in Fig. 5.16.

What happens if the pseudo image frequency is increased and the 2D-FFT pixel point is moved away from the center? Figure 5.20 shows the 0°–90° sweep plots from an 2D-FFT point 20.8 px and 46 px away from the center. Note that the vertical axis decreases in scale.

By comparing Fig. 5.19 and 5.20, we can see that two phenomena occur when the 2D-FFT point moves away: 1) the detected–input difference of all three angle detection methods decreases, and 2) the number of oscillations in each curve increases. The detected angles deviate less (i.e., the methods are more accurate at predicting the input angle) because the angular "spread" of each pixel cluster lessens with distance. The results oscillate more because the pixel cluster passes through more pixels when rotated.

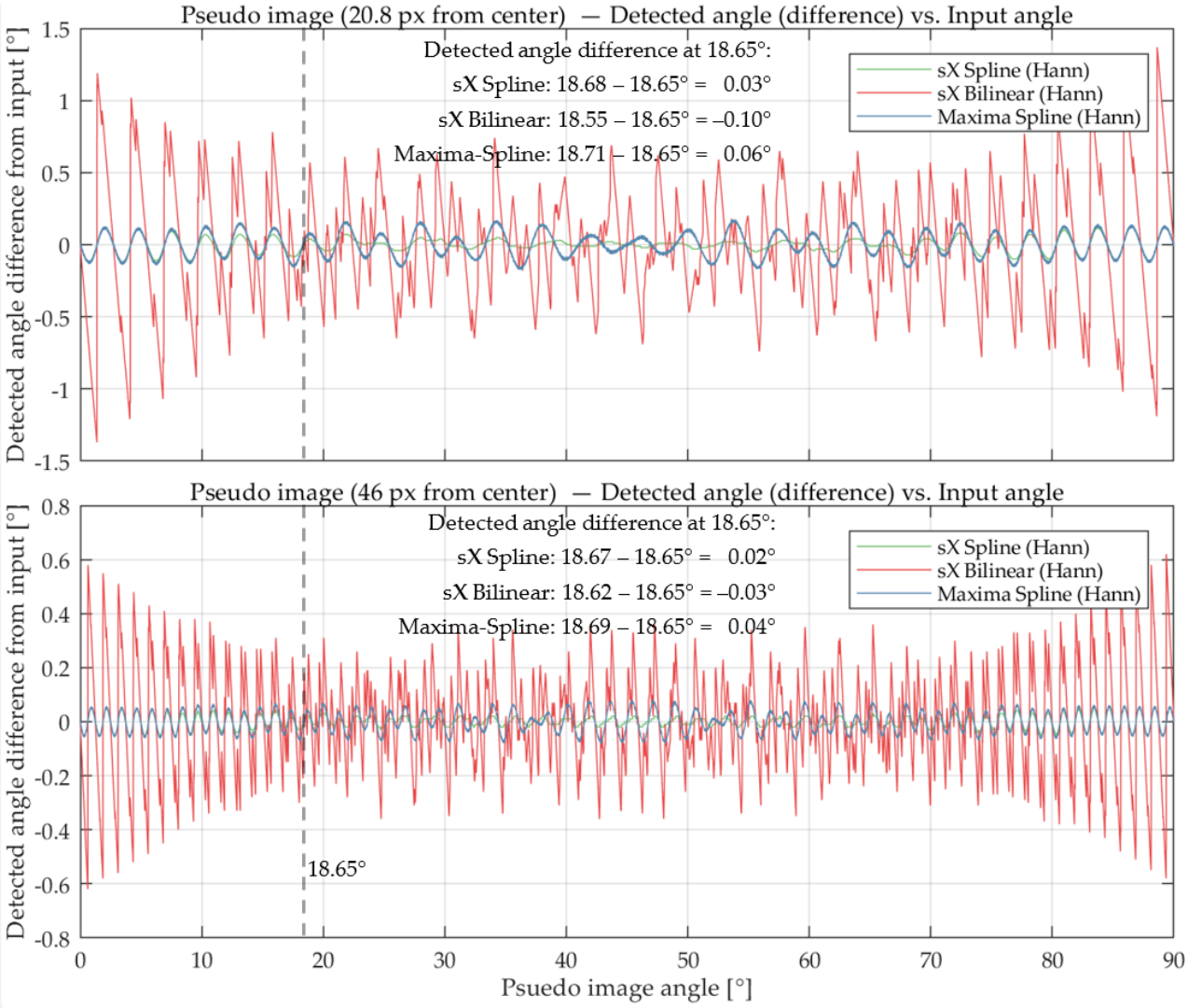

Fig. 5.20: Detected angle difference versus input angle of pseudo images with 2D-FFT points at 20.8 px and 46 px.

These curves visually show us that the uncertainty in a detected angle depends on the method and 2D-FFT pixel distance – but how can we compare the uncertainty of methods and pixel distances in a quantifiable manner? The answer is found in standard deviation.

By calculating the standard deviation of the difference in detected angle and input angle across a 0°–90° point sweep in the 2D-FFT, we

are then able to describe the uncertainty for a specific combination of detection method and pixel distance. In reference to Fig. 5.19 and 5.20, the uncertainty of a method–pixel combination is the sample standard deviation of its corresponding curve.

Figures 5.21 and 5.22 plot the uncertainty in the detected angle deviation at various pixel distances for the SUMCUT (i.e., sX) and spline-maxima methods. The second plot is a zoomed portion of the first plot for pixel distances from 20 px to 21 px. Figure 5.23 provides context to the pixel distances in a zoomed 2D-FFT from an ECT image of preform 7.1.

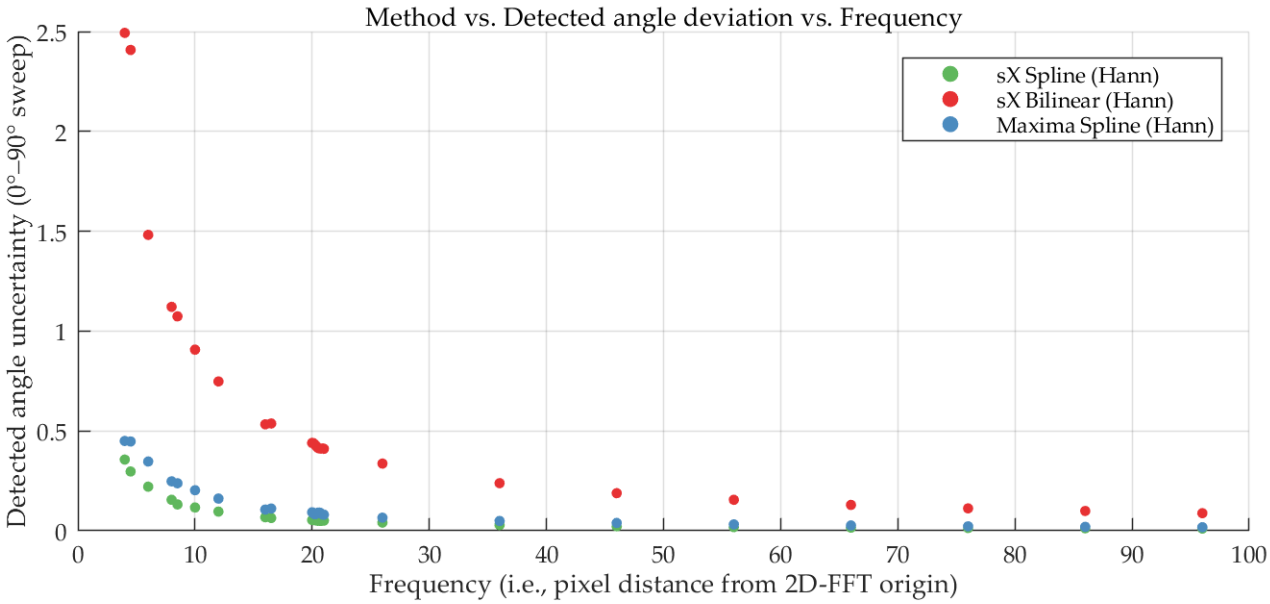

Fig. 5.21: Uncertainty of the detected angle deviation for various 2D-FFT pixel distances. See Fig. 5.23 for pixel distances on an ECT 2D-FFT.

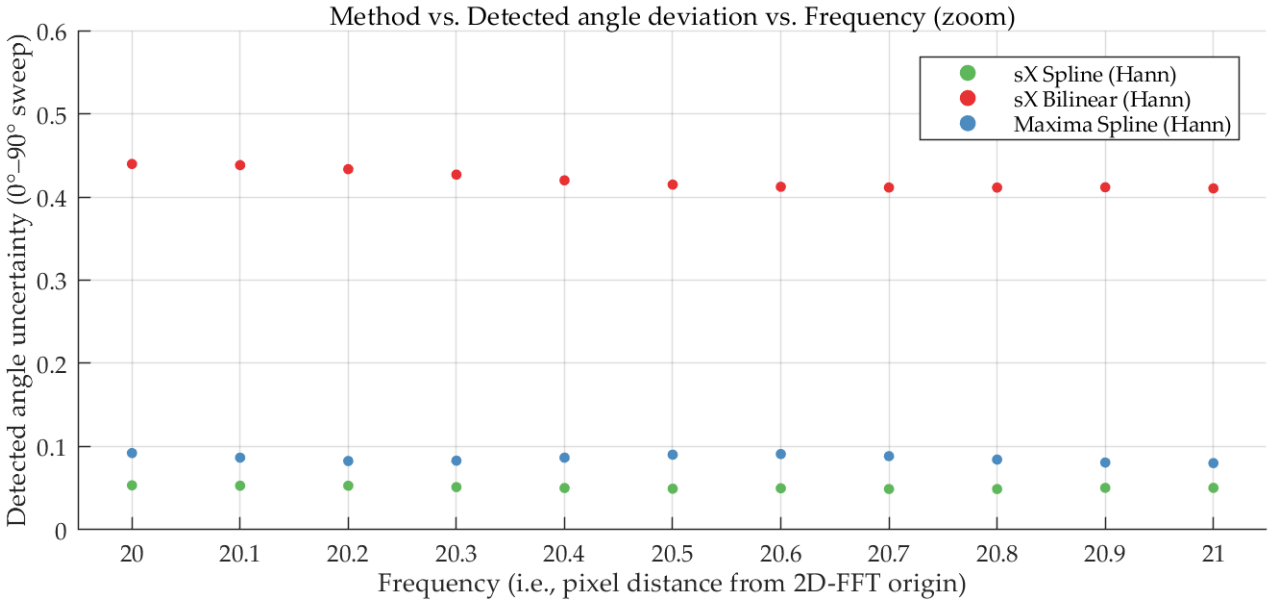

Fig. 5.22: Zoomed portion of detected angle uncertainty from Fig. 5.21.

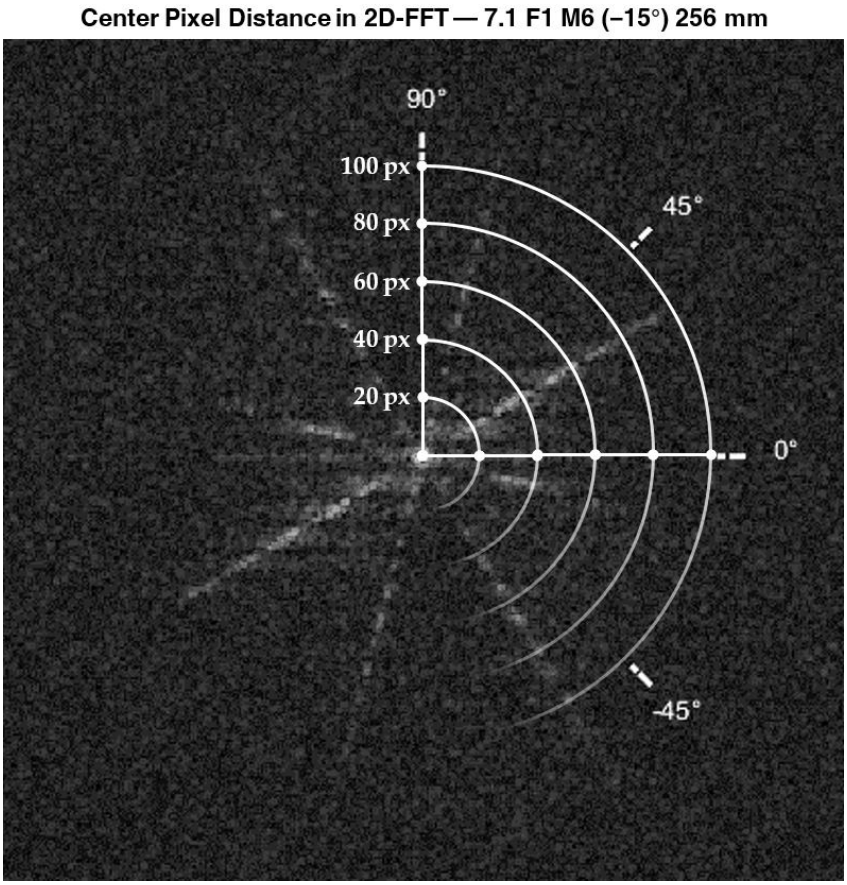

Fig. 5.23: Pixel distance from the 2D-FFT center with reference to the 2D-FFT of a standard resolution ECT (from the 2D-FFT in Fig. 5.8).

The plots in Fig. 5.21 and 5.22 confirm that as the frequency increases, the uncertainty in the detected angle deviation decreases. Qualitatively speaking, as the pixel cluster moves further from the 2D-FFT center, the "trustworthiness" of the subsequent detected angle increases. For some pixel distances between integers, the detected angle uncertainty is actually slightly higher than the integer before it. This may be an effect from 2D-FFT noise introduced by spectral leakage [32].

Because theoretical 2D-FFTs are continuous, interpolating the discrete 2D-FFTs from the ECT images with bicubic spline in SUMCUT would appear to provide the most stable means of angle detection. Indeed, the preceding validation shows that bicubic spline – at least on simple 2D-FFTs – has significantly less uncertainty in the detection of angles. The advantage of bilinear is the significantly reduced computation load, and therefore a shorter processing time. Nevertheless, the analyses in the following sections do investigate both interpolation methods for sampling in SUMCUT.

In conclusion, the plots in Fig. 5.21 and 5.22 show that by analyzing a 2D-FFT through the SUMCUT principle, an inherent uncertainty is thus introduced to the detected angle(s). Because this effect cannot be compensated, we now expect that the angles detected from ECT images with the sX system will exhibit a discernible systematic error within the uncertainty range seen in this validation.

Windowing the eddy current images

The application of 2D window functions to ECT images is a key step in the sX system to improve 2D-FFT quality after ECT image creation. Figure 5.24 shows the appearance of the four window functions investigated with the psuedo images. Figure 5.25 shows the effect of a Hann window on an 2D-FFT from preform 7.1.

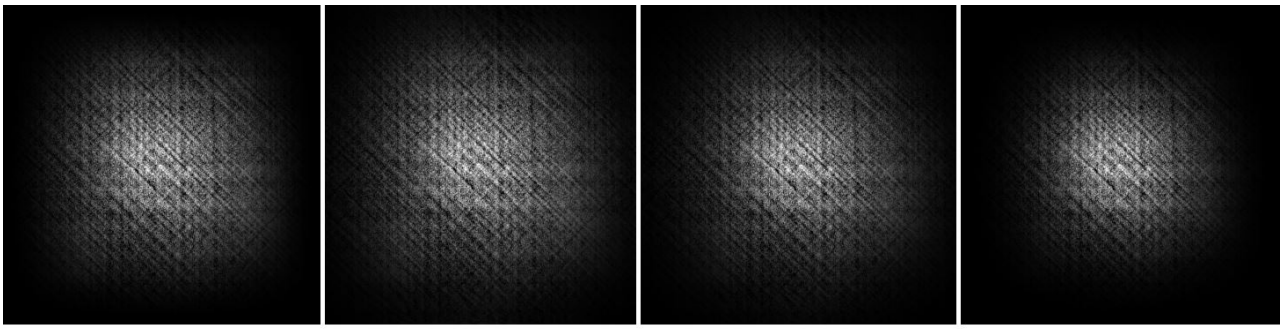

Fig. 5.24: Four investigated 2D window functions.

In general, the purpose of windowing 2D signals is to reduce spectral leakage, which is caused by discontinuities in non-integer periods in a signal. For the visual case of ECT, a window reduces the overall noise in the subsequent 2D-FFT. See [32] for details on windowing.

The validation results between interpolation methods in the previous section were all generated with the Hann window because of its satisfactory implementation in previous algorithms by Hienz and Buelow [27], as well as its general acceptance in literature as a satisfactory "all-purpose" window [32]. However, because this thesis proposes a new ECT/2D-FFT evaluation system, analyses of different windows were still made.

Figure 5.26 shows the detection–input uncertainty results (similar to Fig. 5.22) of the bicubic spline SUMCUT method using four different windows at 11 different pseudo image frequencies (i.e., pixel distances). The most notable difference is the significant decrease in detection uncertainty from non-windowed signals to windowed signals, thus verifying windowing from a general perspective.

Between the results of specific windows, Blackman appears to produce the greatest improvement in uncertainty. Hann – the generally favored window – is a close second. While this verification seems to support windowing with the Blackman function for future analyses, an additional parameter analysis on real ECT images is made later in this chapter.

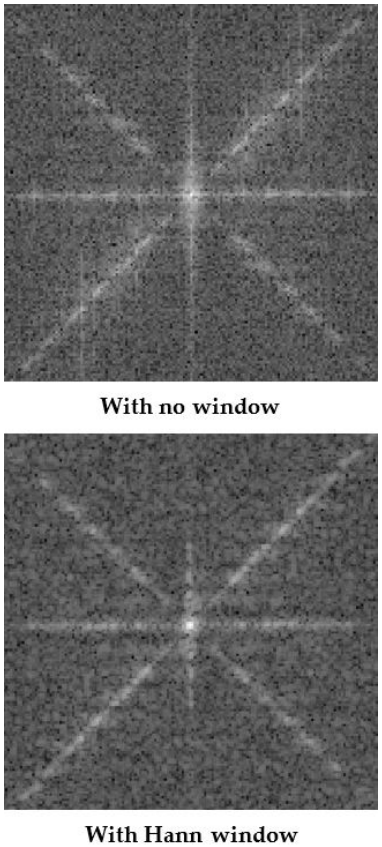

Fig. 5.25: 2D-FFT of a non-windowed and Hann-windowed ECT image from preform 7.1.

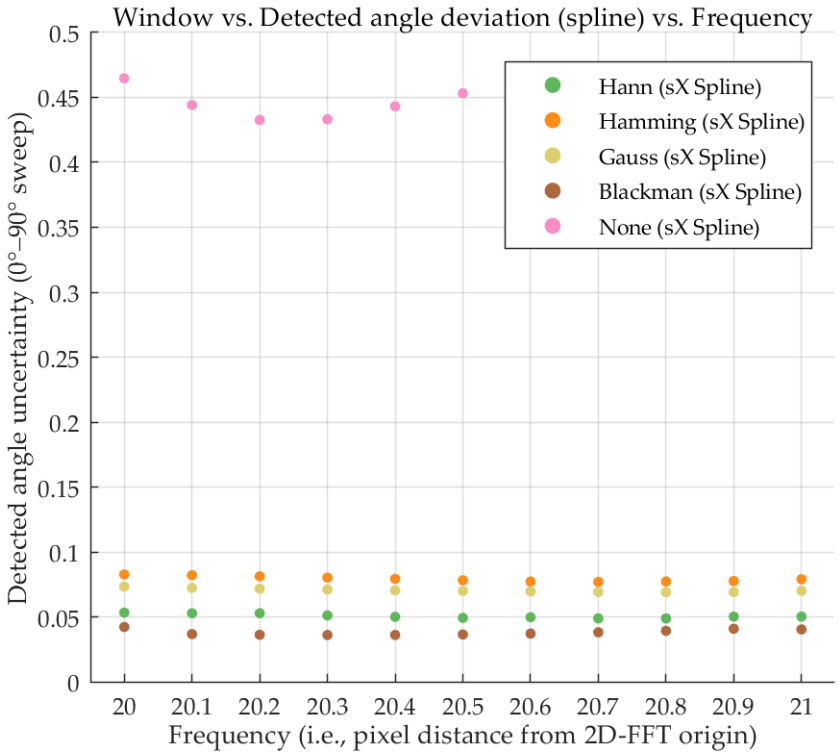

Fig. 5.26: Effect of windowing on the uncertainty of detected angles from pseudo images with the SUMCUT/sX spline method. Note that non-windowed results are as inaccurate as those from the (windowed) sX bilinear method shown in Fig. 5.22. Gauss window parameter $\alpha = 2.5$.

5.3 Calculating uncertainty from the results

In the previous section, we were able to compare 2D-FFT angle extraction methods with known input values (i.e., the pseudo image angles), and from this input–output comparison a measure of uncertainty was determined. However, as we now enter the realm of measured ECT data, there will be no direct input value with which we can compare the detected angles.

Instead, multiple measurements at both identical and rotated orientations must be compared. With these two facets of existing data, two separate measures of uncertainty can be defined, thus providing us with a metric for the optimization and final accuracy of the ECT/2D-FFT layer angle detection method in this thesis.

Average group uncertainty

As we move forward into the application of real ECT data for parameter optimization, we will employ the *overall average group uncertainty* $\bar{\sigma}_{\text{group}}$. In general, $\bar{\sigma}_{\text{group}}$ provides us with a metric for the random error between repeated measurements. To describe the derivation of $\bar{\sigma}_{\text{group}}$ from the detected angles, an example is given:

Let us assume an arbitrary preform with a [0/90/45/-45] stackup has been scanned 35 times across 7 table orientations according to the measurement procedure in Table 5.3 from Section 5.1. Table 5.4 lists the hypothetical detected fiber angles for layer 3. To determine $\bar{\sigma}_{\text{group}}$ for this preform, the first step is to calculate the uncertainty of each group i in each layer j, where the uncertainty $\sigma_{\text{group}}^{(j,i)}$ is the sample standard deviation of the group's five detected angles.

Group i	Table orientation	Layer 3 ($j = 3$) detected angle					$\sigma_{\text{group}}^{(3,i)}$
1	0°	45.5°	45.5°	45.5°	45.6°	45.6°	0.05°
2	−15°	30.1°	30.0°	30.0°	30.1°	30.1°	0.05°
3	−30°	15.3°	15.6°	15.5°	15.6°	15.2°	0.18°
⋮	⋮	⋮	⋮	⋮	⋮	⋮	⋮
							Layer 3 average group uncertainty $\bar{\sigma}_{\text{group}}^{(3)} =$ 0.10°

Table 5.4: Example data to illustrate the derivation of a preform's overall average group uncertainty. This data follows the standard scanning order shown in Table 5.3.

Next, the average group uncertainty for each layer j is calculated, where the uncertainty $\bar{\sigma}_{\text{group}}^{(j)}$ is the arithmetic mean of that layer's 7 group uncertainties. Finally, the overall average group uncertainty $\bar{\sigma}_{\text{group}}$ of the preform data is the arithmetic mean of these average group uncertainties. If the average group uncertainties of the hypothetical layers 1, 2, 3, and 4 were 0.06°, 0.08°, 0.10°, and 0.12°, then $\bar{\sigma}_{\text{group}} = 0.09°$.

The resultant value of $\bar{\sigma}_{\text{group}}$ represents the average random error for the detected layer angles of a preform. That is to say, $\bar{\sigma}_{\text{group}}$ tells us how reliable the angle detection is when a preform is scanned multiple times in a specific orientation. Additionally, each layer's average group uncertainty describes this repeated-orientation uncertainty at that layer depth.

For the analyses and optimization of parameters in the following sections of this chapter, $\bar{\sigma}_{\text{group}}$ will be the metric we seek to reduce. In other words, the optimization of parameters will focus on reducing the average uncertainty within repeated measurements of the same table orientation.

Average compensated layer uncertainty

In the final results of the measured preforms, an additional uncertainty value will be provided – the *average compensated layer uncertainty* $\bar{\sigma}_{\text{comp}}$. This value is the average of the uncertainties of each layer's *compensated* detected angles. We can use the hypothetical data from layer 3 and the additional Table 5.5 to explain the derivation:

The first five measurements (i.e., group 1) provide us with five detected angles for layer 3, all of which are around 45°. This makes sense, because from the original [0/90/45/-45] stackup, layer 3 is at 45°. For the next five measurements (i.e., group 2), we expect the hypothetical detected angles to be near the stackup minus the turntable's rotation, or [0/90/45/-45] $-15°$ = [-15/75/30/-60]. This explains why the detected angles for layer 3 in group 2 are approximately 30°. This expectation continues for all groups 1–7.

If the angles of each group were to be compensated by their respective turntable orientation, we would then expect to have (for each of the four layers) a list of 35 angles near the original layer's orientation. For layer 3, that means we expect 35 independently detected angles near 45°. Table 5.5 provides the compensated angles from the original values in Table 5.4.

Group	Compensation	Layer 3 ($j = 3$) compensated angle					$\sigma^{(3)}_{\text{comp}}$
1	0°	45.5°	45.5°	45.5°	45.6°	45.6°	0.24°
2	+15°	45.1°	45.0°	45.0°	45.1°	45.1°	
3	+30°	45.3°	45.6°	45.5°	45.6°	45.2°	
⋮	⋮	⋮	⋮	⋮	⋮	⋮	

Table 5.5: Example data to illustrate the derivation of a preform's average compensated layer uncertainty. This data follows the standard scanning order shown in Table 5.3.

To determine $\bar{\sigma}_{\text{comp}}$ for this preform, the first step is the aforementioned angle compensation. Next, the uncertainty for each (compensated) layer j is calculated, where the uncertainty $\sigma^{(j)}_{\text{comp}}$ is the sample standard deviation of that layer's 35 compensated angles. The final average compensated layer uncertainty $\bar{\sigma}_{\text{comp}}$ is the arithmetic mean of the compensated layer uncertainties. If the compensated uncertainties of the hypothetical layers 1, 2, 3, and 4 were 0.16°, 0.20°, 0.24°, and 0.28°, then $\bar{\sigma}_{\text{comp}} = 0.22°$.

The compensated uncertainty $\bar{\sigma}_{\text{comp}}$ finds error which is hidden from the group uncertainty $\bar{\sigma}_{\text{group}}$: While the average group angle uncertainty across groups 1 and 2 is quite low at 0.05°, the average compensated layer uncertainty is 0.24°. The group uncertainty here is describing the typical detection error within repeated measurements at identical orientations; the compensated layer uncertainty is instead describing a systematic-based error across various orientations.

In other words, $\bar{\sigma}_{\text{comp}}$ tells us how accurate the entire ECT/2D-FFT and sX algorithm system is at detecting any given fiber layer angle, regardless of the orientation. In the next chapter, $\bar{\sigma}_{\text{comp}}$ will also allow us to compare the ECT results with the inherent systematic uncertainty within the sX system as presented in Section 5.2.

5.4 Optimization of the impedance cloud's phase angle

Another essential step in detecting layer angles with the sX system is the optimization of the phase angle of the complex impedance cloud. The claim in previous work at EVO by Hienz and Buelow [27] (as well as in external work by Bardl et al. [8]) is that the phase angle can be optimized for better angle detection results; however, no direct uncertainty analysis has ever been published regarding this phase angle rotation. This section describes the development of a phase angle optimization method within the sX system.

Rotating the impedance cloud

Figure 5.27 depicts the phase angle rotation of an impedance cloud. Figure 5.28 shows how rotating the phase angle affects the ECT image, 2D-FFT, and SUMCUT of an example preform scan. Note that for each phase angle the SUMCUT intensities are normalized to their maximum value – i.e., the highest peak value is 1.

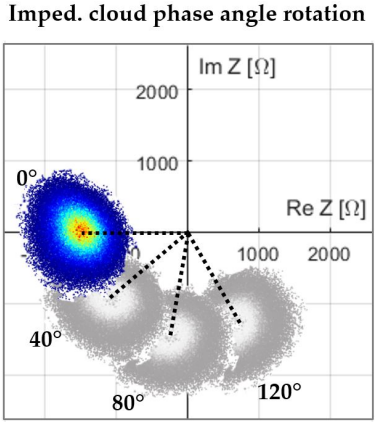

Fig. 5.27: Impedance cloud phase angle rotation.

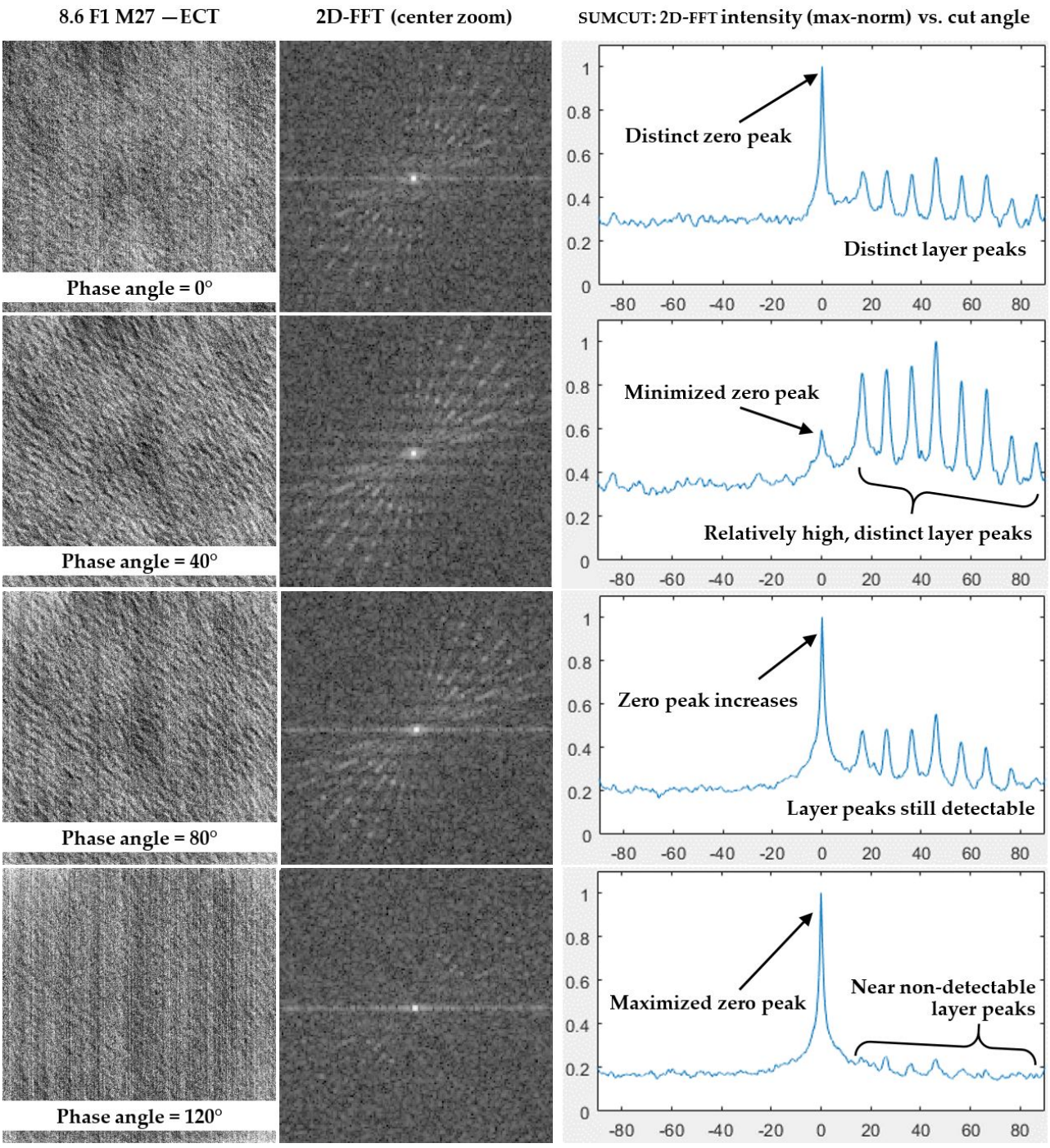

Fig. 5.28: Effect of phase angle rotation on ECT images, the 2D-FFT, and the resultant bilinear SUMCUT from preform 8.6 F1 M27.

Inspection of the SUMCUT plots in Fig. 5.28 reveals two seemingly related effects of during phase angle rotation:

1. the relative height of the zero peak decreases and increases; and
2. the distinctness of the layer peaks increases and decreases to near-non-detectability.

In other words, the zero peak height and layer peak detectability appear inversely related.

The relationship between phase angle and peak intensity

Figure 5.29 shows the mean-normalized zero peak and layer peak intensities for a phase angle sweep from 0° to 179°[10] using the same ECT data from Fig. 5.28. That is to say, for each phase angle in this plot, the following steps were made to calculate the resultant peak intensities:

1. an ECT image with that phase angle was generated;
2. a 2D-FFT from the ECT was calculated;
3. the sX bilinear SUMCUT method was applied to the 2D-FFT;
4. the SUMCUT curve was normalized to its mean[11]; and
5. the zero peak intensity and the peak intensities from layers 1, 2, and 3 were calculated.

The curves in Fig. 5.29 further prove the inverse relationship between zero peak intensity and layer peak intensity. It appears that to maximize the layer peak – and thus optimize the phase angle – the zero peak should be minimized. But does the minimization of the zero peak result in improved detection accuracy?

[10] Though the plot axis may show 180° as the sweep limit, the actual sweep ends at 179°; a phase angle rotation of 180° is just a flipped set of values from 0°.

[11] Mean-normalization makes the arithmetic mean of the curve equal to 1. In other words, the curve is divided by its average intensity. The significance of mean-normalization (as opposed to using the raw SUMCUT curve) is described later in this section.

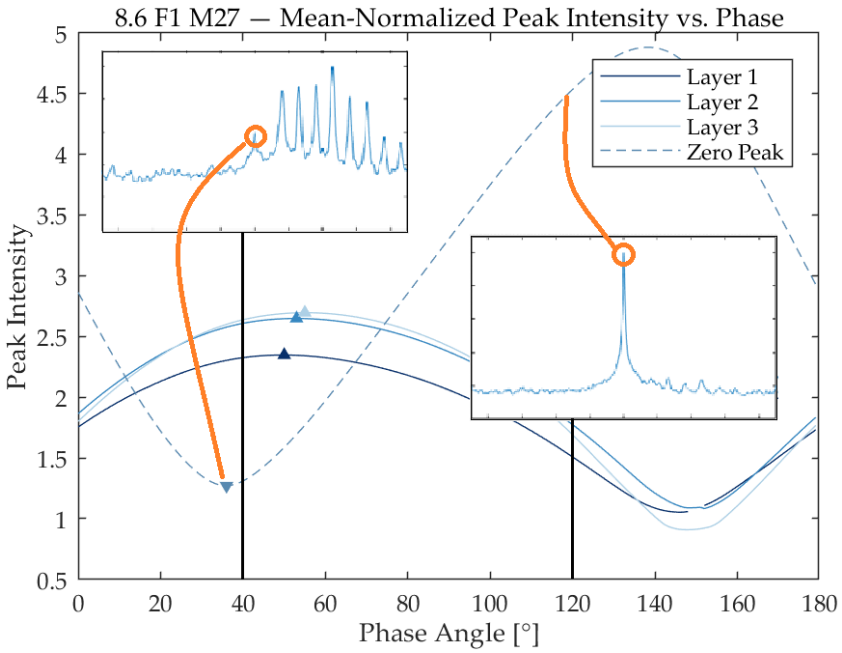

Fig. 5.29: Mean-normalized bilinear SUMCUT zero peak and layer 1–3 peaks for phase angle sweep 0°–179°.

The relationship between phase angle and detection accuracy

To investigate the relationship between phase angle and uncertainty in layer angle detection, we will employ $\bar{\sigma}_{\text{group}}$.[12] Figure 5.30 shows the mean-normalized zero peak and average layer 1–3 peak plotted alongside $\bar{\sigma}_{\text{group}}$ for a phase angle sweep from 0° to 179°. The same preform measurement (8.6 F1 M27) and peak extraction method from Fig. 5.29 was used, but now the arithmetic mean of the peaks from layers 1, 2, and 3 is shown instead of the three individual curves. The calculation of $\bar{\sigma}_{\text{group}}$ is made by using that phase angle for all 35 ECT images from preform 8.6.

The overall average group uncertainty $\bar{\sigma}_{\text{group}}$ – which is effectively a metric for the typical random uncertainty in the detected layer angle for all layers of a preform at a given frequency – is clearly minimized near the lowest zero peak. Likewise, $\bar{\sigma}_{\text{group}}$ increases when the phase angle rotates away from the angle of zero peak minimization. The gap in points for $\bar{\sigma}_{\text{group}}$ (between 120° and 160°) indicates that the layer peaks for layers 1–9 in preform 8.6) were indistinguishable from non-layer peak noise in the SUMCUT curves.

[12] See Section 5.3 for details.

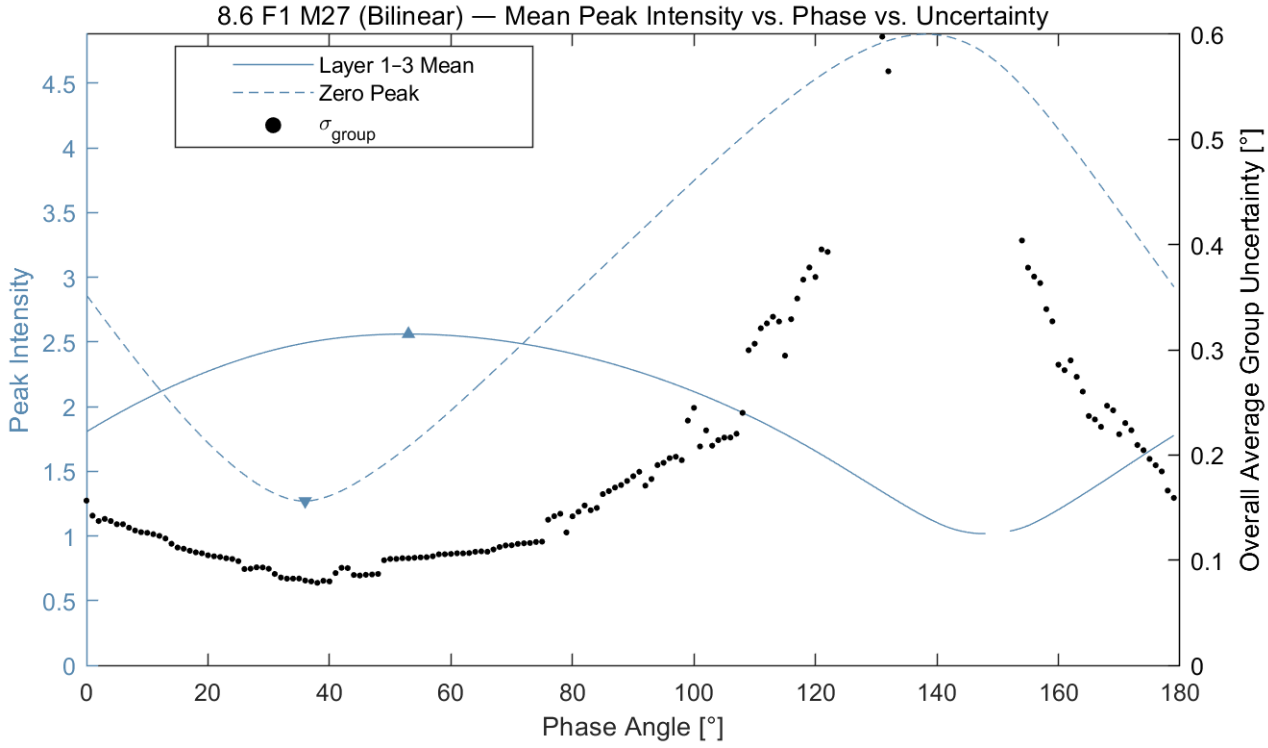

Fig. 5.30: Mean-normalized bilinear SUMCUT zero peak and average layer 1–3 peak plotted alongside $\bar{\sigma}_{\text{group}}$ for phase angle sweep 0°–179°.

Figure 5.31 provides the peak intensity plots from the same ECT data shown in Fig. 5.30, but instead for frequencies F2, F3, and F4. Differences between these plots are noted:

- The phase angle where the zero peak is minimized is not consistent across frequencies. For example, F2's zero peak is minimized at 70°, while for F4 this minimization occurs at 25°.

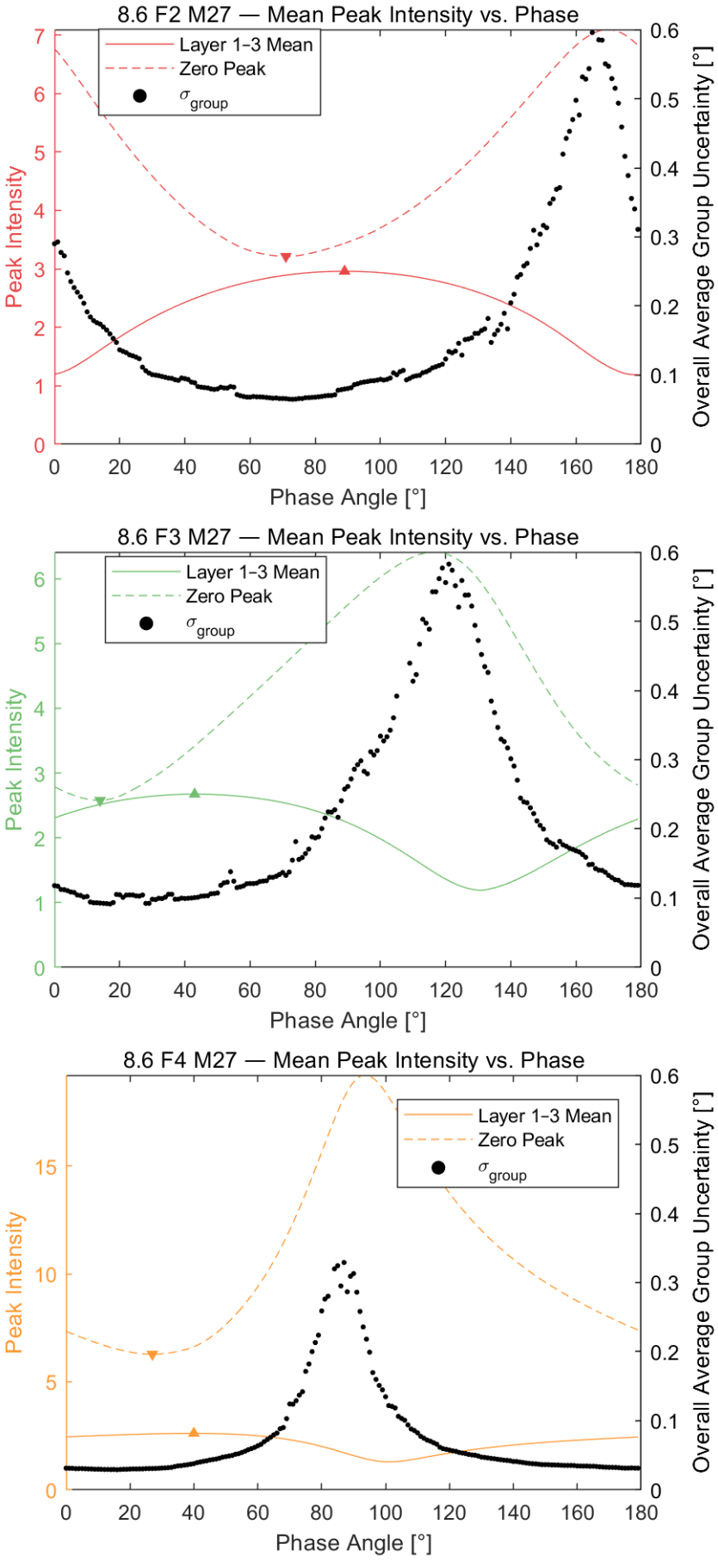

Fig. 5.31: Mean-normalized bilinear SUMCUT zero peak and average layer 1–3 peak plotted alongside $\bar{\sigma}_{group}$ for phase angle sweep 0°–179°, for frequencies F2, F3, and F4 of preform 8.6 M27.

- The relative intensities of the zero peak and layer peak are not equal across frequencies. At the minimized zero peak for F1, the layer peaks are twice as large. For F4, the layer peaks are never more than half the height of the zero peak.
- The optimized $\bar{\sigma}_{\text{group}}$ values are not equal across frequencies. For F4, the lowest uncertainty is about 0.04°; for F3 the lowest is more than double that at 0.10°.

Despite these differences in peak intensity results for the various frequencies, the phenomenon observed prior is still seen: The same relationship between the minimization of zero peak intensity, maximization of layer peak intensity, and reduction of $\bar{\sigma}_{\text{group}}$ is supported for all sensor frequencies.

A summary of this section so far: Rotating the phase angle from a given preform measurement affects the resultant SUMCUT plot. In the SUMCUT plot, the zero peak generally decreases when the layer peaks increase, and vice-versa. When the zero peak decreases, the overall average group uncertainty $\bar{\sigma}_{\text{group}}$ also decreases. Specifically, we have shown that the phase angle where the zero peak is minimized is approximately the phase angle with the lowest $\bar{\sigma}_{\text{group}}$.

Determining the optimal phase angle

In other words, we have shown that minimizing the layer angle uncertainty requires finding the phase angle which minimizes the mean-normalized zero peak. For the detection of preform layer angles with the sX algorithm system, we now define the *optimal phase angle* for a given ECT measurement as the phase angle which minimizes the mean-normalized zero peak.

Hence, the phase angle optimization for an individual ECT scan follows these steps:

1. Set the phase angle of the impedance cloud to 0°.
2. Create an ECT image from the real impedance components.
3. Produce a 2D-FFT from the image.
4. Evaluate the 2D-FFT with the bilinear[13] SUMCUT method.
5. Normalize the SUMCUT plot so that its mean is 1.
6. Find the intensity of the zero peak.
7. Rotate the impedance cloud's phase angle by $+1°$.
8. Repeat steps 2.–6. until the (mean-normalized) zero peak intensities for phases 0°–179° are known.
9. The optimal phase angle is the angle where the mean-normalized zero peak is at its lowest intensity – i.e., where the mean-normalized zero peak is minimized.

The advantage of basing the phase angle optimization on minimizing the bilinear mean-normalized zero peak is that it is independent of layer quantity and arrangement. No layer peaks need to be identified and calculated – only the bilinear SUMCUT needs to be generated and mean-normalized.

[13] Bilinear interpolation-based sampling for SUMCUT requires significantly less computational effort compared to spline interpolation. Additionally, no discernible improvement in phase optimization was observed when using spline interpolation.

The advantage of mean-normalization

Mean-normalization in particular must be implemented to increase phase optimization stability. Figure 5.32 compares the zero peak and layer peaks using the non-normalized (*raw*) SUMCUTS and the mean-normalized SUMCUTS for 8.6 F2 M34. Note that the peak for layer 1 appears connected to the zero peak at sub-optimal phase angles.

For preform 8.6, M34 belongs to measurement group 7. The table orientation for group 7 is −90°. Layer 1's fibers were initially oriented at 0°, but they are now (for M34) oriented at −90°. Recall that the fiber orientation in the ECT measurement is 90° rotated in the 2D-FFT. Therefore, the fibers of layer 1 – and therefore layer 1 itself – appears in the resultant SUMCUT as a peak near 0°. At sub-optimal phase angles, the zero peak effect becomes too large (or rather, the layer 1 peak becomes too small), and the resultant SUMCUT peak for layer 1 is "absorbed" into the zero peak itself. In other words, the zero peak *dominates*[14] the layer 1 peak in the SUMCUT, making layer 1 appear exactly equal to 0° at angles away from the optimal phase angle.

[14] The concept of zero peak domination is described in greater detail in the results of Chapter 6.

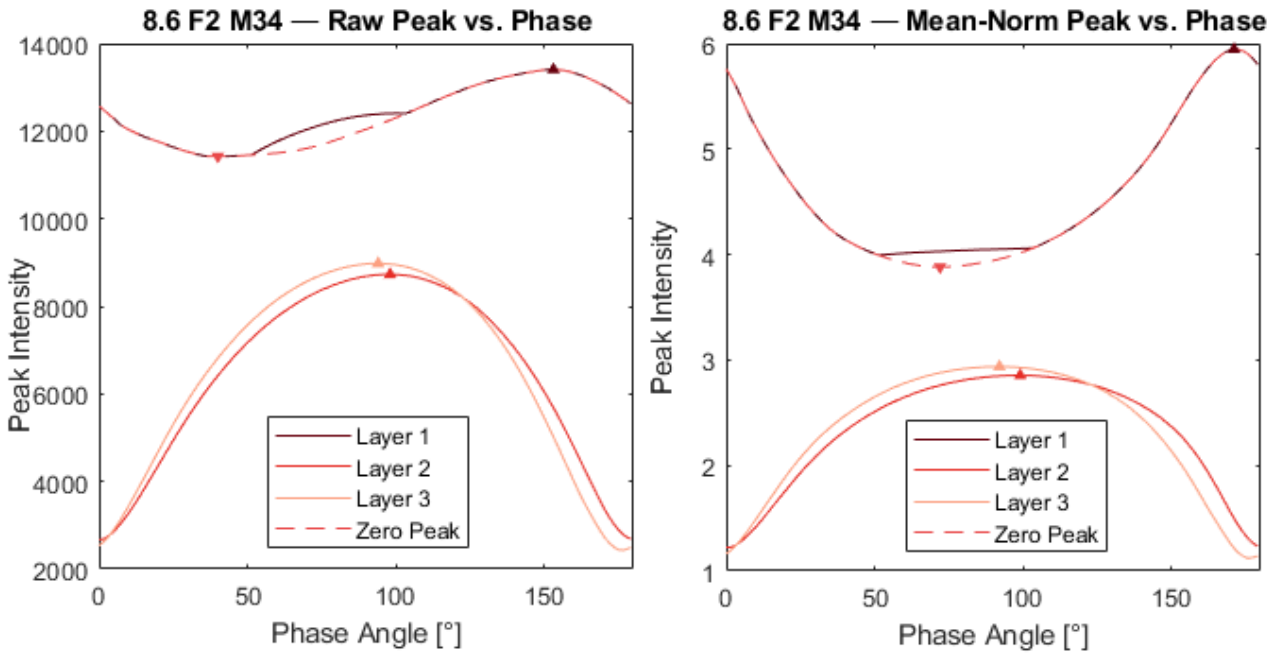

Fig. 5.32: Raw (i.e., non-normalized) and mean-normalized bilinear SUMCUT zero peak and layer 1–3 peaks for phase angle sweep 0°–179°. Similar to Fig. 5.29, but instead for 8.6 F2 M34.

Returning to the significant observation in Fig. 5.32, we see that the zero peak curve from the raw SUMCUTS is different than that from the mean-normalized SUMCUTS. Compared to the mean-normalized curve, the raw SUMCUTS provide a minimized zero peak – i.e., an optimal phase angle – which is further from the phase angle which maximizes the layers peaks. In other words, it appears that mean-normalization brings the optimized phase angle closer to the actual optimal angle.

Figure 5.33 shows the raw- and mean-normalization-based optimal phase angles for all 35 measurements from preform 8.6 F2. The optimized angles from the raw SUMCUTS are less consistent than those from the mean-normalized SUMCUTS. The mean-normalization phase angles remain between 40° to 80°, while the raw phase angles span a range of nearly 180°. In short, mean-normalization increases the stability of the optimal phase calculation for a given ECT scan.

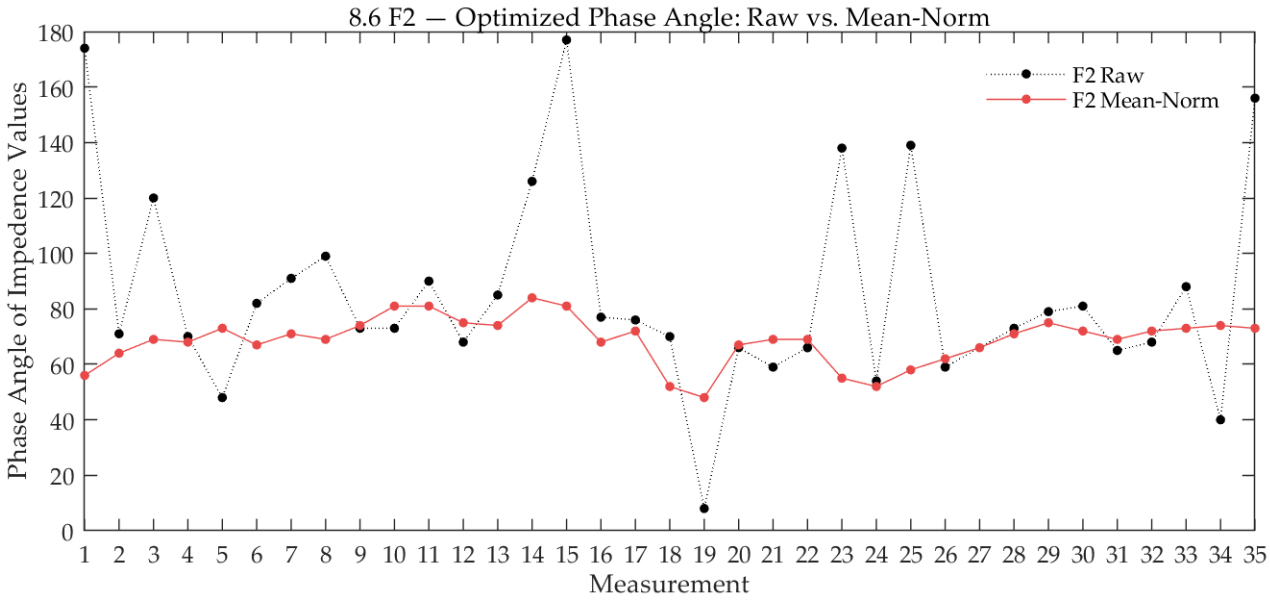

Fig. 5.33: Optimal phase angle calculated with raw (i.e., non-normalized) and mean-normalized bilinear SUMCUTS.

Averaging the optimal phase angles

Instead of using the individual optimal phase angle for each preform measurement in the final results, the *average optimal phase angle* for each preform–frequency combination is applied to all corresponding measurements. The reasoning behind this averaging is as follows:

Figure 5.34 shows the optimal phase angle of each measurement at each frequency for preforms 8.6 and 7.3. The phase optimization for individual ECT scans is stable for almost all measurements and frequencies in preform 8.6, but the optimized phase angles for 7.3 deviate considerably; even with mean-normalization, the resultant phase angle is not always stable.

By averaging the phase angles across each frequency and then applying the average optimal phase angle to all measurements for each preform–frequency combination, we can then ensure stable and consistent phase angle rotations in subsequent analyses. Table 5.6 lists the average optimal phase angle for each preform and frequency. The considerable deviation in phase angle for preform 8.6 is likely due to a different zeroing and/or initialization of the ECT sensor.

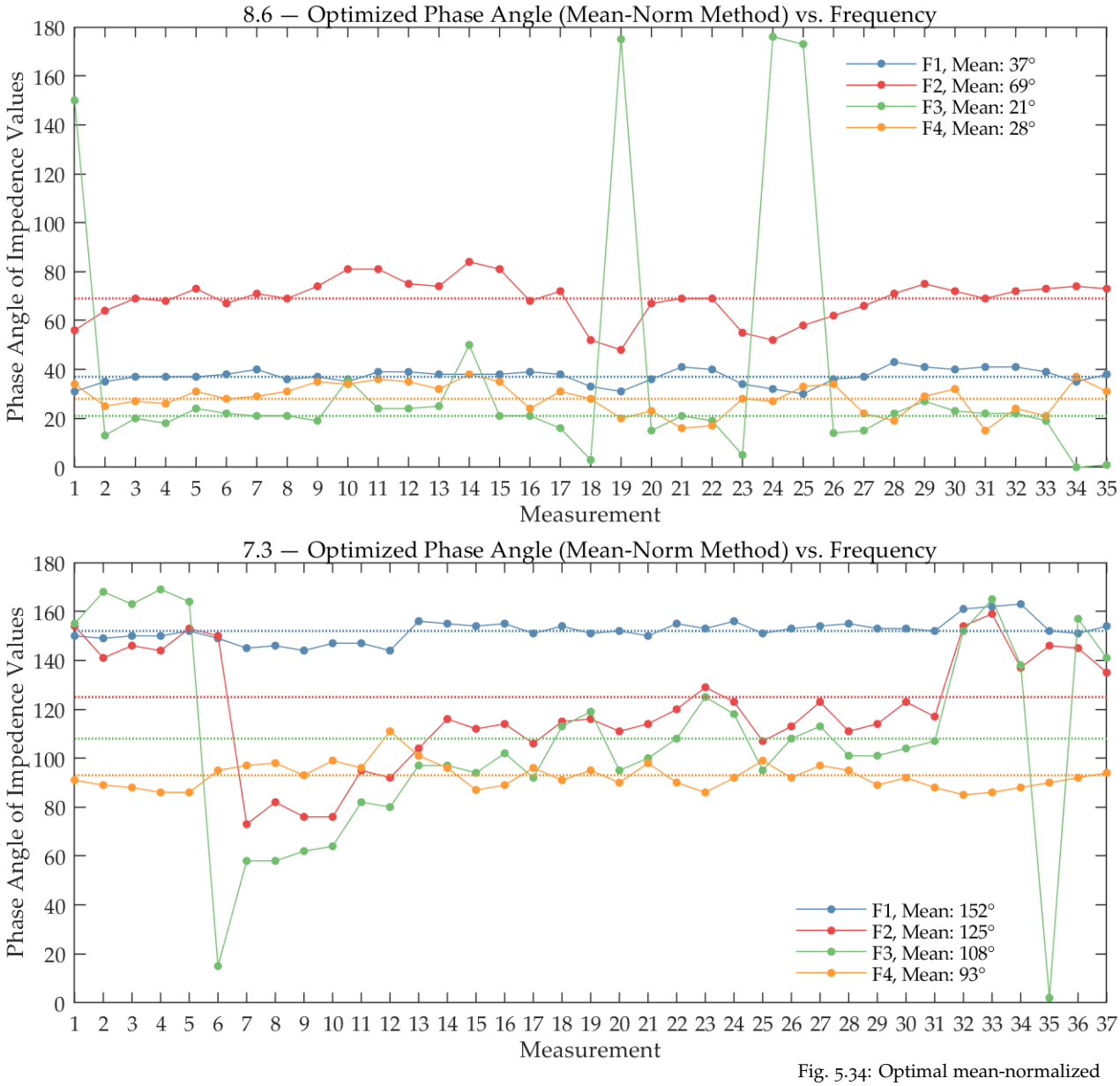

Fig. 5.34: Optimal mean-normalized phase angle of each measurement at each frequency for preform 8.6 and 7.3. For preform 7.3, two additional ECT scans were made.

Preform	Average mean-norm optimal phase angle									
	7.1	7.2	7.3	7.4	8.1	8.2	8.3	8.4	8.5	8.6
F1	153°	151°	152°	148°	152°	149°	150°	149°	151°	37°
F2	113°	116°	125°	109°	113°	105°	123°	110°	102°	69°
F3	102°	101°	108°	89°	99°	84°	87°	95°	86°	21°
F4	157°	154°	93°	148°	153°	148°	161°	153°	140°	28°

Table 5.6: Average mean-normalized optimal phase angle for all preforms and frequencies. Unless otherwise noted, these phases angles were used to generate the ECT images analyzed for the final layer angle detection uncertainty results presented in the following sections.

Chapter 6

Layer Angle Detection: Results

This chapter presents the uncertainty results from the ECT- and 2D-FFT-based layer angle detection analyses with sX, a system of algorithms whose methodology is described in the previous chapter. Before discussing the final optimized uncertainties of the preform data, the results of various sX parameter studies are first evaluated. Table 6.1 lists the studied sX parameters for ECT image processing and the SUMCUT algorithm.

Studied sX parameters	
ECT image processing	SUMCUT algorithm
Optimal phase angle	Angular resolution of cuts
Contrast	Sample point spacing
Windowing	Inner/outer sample point limits (IC/OC)

Table 6.1: sX system parameters studied prior to generating the final layer angle detection uncertainty results.

The parameter studies focused primarily on the ECT data from preform 8.6 for two main reasons:

1. Preform 8.6's stackup of [0/10/20/30/40/50/60/80] offers nine separate non-parallel layers. That is to say, there is only one layer per fiber orientation, and therefore each of the nine peaks in the SUMCUT belongs to just a single layer. This means parameter optimization is based on individual layers with no duplicates. Additionally, nine layers widens the the parameter optimization to a considerable layer depth.
2. The layers of 8.6 are aligned such that only one layer (layer 1) at the last table rotation (group 7) features a layer peak near the zero peak in the SUMCUT. This means only 5 of the 315 total detected layer angles[1] in 8.6 (for each frequency) is influenced by the zero peak. Because all other layer peaks are never aligned to the zero peak, the resultant $\bar{\sigma}_{\text{group}}$ is not affected by the zero peak effect.[2]

Additionally, the detectability of all layers with 8.6's F4 meant F4 was predominantly used in the parameter study.

[1] Nine (9) layers in 35 measurements is 315 total detectable layers.

[2] In the calculations of $\bar{\sigma}_{\text{group}}$ and $\bar{\sigma}_{\text{comp}}$ for the following studies and results for 8.6, the detected angles from layer 1 in group 7 are not included.

The detection of layers in both the parameter studies and the final results was based on an automated approach. Because of the presence of false peaks along each SUMCUT curve, manually preprogrammed angle ranges were used to filter out the true peaks. For each preform, each layer's order and orientation was set as the expected layer peak angle based on a sample SUMCUT. A level of angular "play" was added to both sides of the expected peak angle to allow for deviation in the detected angle. If a layer peak was not detected within the expected range, the detection results returned no angle. The angles in the final results were verified out of the automated system.

6.1 Parameter study: ECT image processing

The previous ECT image processing algorithms at EVO from Hienz and Buelow [27] featured parameters which altered the ECT images with the intention to improve the accuracy of detected layer angles. Three of these parameters – phase angle rotation, contrast, and windowing – were studied in the scope of this thesis. While the optimization of phase angles was already presented in Section 5.4 as part of the sX system methodology, this section discusses the other two parameters.

Contrast

The application of contrast results in a remapping of a given image's intensity along the display range [33]. Figure 6.1 shows the effect of contrast on an ECT image. The majority of the intensities are forced to a narrow band of the grayscale range $[0, 255]$ by extreme outliers, thus degrading the visual detection of differences in the ECT data.

When the intensity values within three standard deviations (3 STD) are filled to the entire intensity range – i.e., when a 3 STD contrast is applied – the image's highlights appear brighter and its shadows appear darker. This sharpening of black–white differences is further increased with a 1.5 STD contrast. That is to say, the values of the original image which lay within 1.5 standard deviations of the average intensity now fill the grayscale range; values outside this contrast level simply fill the range extremes.

Although not investigated for the pseudo images because they were already visually analyzable, applying contrast to ECT images is aesthetically favorable, and was subsequently applied in previous algorithms from Hienz and Buelow [27] with the intention of improving ECT/2D-FFT layer angle detection.

Table 6.2 lists the results of the uncertainty study on the effects of contrast to the resultant $\bar{\sigma}_{\text{group}}$ from preform 8.6 F4. When stronger contrast is applied – i.e., when the standard deviation range is decreased – the uncertainty $\bar{\sigma}_{\text{group}}$ increases. This makes sense because information from the ECT is effectively "lost" to the black and white extremes of the grayscale when contrast is applied.

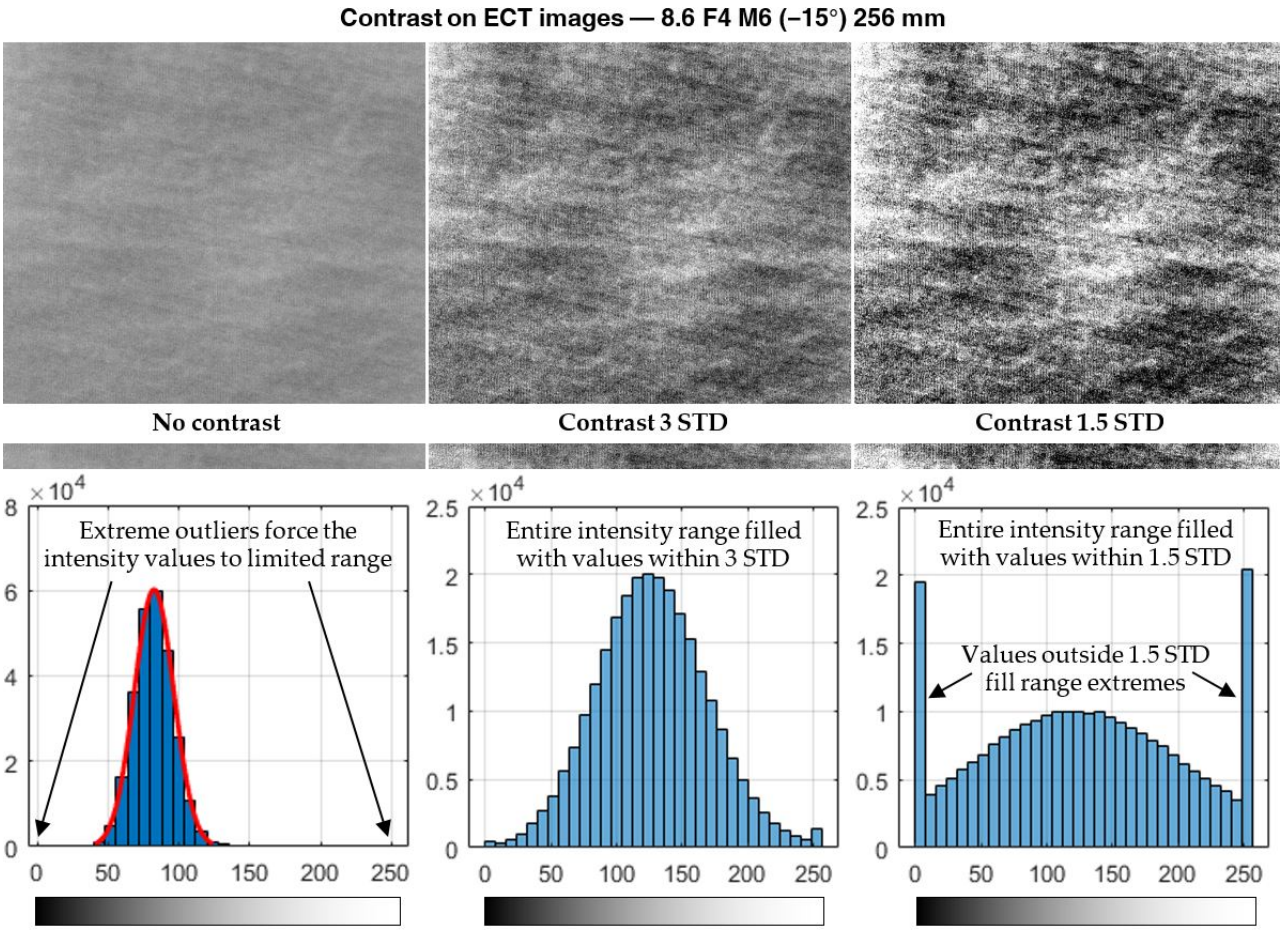

Fig. 6.1: Application of different contrast amounts to an example ECT image.

Between none and 2.5 STD contrast, no considerable uncertainty difference is made. This is likely due to the reduction of only extreme outliers. Hence, for the numerical analysis of ECT images with sX, none to 2.5 STD contrast can be applied. Nevertheless, contrast serves its purpose as an aesthetic enhancer for images, just as the logarithmic scale is used for 2D-FFT visualization. (Indeed, most ECT images shown this thesis were applied with a 2 STD contrast.)

Windowing

As described and verified in the pseudo image analysis of Section 5.2, windowing reduces noise in the 2D-FFT by limiting spectral leakage. Again, previous analyses at EVO by Hienz and Buelow [27] incorporated windowing into the parent algorithms with the goal of improving ECT/2D-FFT layer angle detection. Table 6.3 lists the uncertainty results of the windowing study on $\bar{\sigma}_{\text{group}}$ from preform 8.6 F4.

Contrast — Effect on overall average group uncertainty

Contrast (STD)	$\bar{\sigma}_{\text{group}}$	% difference from minimum
None	0.0288°	0%
3.0	0.0290°	0.50%
2.5	0.0288°	0.03%
2.0	0.0297°	2.48%
1.5	0.0324°	10.41%
1.0	0.0407°	34.25%
0.5	0.0539°	72.12%

ECT parameters

Preform/frequency	8.6/F4
Image size	256 mm × 256 mm
Windowing	Hamming
Contrast	**Varied**

SUMCUT parameters

Interpolation	Bicubic spline
Cut angular res.	0.01°
Sample spacing	1 px
IC/OC limits	10 px/90 px

Table 6.2: Effect of contrast on $\bar{\sigma}_{\text{group}}$.

Windowing — Effect on overall average group uncertainty

Window	$\bar{\sigma}_{\text{group}}$	% difference from minimum
None	0.0386°	30%
Hann	0.0316°	8%
Hamming	0.0290°	0%
Gauss $\alpha = 2.5$	0.0299°	3%

ECT parameters

Preform/frequency	8.6/F4
Image size	256 mm × 256 mm
Windowing	**Varied**
Contrast	3 STD

SUMCUT parameters

Interpolation	Bicubic spline
Cut angular res.	0.01°
Sample spacing	1 px
IC/OC limits	10 px/90 px

Table 6.3: Effect of windowing on $\bar{\sigma}_{\text{group}}$.

The improvement in detection accuracy from no window to windowing is significant at a 30% difference from the minimum value, which belongs to the Hamming window. Differences between different window functions also exist, and the apparent optimal window – the Hamming function – disagrees with previous analyses which showed the Hann function to be optimal. Nevertheless, because this analysis shows Hamming to provide the lowest overall average group uncertainty $\bar{\sigma}_{\text{group}}$, Hamming is applied as the windowing function for the final analyses.

6.2 Parameter study: SUMCUT algorithm

The proposed SUMCUT algorithm for extracting layer angles from 2D-FFTs features three modifiable parameters (apart from the interpolation scheme): 1) The angular resolution of the cuts, 2) the sample point spacing along each cut, and 3) the IC/OC start/stop limits for the sample points. This section describes the studies regarding these SUMCUT parameters.

Cut angular resolution

Table 6.4 lists the uncertainty results of the cut angular resolution study on $\bar{\sigma}_{\text{group}}$ from preform 8.6 F4. As the angular resolution decreases – i.e., as the number of cuts across the $-90°$ to $+90°$ sweep increases – the resultant $\bar{\sigma}_{\text{group}}$ decreases. This makes sense because the fineness of the sampling across the 2D-FFT increases, and therefore more information is being pulled from the matrix; however, the uncertainty in layer angle detection accuracy begins to plateau near $0.01°$. Also, the relative improvement in uncertainty at this plateau is minimal compared to the additional computational effort. Therefore, to balance accuracy and calculation time, a cut resolution of $0.01°$ is used in the final analyses.

Cut angular resolution — Effect on overall average group uncertainty

Cut angular res.	Total cuts	$\bar{\sigma}_{\text{group}}$	% difference from minimum
0.1°	1800	0.0343°	18.5%
0.05°	3600	0.0309°	7.3%
0.02°	9000	0.0290°	1.2%
0.01°	18000	0.0290°	1.1%
0.005°	36000	0.0287°	0%

Table 6.4: Effect of cut angular resolution on $\bar{\sigma}_{\text{group}}$.

ECT parameters

Preform/frequency	8.6/F4
Image size	256 mm × 256 mm
Windowing	Hamming
Contrast	3 STD

SUMCUT parameters

Interpolation	Bicubic spline
Cut angular res.	**Varied**
Sample spacing	1 px
IC/OC limits	10 px/90 px

Sample point spacing

Table 6.5 lists the uncertainty results of the sample point spacing study on $\bar{\sigma}_{\text{group}}$ from preform 8.6 F4. As the point spacing decreases – i.e., as the number of sample points along each cut increases – the resultant $\bar{\sigma}_{\text{group}}$ decreases slightly.

Sample point spacing — Effect on overall average group uncertainty

Pt. spacing	$\bar{\sigma}_{\text{group}}$	% difference from minimum
1 px	0.028 99°	1.5%
0.5 px	0.028 59°	0.1%
0.2 px	0.028 56°	0%
0.1 px	0.028 61°	0.2%

ECT parameters	
Preform/frequency	8.6/F4
Image size	256 mm × 256 mm
Windowing	Hamming
Contrast	3 STD
SUMCUT parameters	
Interpolation	Bicubic spline
Cut angular res.	0.01°
Sample spacing	**Varied**
IC/OC limits	10 px/90 px

Table 6.5: Effect of sample point spacing on $\bar{\sigma}_{\text{group}}$.

The noted decrease in $\bar{\sigma}_{\text{group}}$ would appear to make sense because the sampling fineness across the 2D-FFT increases. The 2D-FFT however is already limited by discrete values with 1 px spacing, so no truly "new" information is being sampled.

With spacing below 1 px, the points along the cut are no longer sampling finer information; instead, the interpolation schemes are being applied to estimate the values between pixels, and do so with minimal improvement in accuracy. In fact, the change in detection uncertainty occurs only in the third significant digit at the expense of integer-multiples in computational effort. Because a cut resolution of 0.01° already generates a nearly plateaued uncertainty value, the final analyses use 0.01° for the sake of SUMCUT efficiency.

Inner and outer circle limit

The inner and outer circle (IC/OC) parameter in the SUMCUT algorithm describes the inner and outer sum limits for each cut, effectively acting as a band pass filter against low and high 2D-FFT frequencies, respectively. Figure 6.2 illustrates the implementation of two IC/OC pairs on an identical 2D-FFT from 8.6 F4 M1. The 3 px/127 px IC/OC pair – a "broad" band which sums points between (and including) 3 px and 127 px from the 2D-FFT center – has less distinct peaks for deeper layers than those from the "narrow" band 20 px/90 px pair. The right-most peak is especially more distinct with the narrow IC/OC band. From the example in Fig. 6.2 we see that IC/OC enables filtering of 2D-FFT noise, and consequently alters the layer peaks in the SUMCUT plot. But is there an optimal parameter?

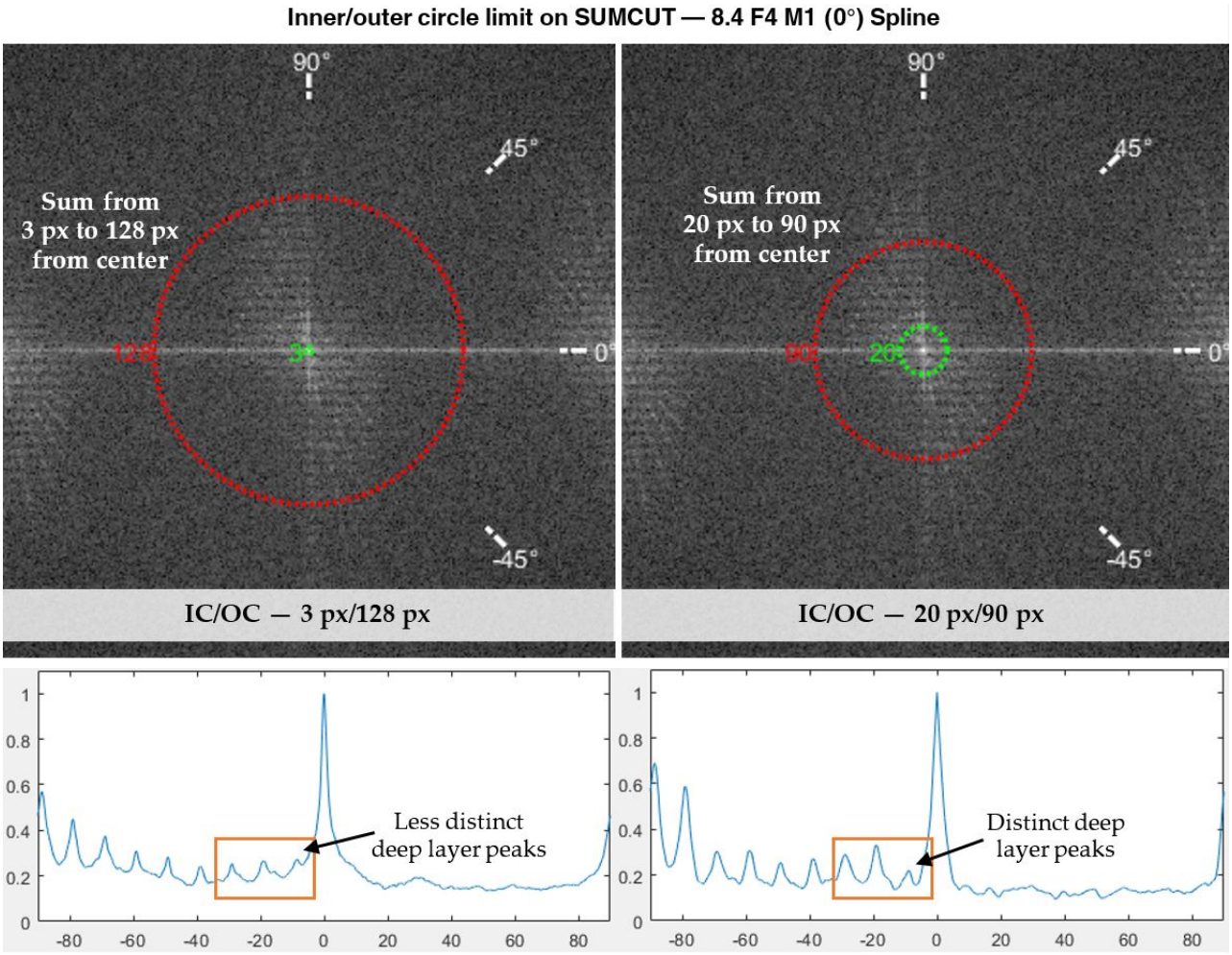

Fig. 6.2: Effect of inner and outer circle cut limits on SUMCUT layer peaks.

In this thesis, the optimization of IC/OC is driven (and constrained) by two goals:

1. find the IC/OC pair which minimizes $\bar{\sigma}_{\text{group}}$; and
2. find the IC/OC pair which enables the detection of all layers.

Therefore, the ignore-if-not-detected logic in the automated peak detection code[3] is appended with a constraint: If the given IC/OC combination cannot identify every layer across every measurement,[4] then that combination is deemed *unacceptable*.

To find the optimal IC/OC parameter, the $\bar{\sigma}_{\text{group}}$ of every IC/OC combination from 3 px to 127 px[5] was calculated for 8.6 F1–F4, and then the lowest value was identified. Figure 6.3 and 6.4 visualize the results for the bilinear- and spline-based IC/OC optimization for F4. The horizontal axis is IC, and the vertical axis is OC. The color of each point represents the relative logarithmic value of $\bar{\sigma}_{\text{group}}$. Points with no color are unacceptable IC/OC pairs – i.e., one or more layer(s) are undetectable in one or more measurements. The respective minimized $\bar{\sigma}_{\text{group}}$ is listed in each plot. Table 6.6 lists the parameters.

[3] Explained in the introduction to Chapter 6 on p. 67.

[4] Recall that for 8.6 the only occurrence of a layer peak being coincident with (and therefore affected by) the zero peak is layer 1 in measurement group 7. Hence, the detected peaks for layer 1 for M31–M35 are excluded from this detectability constraint.

[5] The lower/upper limits for IC/OC were set to prevent the SUMCUT curves from being "flooded" by the strong center 2D-FFT values and the outside 2D-FFT noise.

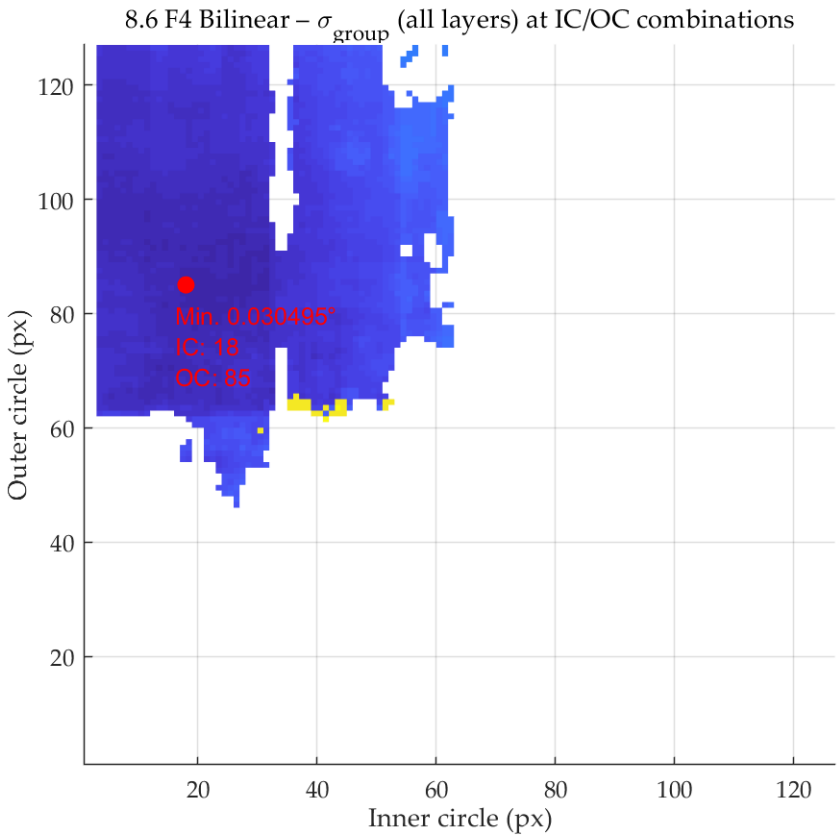

Fig. 6.3: Acceptable IC/OC combinations for 8.6 F4 with bilinear interpolation in SUMCUT. Color scale is relative logarithmic, where the lowest $\bar{\sigma}_{group}$ is blue, and the highest is yellow. Absence of colored points indicates unacceptable IC/OC combinations – i.e., not all layers are detectable in all measurements.

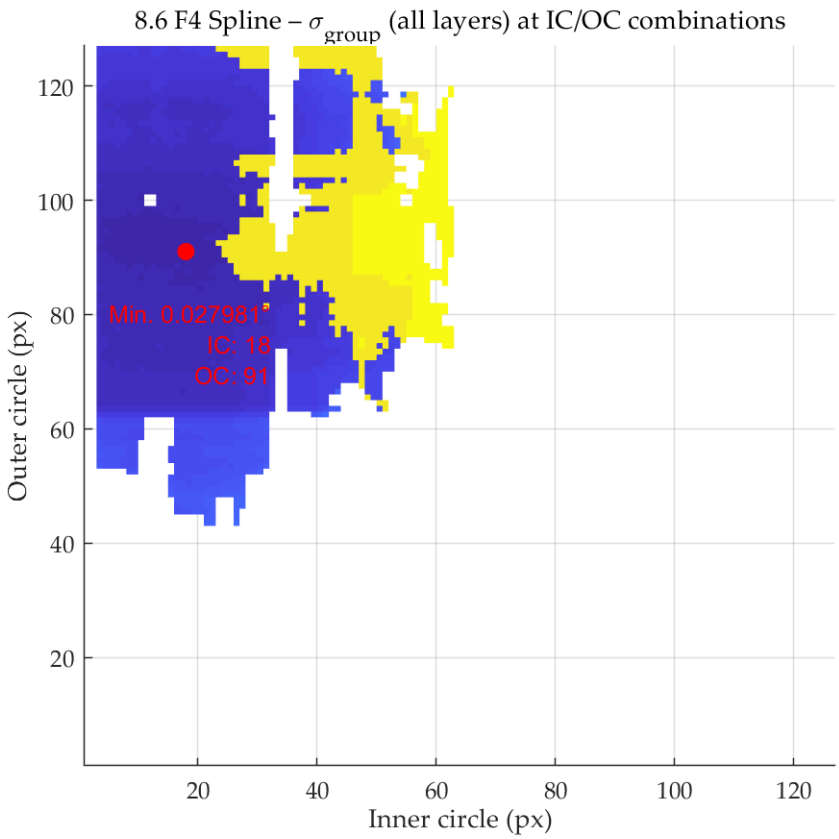

Fig. 6.4: Acceptable IC/OC combinations for 8.6 F4 with spline interpolation in SUMCUT. Color scale is relative logarithmic, where the lowest $\bar{\sigma}_{group}$ is blue, and the highest is yellow. Absence of colored points indicates unacceptable IC/OC combinations – i.e., not all layers are detectable in all measurements.

From Fig. 6.3 and 6.4 we see that a minimum OC of about 45 px is necessary to detect all layers in all measurements. This makes sense because if higher frequency intensities (of the layers) are excluded, less layer-indicative 2D-FFT intensities are summed. Likewise, the maximum IC is about 60 px, because otherwise the lower frequency intensities are excluded. Additionally, as IC is increased – i.e., as more low frequencies are filtered out – the $\bar{\sigma}_{\text{group}}$ tends to worsen.

For F1, F2, and F3, no optimal IC/OC was calculated because not all layers could be identified in every measurement. Table 6.6 lists the results of a second IC/OC analysis, this time with the all-layer detection initial constraint relaxed to the top four layers. That is to say, for a IC/OC combination to be permissible, each of the top four layers in 8.6 must be identifiable for each measurement. The top four layers generally produce the strongest peaks in SUMCUT plots, and hence this "top 4" constraint is implemented. The uncertainty values are the average of the average group uncertainty for layers 1–4 ($\bar{\sigma}^{1-4}_{\text{group}}$), not the *overall* average group uncertainty $\bar{\sigma}_{\text{group}}$, which is the average from all nine layers.

Inner/outer circle limit — Optimal combination (all layers)

	Bilinear		Spline	
Freq.	IC/OC [px]	$\bar{\sigma}_{\text{group}}$	IC/OC [px]	$\bar{\sigma}_{\text{group}}$
F1 F2 F3*	—	—	—	—
F4	18/85	0.030°	18/91	0.028°

Inner/outer circle limit — Optimal combination (top 4 layers)

	Bilinear		Spline	
Freq.	IC/OC [px]	$\bar{\sigma}^{1-4}_{\text{group}}$	IC/OC [px]	$\bar{\sigma}^{1-4}_{\text{group}}$
F1	19/79	0.039°	3/91	0.041°
F2	11/118	0.032°	11/73	0.031°
F3	16/110	0.046°	3/111	0.044°
F4	12/85	0.016°	9/115	0.019°

ECT parameters

Preform/frequency	8.6/F4
Image size	256 mm × 256 mm
Windowing	Hamming
Contrast	None

SUMCUT parameters

Interpolation	**Varied**
Cut angular res.	0.01°
Sample spacing	1 px
IC/OC limits	**Varied**

Table 6.6: Optimization of IC/OC with all layers ($\bar{\sigma}_{\text{group}}$) and top four layers ($\bar{\sigma}^{1-4}_{\text{group}}$) of 8.6. *No IC/OC combination for F1, F2, or F3 allowed the detection of all nine layers at all measurements.

Table 6.6 shows that even within the ECT measurements of a single preform specimen, the optimal IC/OC for each frequency is significantly different. Therefore, the final layer angle detection uncertainty results for each of the ten preforms are based on their individual optimization of IC/OC. These optimal IC/OC pairs are listed alongside the final uncertainties in Section 6.4.

6.3 Mitigating zero peak domination

The last step before establishing the final angle detection uncertainties involves mitigating the domination of the zero peak. Figure 6.5 shows the spline SUMCUTS from F1 and F4 of 7.1 M6, both with visible zero peaks. The zero peak – this sharp rise in the SUMCUT curve at exactly 0° – is a direct product of the vertical striping effect seen in ECT images, which itself is a measurement artifact from the sensor scanning method. When layer peaks in the SUMCUT are near 0°, they can be influenced or even completely *dominated* by the zero peak.

Up until now, we have primarily used the 8.6 data to study and optimize various system parameters within the ECT/2D-FFT-based sX system. As stated in the introduction of this chapter, no layer in the measurements of 8.6 was ever aligned such that its respective peak was influenced by zero peak domination.[6] Hence, the study and optimization of various parameters was made free of the zero peak's influence.

In the ECT measurements of all other preforms 7.1–8.5, there are multiple instances where the fiber patterns in the resultant 2D-FFTS are aligned in the zero direction. In other words, there are multiple instances where the layer peaks in the SUMCUT plot are near 0°, and therefore are susceptible to zero peak domination. To decrease the influence of the zero peak on the final results of all preforms, two levels of mitigation were implemented:

1. using the ECT data from F1; and
2. using bicubic spline interpolation in the SUMCUT algorithm.

[6] Except for layer 1 in measurement group 7, the detected angles of which were excluded from previous analyses as noted earlier in this thesis.

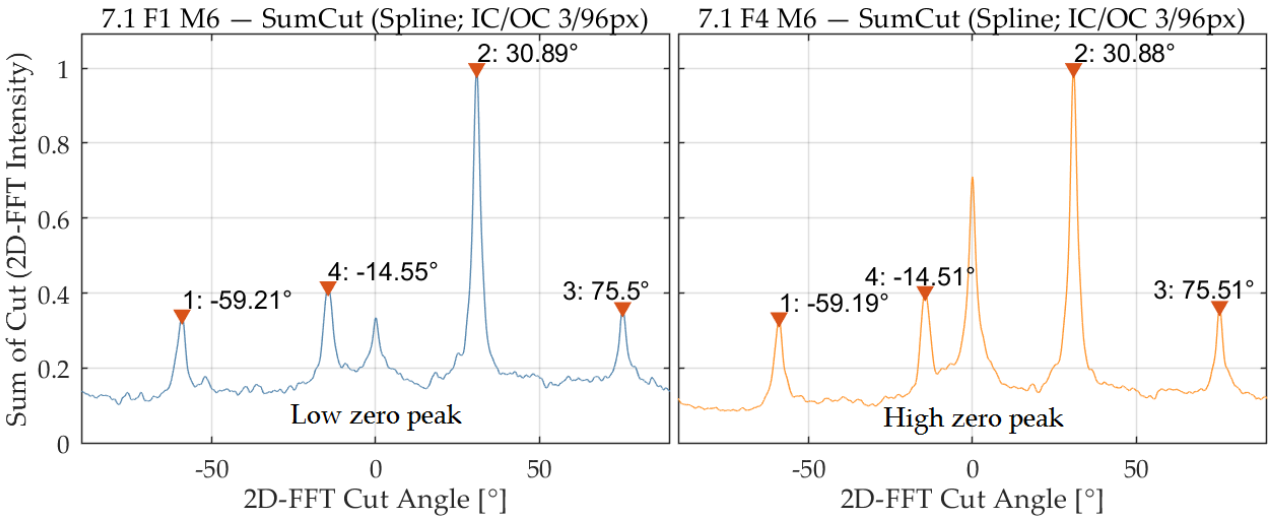

Fig. 6.5: Zero peak effect difference between F1 (left) and F4 (right) relative to layer peaks in 7.1 M6.

Level 1: Using frequency 1 ECT data

The pure zero peak in Fig. 6.5 for F1 is notably lower than for F4, even though the layer peak intensities are relatively similar. Figure 6.6 shows the same preform (7.1) and frequencies (F1 and F4) as Fig. 6.5 but at M1 – a measurement with a table orientation which aligns

layer 4's peak near the zero peak. While for both frequencies the layer 4 peak is affected by the zero peak, the domination of the zero peak in F1 is significantly reduced.

Table 6.7 lists the F1/F4 layer angles from 7.1 M6, M6 compensated,[7] and M1. The difference between the M6 compensated and M1 layer angles is also listed.

[7] Recall that a compensated layer angle is one whose respective table orientation is added to the resultant angle, therefore compensating for the table's rotation. For $M6_{comp}$, the angular compensation is +15°.

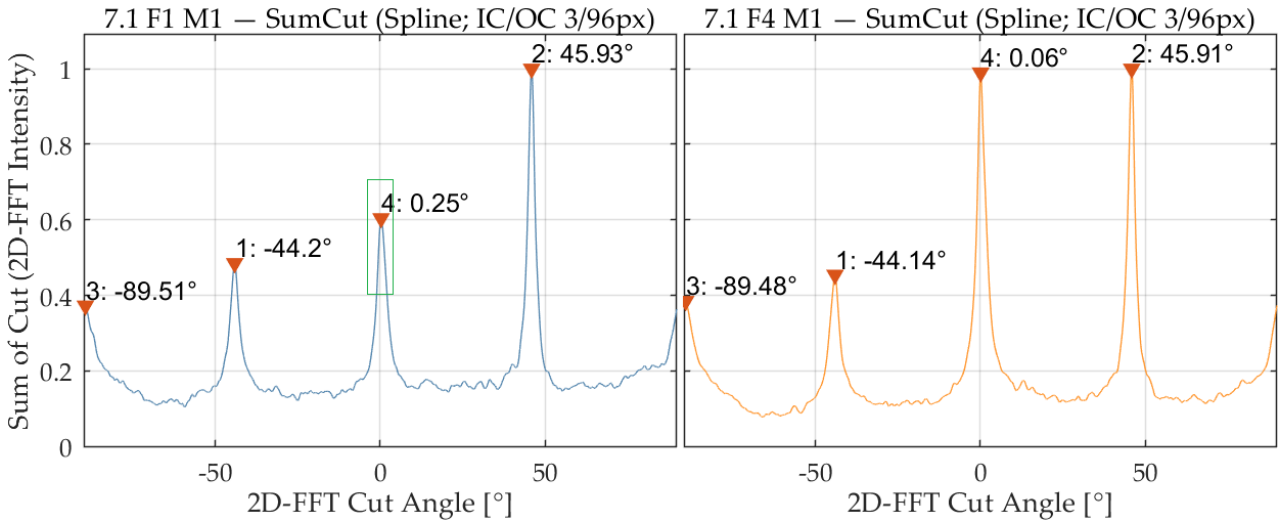

Fig. 6.6: Difference in zero peak domination along layer 4 for F1 (left) and F4 (right) in 7.1 M1.

The difference between $M6_{comp}$ and M1 for F1 and F4 in Table 6.3 reveals a mitigation of the zero peak influence: The difference between $M6_{comp}$ and M1 for layers 1, 2, and 3 are $\leq$0.05° for both F1 and F4. For layer 4, the differences for F1 and F4 are significantly larger at 0.20° and 0.43°, respectively.

This increase in difference is evidence of the zero peak's influence on the detected angle of layer 4; however, F1's angle was shifted by half the amount of F4. For F2 and F3, analysis showed the difference was comparable to that of F4. Therefore, to reduce the influence of the zero peak on the final uncertainty results for preforms 7.1–8.5, ECT data exclusively from F1 is used.

Zero peak domination — Mitigation with F1 versus F4 on 7.1

Meas.		Spline-based SUMCUT-detected layer angles L1 (F1/F4)	L2 (F1/F4)	L3 (F1/F4)	L4 (F1/F4)
7.1 M6	+15° ↓	−59.21°/−59.19°	+30.89°/+30.88°	+75.50°/+75.51°	−14.55°/−14.51°
7.1 $M6_{comp}$		−44.21°/−44.19°	+45.89°/+45.88°	−89.50°/−89.49°	+0.45°/+0.49°
7.1 M1		−44.20°/−44.14°	+45.93°/+45.91°	−89.51°/−89.48°	+0.25°/+0.06°
$\lvert M6_{comp} - M1 \rvert$		0.01°/0.05°	0.04°/0.03°	0.01°/0.01°	→ 0.20°/0.43° ←

Table 6.7: Influence of frequency on the zero peak domination in detected and compensated angles in 7.1.

Level 2: Using spline interpolation with SUMCUT

Even when using the F1 ECT data, the zero peak nevertheless has an influence on the layer peaks when they are near 0° in the 2D-FFT. To provide a second level of mitigation against zero peak domination for preforms 7.1–8.5, the bicubic spline (and not bilinear) interpolation scheme for sampling in SUMCUT is used. Figure 6.7 shows the bilinear SUMCUT of 7.1 F1 M1 (left), the corresponding zero peak (top-right), and the spline zero peak (bottom-right) from the SUMCUT in Fig. 6.6.

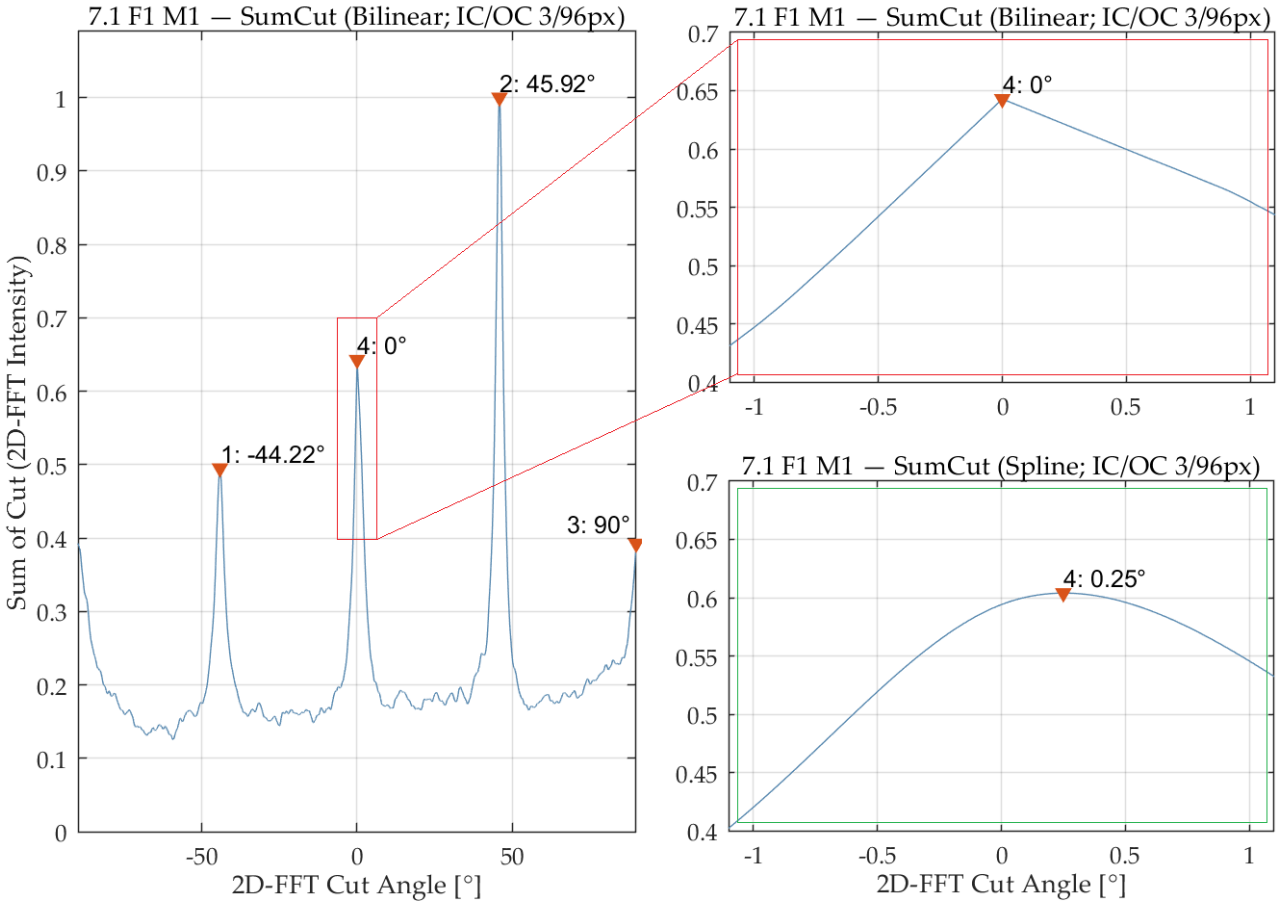

Fig. 6.7: Zero peak effect difference between bilinear and (bicubic) spline SUMCUT interpolation schemes for 7.1 F1 M1.

The bilinear SUMCUT shows peaks at exactly 0° and 90°, while the spline SUMCUT reveals peaks slightly off the vertical and horizontal directions. In other words, not only is the influence of the zero peak reduced in the spline SUMCUT, but the effect of 90° artifacts in 2D-FFT is also reduced. This 2D-FFT artifact mitigation seems to be a product of the overshoot ability of spline interpolation. To further mitigate zero peak domination in the final layer angle uncertainty results of 7.1–8.5, spline interpolation is used.

6.4 Final layer angle detection uncertainty results

Table 6.8 lists the layer angle detection uncertainties[8] $\bar{\sigma}_{\text{group}}$ and $\bar{\sigma}_{\text{comp}}$ from all preforms 7.1–8.6 using the ECT/2D-FFT-based sX algorithms and their respective optimized parameters. For F1, preform 8.1 exhibits the lowest overall average group uncertainty (0.021°) and lowest average compensated layer uncertainty (0.086°). The highest uncertainty pair belongs to 8.3 with 0.116° and 0.191°, respectively.

Despite these low values for the eight-layered 8.1, it should be noted that the preform specimen has a symmetrical stackup; since each layer orientation is featured twice, the 2D-FFT intensities – and therefore the SUMCUT peaks – show only four discernible fiber directions. These fiber directions are "reinforced," and therefore the resultant $\bar{\sigma}_{\text{comp}}$ (which is an overall average of compensated layer uncertainties) does not provide an accurate measure for non-duplicate fiber angle detection.

[8] A description of the calculation of $\bar{\sigma}_{\text{group}}$ and $\bar{\sigma}_{\text{comp}}$ is provided in Section 5.3.

Table 6.8: Final $\bar{\sigma}_{\text{group}}$ and $\bar{\sigma}_{\text{comp}}$ results from all preforms. Two orientations in immediate brackets (e.g., [0/90]) signify a woven fabric. *Excludes group 7 layer 1 detected angles.

Final overall (all-layer) $\bar{\sigma}_{\text{group}}$ and $\bar{\sigma}_{\text{comp}}$

Preform	$\bar{\sigma}_{\text{group}}$	$\bar{\sigma}_{\text{comp}}$	Stackup
7.1	0.044°	0.119°	45/-45/0/90
7.2	0.050°	0.110°	45/-45/90/0
7.3	0.048°	0.179°	0/90/45/-45
7.4	0.043°	0.132°	[45/-45]/[0/90]
8.1	0.021°	0.086°	0/45/90/-45/-45/90/45/0
8.2	0.070°	0.142°	0/0/45/45/90/90/-45/-45
8.3	0.116°	0.191°	0/90/10/-80/20/-70/30/-60
8.4	0.090°	0.176°	[0/90]/[10/-80]/[20/-70]/[30/-60]
8.5	0.053°	0.139°	[10/-80]/[20/-70]/[30/-60]/[40/-50]
8.6	0.091°	0.144°	0/10/20/30/40/50/60/70/80
8.6 F4*	0.028°	0.083°	——

ECT parameters

Preform/frequency	**Varied**/F1
Image size	256 mm × 256 mm
Image resolution	512 px × 512 px
Phase angle	**See Table 5.6**
Windowing	Hamming
Contrast	None

SUMCUT parameters

Interpolation	Bicubic spline
Cut angular res.	0.01°
Sample spacing	1 px
IC/OC limits	**See Table 6.10**

To bring cross-specimen relevance to the $\bar{\sigma}_{\text{comp}}$ results, a truncated averaging to the lowest common fiber direction count is provided. Table 6.9 lists the top-four average compensated layer uncertainty $\bar{\sigma}_{\text{comp}}^{1-4}$, which is the average group uncertainty across the top four discernible fiber directions.[9] The percent difference from the overall "all-layer" $\bar{\sigma}_{\text{comp}}$ from Table 6.8 is also listed. Figure 6.9 visualizes these results.

[9] For 8.4 and 8.5 (which both have biaxial woven layers), the averaging means the top two layers' (and therefore top four fiber directions') uncertainties.

$\bar{\sigma}_{comp}$— Overall versus top four			
Preform	$\bar{\sigma}_{comp}$	$\bar{\sigma}^{1-4}_{comp}$	% diff.
7.1	——	0.119°	
7.2	——	0.110°	
7.3	——	0.179°	
7.4	——	0.132°	
8.1*	——	0.086°	
8.2*	——	0.142°	
8.3	0.191°	0.086°	-76%
8.4	0.176°	0.167°	-5%
8.5	0.139°	0.151°	+8%
8.6	0.114°	0.085°	-52%
8.6 F4	0.083°	0.064°	-26%

Table 6.9: Top four discernible fiber directions. *Symmetrical (duplicate) layers – i.e., two layers per detected fiber angle.

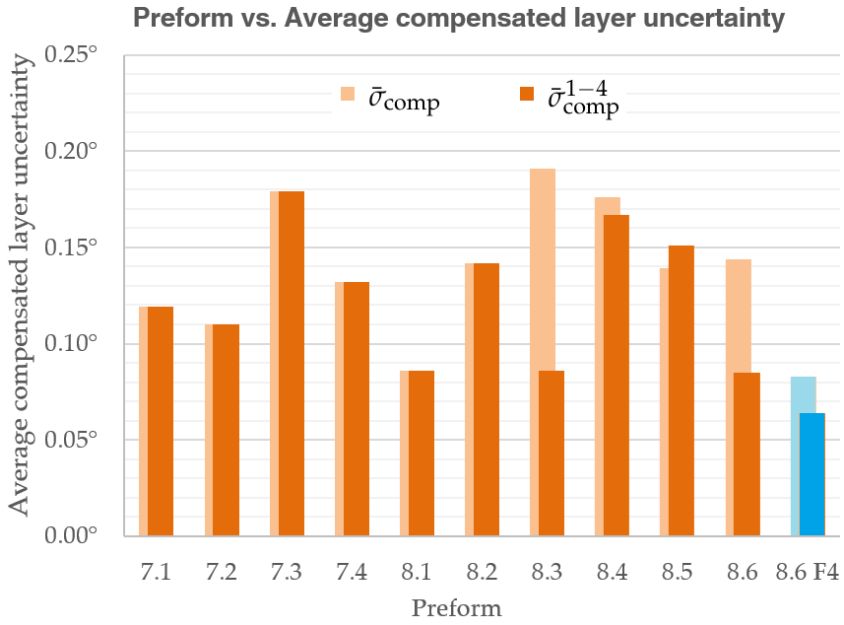

Fig. 6.8: All-layer average compensated uncertainty $\bar{\sigma}_{comp}$ and top-four-layer average compensated uncertainty for each preform specimen at F1.

The plot in Fig. 6.8 shows that (except for 8.5) there is a consistent and significant decrease in uncertainty when averaging the top four fiber directions instead of all layers. This depth–uncertainty relationship is discussed later in this section.

The lowest compensated layer uncertainty $\bar{\sigma}^{1-4}_{comp}$ from all the preforms at F1 belongs to 8.6 at 0.085°. For 8.6 F4 – i.e., the sole zero-peak-unaffected preform – the $\bar{\sigma}^{1-4}_{comp}$ is 0.064°. Because of its superior detection qualities and nine-layer structure, 8.6's results will specifically be examined in this section.

Restrictions for certain IC/OC optimizations

Table 6.10 lists the lower and upper restrictions on the IC/OC optimizations for each preform. As mentioned in the initial IC/OC optimization of 8.6 in Section 6.2, the default IC minimum restriction of 1 px was intended to prevent "flooding" of the SUMCUT by the center intensity.

The default OC restriction of 127 px was intended to avoid 2D-FFT border artifacts. For certain preforms, the OC maximum was further restricted in the IC/OC optimization to avoid the effect of disruptive non-fiber-direction 2D-FFT intensities[10] within the typical layer frequency range.

Figure 6.9 is a cropped portion of the 2D-FFT from 8.4 F1 M16 showing its optimized IC/OC. The OC restriction for 8.4 was 72 px. The intense 2D-FFT points near – but not exactly along – the intensity bands of the fiber directions just outside the 69 px radius are close enough to disrupt the detected layer angles in the resultant SUMCUT. The visible points inside the OC restriction are also not directly indicative of the fiber directions, but they are not near the layer intensity bands, and therefore do not disrupt the detected angles.

[10] The non-fiber-direction intensities seen in certain 2D-FFTs are predominant in preforms with woven fibers. The sharp, distinct 2D-FFT intensities are hence indicative of the weave pattern, and not the actual fibers themselves.

Optimized F1 IC/OC for Table 6.8

Preform	IC [px]	OC [px]	OC restrict.
7.1	3	96	
7.2	30	90	90
7.3	8	61	63
7.4	6	121	
8.1	9	93	
8.2	4	67	
8.3	10	63	63
8.4	6	69	72
8.5	13	94	
8.6	3	91	
8.6 F4	18	91	

Table 6.10: Optimized IC/OC pairs from all preforms. Unlisted OC restriction indicates default 127 px. †Top four layer-based.

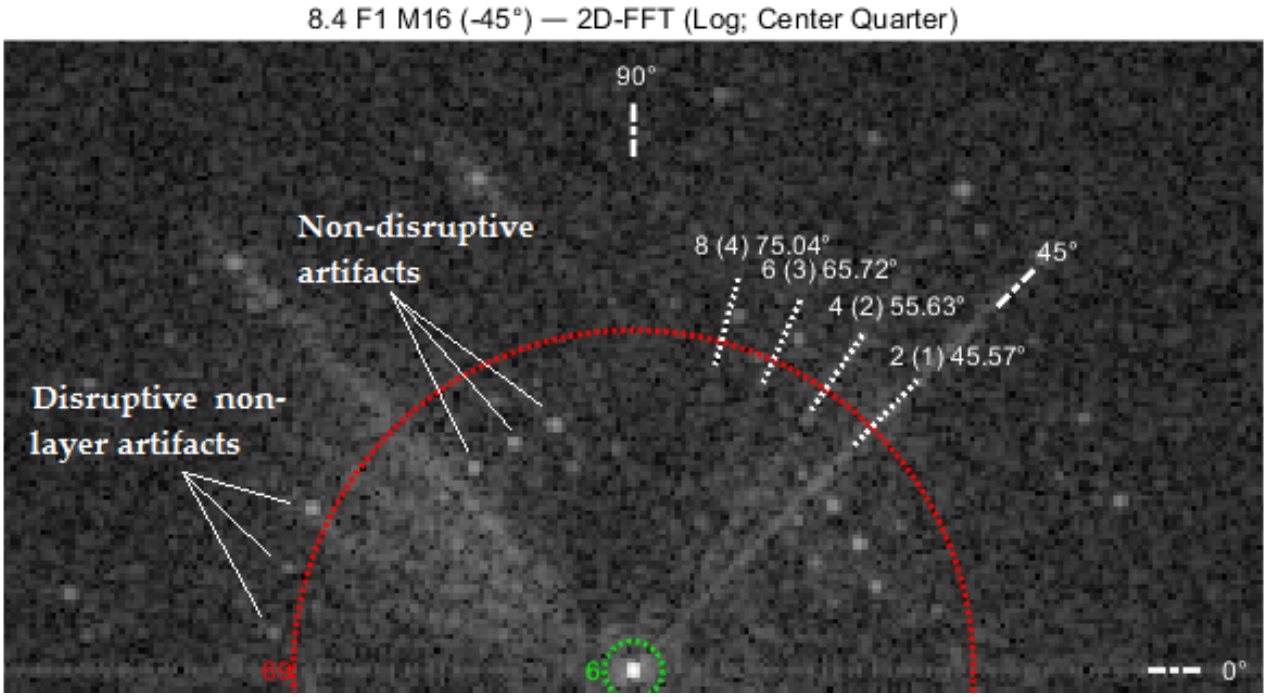

Fig. 6.9: Cropped center 2D-FFT from 8.4 F1 M16 with 69 px OC.

Layer depth versus uncertainty

Figure 6.10 shows the per-layer average group uncertainty $\bar{\sigma}^j_{\text{comp}}$ and compensated uncertainty $\bar{\sigma}^j_{\text{comp}}$ for each layer in 8.6 F1. The first notable feature is an exponential-like relationship appearing to exist between layer depth and uncertainty. In other words, the deeper a layer is located, the less accurate its fiber direction can be detected. This could be attributed to the well-documented exponential decay of eddy current intensity with material depth [34].

The other notable feature is that at every layer depth, $\bar{\sigma}^j_{\text{comp}}$ is always larger than its corresponding $\bar{\sigma}^j_{\text{group}}$. This means that the detected layer angles within repeated measurements at an identical table (and hence layer) orientation remain more accurate than the overall orientation-less accuracy. In other words, an increased $\bar{\sigma}^j_{\text{comp}}$ implies error is introduced at different table orientations.

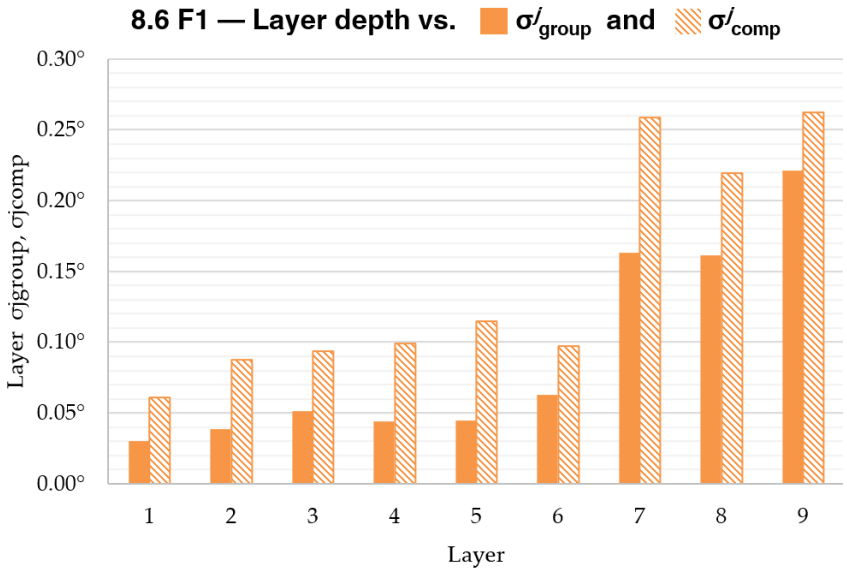

Fig. 6.10: Per-layer average group uncertainty $\bar{\sigma}^j_{\text{group}}$ and compensated uncertainty $\bar{\sigma}^j_{\text{comp}}$ for the nine layers of 8.6 F1.

Frequency 1 versus frequency 4

Figure 6.11 shows the per-layer average group uncertainty $\bar{\sigma}^j_{\text{group}}$ for 8.6 F1 and F4. Recall that while F1 was chosen to mitigate the influence of the zero peak effect on detected layer angles, the measurement for 8.6 was made such that nearly all layers are free from the zero peak effect, thus permitting a robust uncertainty analysis.

In all per-layer uncertainties in Fig. 6.11, F4 shows a distinct improvement in layer angle detection accuracy. Most notably is the difference in $\bar{\sigma}^j_{\text{group}}$ for layers 7–9. Also, while the detected angle for F1 suffers a sharp increase in uncertainty, F4's uncertainty increases only slightly. In short, F4 provides a superior detection accuracy.

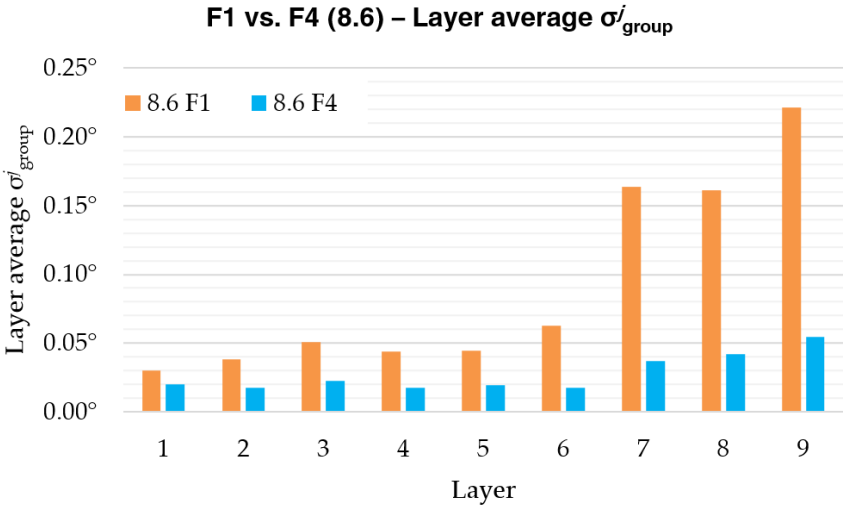

Fig. 6.11: 8.6 $\bar{\sigma}^{j}_{\text{group}}$ with F1 and F4.

Bicubic spline versus bilinear

Recall that spline was specifically chosen for the final uncertainty analyses to mitigate the zero peak effect in the layer peaks of preforms 7.1–8.5; bilinear was shown to be weak against the zero peak effect in the 2D-FFT. For the 8.6 measurements, however, nearly all layers are free from the zero peak, thus allowing an undisturbed comparison between bilinear and spline results.

Figure 6.12 shows the individual per-layer compensated uncertainties $\bar{\sigma}^{j}_{\text{comp}}$ for 8.6 F4 with both SUMCUT interpolation schemes. The spline interpolation scheme – although seen as superior to bilinear in the preliminary uncertainty investigation with pseudo images in Chapter 5 – does not provide such a significant increase in orientation-independent detection accuracy.

The conclusion from this lack of difference between spline and bilinear is this: If the zero peak effect was mitigated (or even removed) through changes in the ECT measurement itself, bilinear interpolation in the SUMCUT algorithm would still offer satisfactory uncertainty at a significantly reduced computational effort.

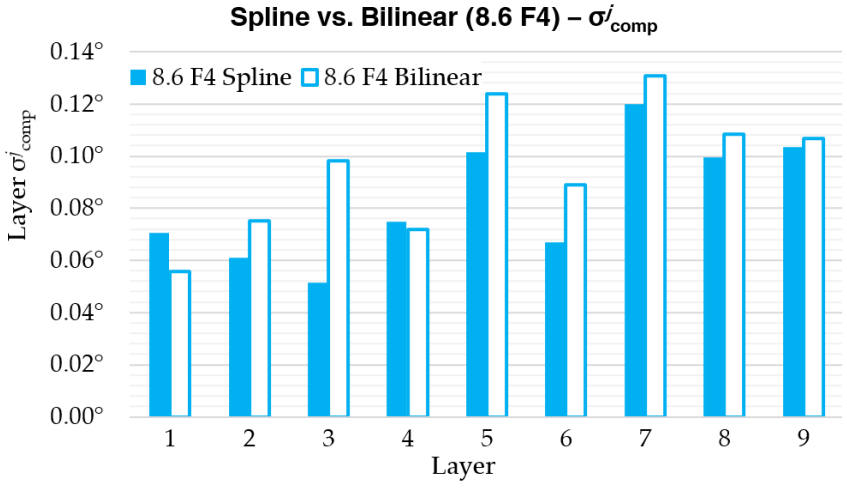

Fig. 6.12: 8.6 F4 $\bar{\sigma}^{j}_{\text{comp}}$ for (bicubic) spline and bilinear interpolation schemes in SUMCUT.

Sources of error

The results for $\bar{\sigma}_{\text{comp}}$ in comparison to $\bar{\sigma}_{\text{group}}$ show us that a source of detection error exists for an arbitrary orientation of a given layer. Possible significant sources for the error introduced when the preform is rotated include the following:

- **Non-coincident equipment/specimen rotation**: Though attempts were made to center the table, preform, and scanning path of the sensor – i.e., to make the rotational axes coincident – this cannot be guaranteed with 100% accuracy. With respect to non-coincident rotational axes, the ECT images from different table orientations therefore do not contain identical fiber structure data. Fiber waviness (which cannot be completely mitigated) would thus produce different detected layer angles.
- **Unequal image corners**: The fiber structure shown in the corners of the ECT images changes as the table rotates. If the fibers were aligned perfectly throughout the specimen, then the orientation of the ECT image area – and even the location of the scanned area along the specimen – would not affect the detected layer angles. Again, fiber waviness cannot be completely mitigated, so variations in scanned area means the resultant detected layer angles carry through a variation in fiber orientation.
- **Error within the sX algorithms**: The sX system detects the fiber orientation of layer angles with discrete ECT images, discrete 2D-FFTs, and interpolation schemes. Each of these elements introduces a level of error.

The uncertainty in the table's absolute orientation is 0.006° as noted in Section 5.1 [28]. Although the resultant layer angle detection uncertainty is certainty affected by the table's rotational uncertainty, 0.006° is less than 10% of the final $\bar{\sigma}_{\text{comp}}$ uncertainties, and thus not a significant contributor to the $\bar{\sigma}_{\text{comp}}$ results.

The error introduced by the sX system to the final results can be compared with the validation made in Chapter 5. With the use of pseudo images, we saw that the SUMCUT algorithm has an uncertainty inversely proportional to the pixel intensity distance from the 2D-FFT center. In short, this means that the sX system has an inherent uncertainty which introduces a finite level of systematic error.

The standard deviation in the detected angle (with SUMCUT) of a pseudo image which produces a 2D-FFT point 96 px from the center is 0.017° and 0.088° with spline and bilinear interpolation, respectively. Compared to typical $\bar{\sigma}_{\text{comp}}$ values (which almost all are generated with OC limits near 96 px), these uncertainty values are in a similar range. In short, the accuracy in the ECT detection of preform layer angles (in this thesis) is likely limited by the mathematical error inherently introduced with discrete ECT images and 2D-FFTs.

Chapter 7

Conclusion

The objective of this master's thesis was to investigate the uncertainty in two areas of DLR's EVO facility, namely, in 1) the handling of dry carbon fiber fabrics and 2) the layer angle detection of carbon fiber preforms with ECT/2D-FFT methods.

For the analysis of fabric handling, a method needed to be developed to determine the absolute position of a quadrilateral fabric sheet. The method proposed in this thesis involves 3D laser scanning equipment, edge-fit corner intersections, and geometric manipulation. The uncertainty (defined in this thesis as the sample standard deviation) of this measurement approach using the defined parameters is 0.11 mm translationally and 0.01° rotationally. The two fabric handling steps specifically examined – the vacuum-based gantry transfer from the cutter to the storage drawer and then to the preparation table – exhibited translational uncertainties no larger than 0.22 mm and rotational uncertainties no larger than 0.03°.

Despite the apparent robustness of the proposed fabric position calculation method, the uncertainty of the examined fabric handling steps is still within the same order of magnitude as the measurement uncertainty. The conclusion is that the measured uncertainty values were highly influenced by the measurement method itself. Hence, a more accurate method to analyze the position of fabric cutouts should be developed if more rigid claims are needed regarding the exact uncertainty in fabric handling.

Nevertheless, in future work, the proposed 3D scan-based approach appears to be a reliable way to determine fabric movement. This simplified 2D approach could be extended towards non-quadrilateral cutouts because the vertex-based center of mass calculation is a generalized formula; however, when analyzing the placement of fabrics in 3D – e.g., draped along preform molds – a surface-based calculation of the center of mass is likely necessary.

The preform layer angle detection system implemented at EVO relies on the well-documented combination of ECT to create images of the underlying component fiber structure and 2D-FFT to determine the predominant patterns – in this case the fibers – of those ECT images. Despite this method's successful implementation in recent literature, the specific approach by which layer angles are extracted

has never been openly published nor successfully investigated for its uncertainty.

This thesis presents a set of algorithms collectively known as sX which replace the existing flawed system at EVO for calculating the layer angles of preforms with ECT and 2D-FFT. The sX system is centered around the SUMCUT principle, which projects cuts around the 2D-FFT with evenly spaced, interpolation-based sampling points, and results in a SUMCUT plot showing the fiber directions as peaks. Pseudo images were analyzed with 2D-FFT and SUMCUT to validate the underlying mathematical methodology of sX. An optimization scheme for the impedance phase angle, which relies on SUMCUT as well, is also a key element of the sX system.

Existing 256 mm $\times$ 256 mm ECT measurements from 10 preform specimens with varying material, structure, and stackups were examined with sX to determine the corresponding uncertainty in ECT/2D-FFT-based layer angle detection. The presence of the "zero peak effect" – a significant disturbance in the existing measurements – was mitigated by analyzing 1.895 MHz data combined with the bicubic spline interpolation scheme in SUMCUT.

The results from sX show that for preforms with four distinct fiber directions – e.g., with four unidirectional layers or two biaxial layers – the uncertainty in the detected angle of an arbitrarily oriented layer is on average no more than 0.20° with the described measurement approach. The results from a nine-layered preform with unidirectional fibers at nine orientations support the relationship between detection uncertainty and layer depth. Lastly, limited results from a higher frequency of 6.265 MHz (on a preform whose results were not disturbed by the zero peak effect) showed reduced uncertainties compared with 1.895 MHz, thus supporting the relationship between higher ECT sensor frequencies and detection accuracy.

For future uncertainty investigations of the sX system at EVO – and ECT in general – the vertical striping which causes the zero peak effect must be addressed. A potential starting point for this future work could be the measurement process itself; continuous sensor movement during measurement may be the source of this striping issue, as work by Bardl et al. [8] – which instead implement a "stop-and-go" measurement technique – appears to have no striping artifacts.

Beyond the detection of layer angles, the sX system could be used to check for waviness by comparing the width of SUMCUT peaks from known specimens to the peaks of measured components; the wider the peak, the more deviation in the layer's fibers. Also, if the scanning path resolution was increased, different areas of a given image could be compared to check for consistency in fiber direction.

Additional research on the ECT/2D-FFT angle detection method is necessary before it can be implemented in the commercial RTM-based production of aerospace components. Nevertheless, the results of this thesis support and encourage its use as a non-destructive testing method for quality assurance along the production chain.

Bibliography

[1] D. Darmofal, "16.100 Aerodynamics," 2005. [Online]. Available: https://ocw.mit.edu/courses/aeronautics-and-astronautics/16-100-aerodynamics-fall-2005/

[2] L. Jensen and B. Yutko, "Why Budget Airlines Could Soon Charge You to Use the Bathroom," *FiveThirtyEight*, June 2014. [Online]. Available: https://www.fivethirtyeight.com/features/if-everyone-went-to-the-bathroom-before-boarding-the-plane-ticket-prices-might-be-lower/

[3] M. Maynard, "No speck too small as U.S. airlines search for fuel savings," *The New York Times*, June 2008. [Online]. Available: https://www.nytimes.com/2008/06/11/business/worldbusiness/11iht-air.1.13628276.html

[4] Massachusetts Institute of Technology, "On the Road in 2035: Reducing Transportation's Petroleum Consumption and GHG Emissions," 2008. [Online]. Available: http://web.mit.edu/sloan-auto-lab/research/beforeh2/otr2035/

[5] United States Environmental Protection Agency, "Light-Duty Automotive Technology, Carbon Dioxide Emissions, and Fuel Economy Trends: 1975 Through 2011," 2012. [Online]. Available: https://nepis.epa.gov/Exe/ZyPURL.cgi?Dockey=P100DYX6.TXT

[6] US Energy Information Administration, "How much carbon dioxide is produced from burning gasoline and diesel fuel?" 2017. [Online]. Available: https://www.eia.gov/tools/faqs/faq.php?id=307&

[7] C. Schmidt, C. Schultz, P. Weber, and B. Denkena, "Evaluation of eddy current testing for quality assurance and process monitoring of automated fiber placement," *Composites: Part B*, vol. 56, pp. 109–116, August 2013. [Online]. Available: https://doi.org/10.1016/j.compositesb.2013.08.061

[8] G. Bardl, A. Nocke, C. Cherif, M. Pooch, M. Schulze, H. Heuer, M. Schiller, R. Kupke, and M. Klein, "Automated detection of yarn orientation in 3D-draped carbon fiber fabrics and preforms from eddy current data," *Composites: Part B*, pp. 312–324, April 2016. [Online]. Available: https://www.doi.org/10.1016/j.compositesb.2016.04.040

[9] Hancox NL., "The compression strength of unidirectional carbon fibre reinforced plastic," *Journal of Material Science*, vol. 10, pp. 234–242, 1975.

[10] H. Heuer, M. Schulze, M. Pooch, S. Gaebler, A. Nocke, G. Bardl, C. Cherif, M. Klein, R. Kupke, R. Vetter, F. Lenz, M. Kliem, C. Buelow, J. Goyvaerts, T. Mayer, and S. Petrenz, "Review on quality assurance along the CFRP value chain — Non-destructive testing of fabrics, preforms and CFRP by HF radio wave techniques," *Composites: Part B*, vol. 77, pp. 494–501, March 2015. [Online]. Available: https://doi.org/10.1016/j.compositesb.2015.03.022

[11] S. Laurenzi and M. Marchetti, "Advanced Composite Materials by Resin Transfer Molding for Aerospace Applications," *Composites and Their Properties*, pp. 197–226, 2012. [Online]. Available: https://doi.org/10.5772/48172

[12] Concordia Fibers, "Carbon Twisting of Woven 3D Preforms," 2015. [Online]. Available: https://www.concordiafibers.com/carbon-twisting.html

[13] AVK – Industrievereiniung Verstaerkte Kunststoffe, *Handbuch Faserverbundkunststoffe: Grundlagen,*

Verarbeitung, Anwendungen. Vieweg & Teubner, 2010.

[14] Center for Lightweight Production Technology (ZLP), "EVo - Fully automated resin transfer molding (RTM) process for high volume parts."

[15] H. Heuer, M. Schulze, and N. Meyendorf, "Non-destructive evaluation (NDE) of composites: eddy current techniques," *Non-destructive evaluation (NDE) of polymer matrix composites*, pp. 33–55, 2013. [Online]. Available: https://doi.org/10.1533/9780857093554.1.33

[16] M. H. Schulze, H. Heuer, and N. Meyendorf, "Textural analyses of carbon fiber materials by 2D-FFT of complex images obtained by high frequency eddy current imaging (HF-ECI)," 2012. [Online]. Available: http://publica.fraunhofer.de/documents/N-206512.html

[17] C. Buelow, "Sensorintegration in einen vollautomatisierten RTM-Prozess," Master's thesis, University of Rostock, 2012.

[18] SURAGUS, "Non-destructive carbon fiber testing," 2017. [Online]. Available: https://www.suragus.com/en/applications/carbon-fiber-testing/

[19] E. Wood, "Applying Fourier and associated transforms to pattern characterization in textiles," *Textile Research Journal*, vol. 60, pp. 212–220, 1990.

[20] I. Hessen, Private Communication, 2018.

[21] Hexagon Metrology, "Leica T-Scan 5: Product brochure," 2015.

[22] ——, "Leica Absolute Tracker AT960: Product brochure," 2015.

[23] P. Bourke, "Calculating the area and centroid of a polygon," 1988. [Online]. Available: https://www.seas.upenn.edu/~sys502/extra_materials/Polygon%20Area%20and%20Centroid.pdf

[24] MathWorks, "Fitting an orthogonal regression using principal components analysis," 2018. [Online]. Available: https://de.mathworks.com/help/stats/examples/fitting-an-orthogonal-regression-using-principal-components-analysis.html

[25] D. Eberly, "Least squares fitting of data," *The Pennsylvania State University*, 2017. [Online]. Available: http://www.sci.utah.edu/~balling/FEtools/doc_files/LeastSquaresFitting.pdf

[26] Joint Committee for Guides in Metrology, *Evaluation of measurement data — Guide to the expression of uncertainty in measurement*. JCGM, 2008.

[27] B. Hienz and C. Buelow, "Ermittlung der Messgenauigkeit und Erprobung von Wirbelstromsensorik zur Qualitaetssicherung von komplexen CFK-Preforms," Master's thesis, University of Stuttgart: Institute of Aircraft Design, 2017.

[28] EVo Team, "Laser-based uncertainty analysis of EVo ECT turntable (unpublished)," 2018.

[29] CMG Lee, "Comparison of 1D and 2D interpolation," 2016. [Online]. Available: https://commons.wikimedia.org/wiki/File:Comparison_of_1D_and_2D_interpolation.svg

[30] McMaster University, "Bicubic interpolation," 2014. [Online]. Available: http://www.ece.mcmaster.ca/~xwu/interp_1.pdf

[31] esri, "Difference between Nearest Neighbor, Bilinear Interpolation and Cubic Convolution," 2016. [Online]. Available: https://support.esri.com/en/technical-article/000005606

[32] National Instruments, "Understanding FFTs and Windowing," 2018. [Online]. Available: https://www.ni.com/instrument-fundamentals

[33] MathWorks, "Contrast adjustment," 2018. [Online]. Available: https://de.mathworks.com/help/images/contrast-adjustment.html

[34] NDT Education Resource Center, "Eddy Current Testing: Depth of Penetration and Current Density," *Iowa State University*, 2014. [Online]. Available: https://www.nde-ed.org/EducationResources/CommunityCollege/EddyCurrents/Physics/depthcurrentdensity.htm